Properties of the Molecular Gas in Low Metallicity Environments

Dissertation
zur
Erlangung des Doktorgrades (Dr. rer. nat.)
der
Mathematisch–Naturwissenschaftlichen Fakultät
der
Rheinischen Friedrich–Wilhelms–Universität
Bonn

vorgelegt von
Jorge Luis Pineda Gálvez
aus Santiago de Chile

Bonn, Juni 2007

Angefertigt mit Genehmigung
der Mathematisch–Naturwissenschaftlichen Fakultät
der Rheinischen Friedrich–Wilhelms–Universität Bonn

1. Referent: Prof. Dr. Ulrich Klein
2. Referent: Priv.-Doz. Dr. habil. Endrik Krügel

Tag der Promotion: 19 Juni 2007

Contents

1 Introduction

The study of the star formation processes and its relation with their environment is of essential importance in modern astrophysics. The formation of stars has a crucial impact in the way galaxies evolve and therefore its understanding give us important insights in the evolution and nature of our Universe. Star formation has been extensively studied in our Galaxy (e.g. Evans, 1999) and to some extent in nearby galaxies (e.g. Kennicutt, 1998).

Stars form in dense molecular gas. The physical and chemical conditions of this gas determines the time scale, efficiency and rate at which the process of star formation occurs. Determinant properties of the molecular gas are the abundance of heavy elements[1] (metallicity) and the relative amount of dust (dust-to-gas ratio). Both parameters have a crucial impact on the chemistry and thermal balance of the ISM and they seem to be correlated (e.g. Lisenfeld & Ferrara, 1998). The metallicity and dust-to-gas ratio have evolved during the lifetime of the universe. Heavy elements are mainly produced by massive stars ($M > 8$ $M_\odot$) via nucleosynthesis and are then released in supernova explosions and in stellar winds from evolved stars. Dust is also initially mainly formed in supernova explosions until intermediate mass stars (6−8 $M_\odot$) reach the asymptotic giant branch (AGB) becoming the dominant dust producers. The cyclic process of formation and destruction of massive stars enriches progressively the environment with metals and dust. This implies that in young galaxies the process of star formation develops in low-metallicity, low gas-to-dust ratio environments.

1.1 Photon-Dominated Regions

Star formation has an immediate impact on the molecular clouds where it occurs, in particular if the formed stars are massive. Stars interact with the molecular gas via stellar winds and its radiation. Stellar photons produce regions of hot ionized gas in the immediate vicinity of the stars. At larger distances from stars the ISM is cold, dense, and molecular. The interface between the hot ionized medium and the cold and dense molecular cloud is called a photon-dominated region (PDR; see Hollenbach & Tielens (1999) for a review).

Photon-dominated regions are parts of the interstellar medium where the structure, chemistry and thermal balance are dominated by the influence of stellar far-ultraviolet photons (6eV<hν<13.6 eV). This far-ultraviolet radiation is able to ionize, dissociate and heat the gas.

The structure of a PDR depends on how the far-ultraviolet radiation penetrates the molecular cloud. This is mainly determined by dust absorption, with some contribution of dust scattering and absorption by molecules. Figure 1.1 shows a schematic

[1] Elements heavier than Li

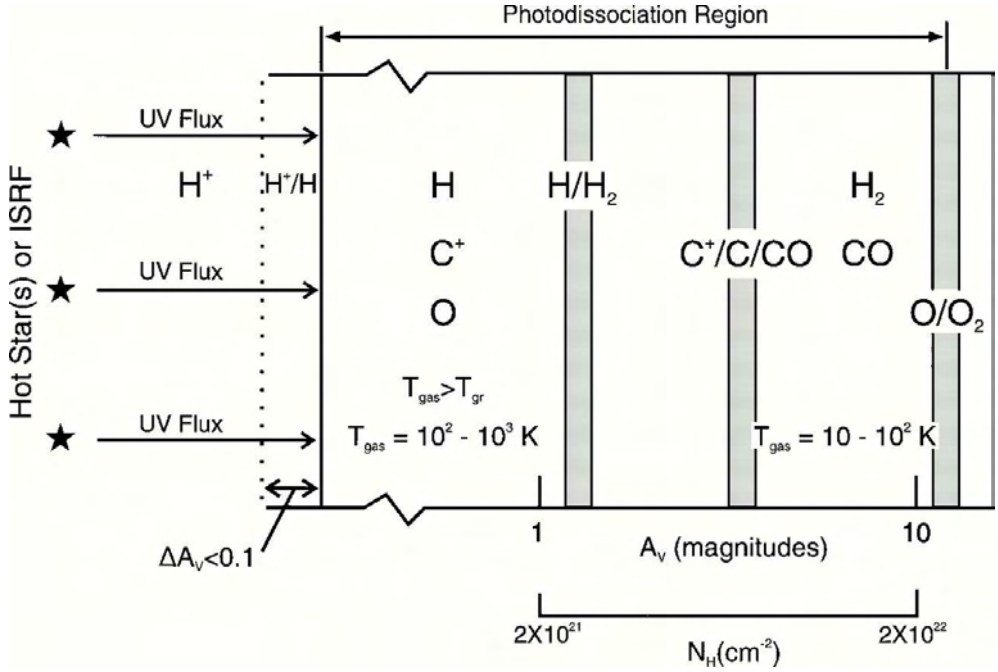

Fig. 1.1: *Structure of a Photon Dominated Region (PDR). Reproduced from Hollenbach & Tielens (1999).*

representation of a PDR as a function of cloud depth, quantified by the visual extinction A_V in units of magnitudes. The PDR is overlaid with a layer of ionized hydrogen until FUV photons, capable to ionize hydrogen ($h\nu$=13.6 eV), are absorbed in a thin ($N_H \sim 10^{19}cm^{-3}$, $\Delta A_v \simeq 10^{-2}$) H II/H I interface layer. Then, photons with energies between 11-13.6 eV dissociate H_2 and ionize carbon forming a H I/C II region. These photons are absorbed at about $A_v \sim 2$ mag, producing a H_2/C II region until photons that ionize carbon are absorbed at about $A_v \sim 4$ mag, then producing a C I/CO transition layer. Deeper into the cloud oxygen starts to be in molecular form.

The temperature in PDRs depends on the balance between heating and cooling processes. The energy input comes from the stellar far-ultraviolet radiation, mainly through the photoelectric effect on dust grains and from the excitation of H_2 by far-ultraviolet photons. Depending in the density and temperature of the region, this energy is then re-radiated, for example, via fine-structure transitions such as [C II] 158 μm, [O II] 63,146 μm, [C I] 609,370 μm and rotational transitions of CO and its isotopomers. All these transitions are in the infrared, millimetre and sub-millimetre domain.

Since the far-ultraviolet radiation dominates the chemistry in PDRs photo-reactions are very important. The temperatures in PDRs allow many endothermal reactions, reactions with activation barriers and reactions with excited H_2 (H_2^*). Figure 1.2 shows the most important reactions of the carbon and oxygen chemistries. In the case of high densities and temperatures, reactions with excited molecular hydrogen H_2^* enhance, for example, the abundance of OH and CH^+. These molecules react with C^+ and

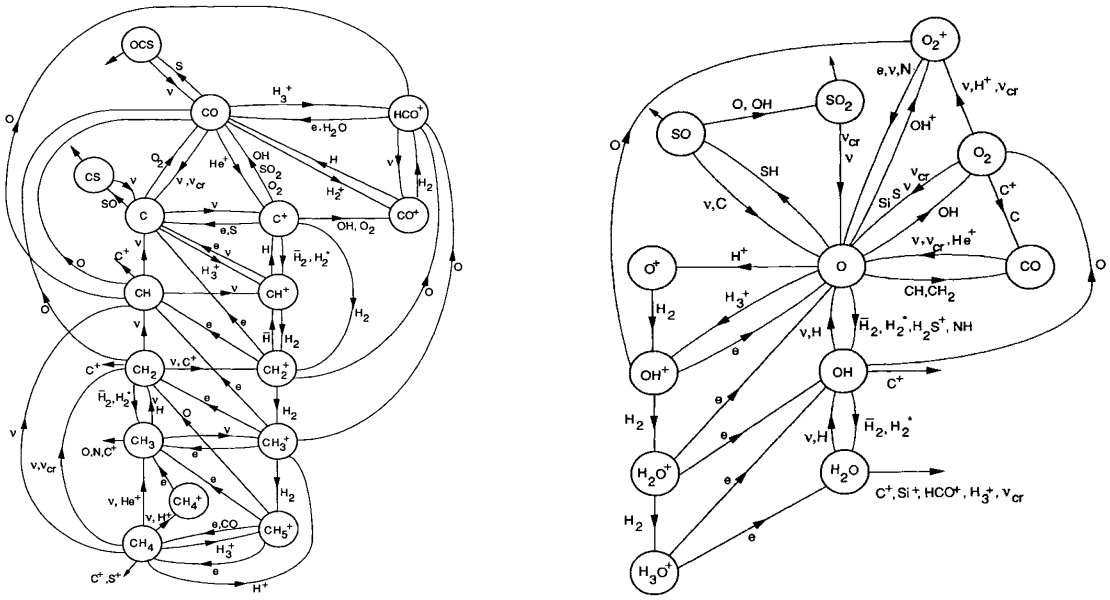

Fig. 1.2: *Chemical networks for carbon and oxygen chemistries. Taken from Sternberg & Dalgarno (1995).*

O, respectively to form CO^+ which later exchanges charge with H to form CO. The presence of polycyclic aromatic hydrocarbons (PAHs) is also important for the carbon chemistry, enhancing the abundance of neutral atoms like C or S due to neutralizations between the corresponding ions on PAH^-s (Lepp & Dalgarno, 1988; Bakes & Tielens, 1998).

In low-metalicity environments the gas-to-dust ratio is reduced. This allows the far-ultraviolet radiation field to penetrate more deeply into the molecular gas and to modify the structure of PDRs. This effect is important for the chemistry of carbon: The CO molecules are less efficiently self-shielded compared to the strongly self-shielded H_2 (van Dishoeck & Black, 1988). This produces significant changes in the relative amounts of H_2 and CO in molecular clouds. The enhanced photo-dissociation of CO increases the size of the C II/C I/CO transition layer in PDRs (see Fig. 1.1) and therefore increases the abundance of C II and C I relative to the CO abundance. Under these conditions, the sites of large-scale star formation must hence be regarded as giant PDRs, where the molecular content is also (indirectly) traced via the atomic carbon in its neutral [C I] and ionized [C II] form.

PDRs can be found in many different environments in the Universe. Examples are the centers of galaxies, protostellar disks, hot cores, galaxies, etc (Figure 1.3).

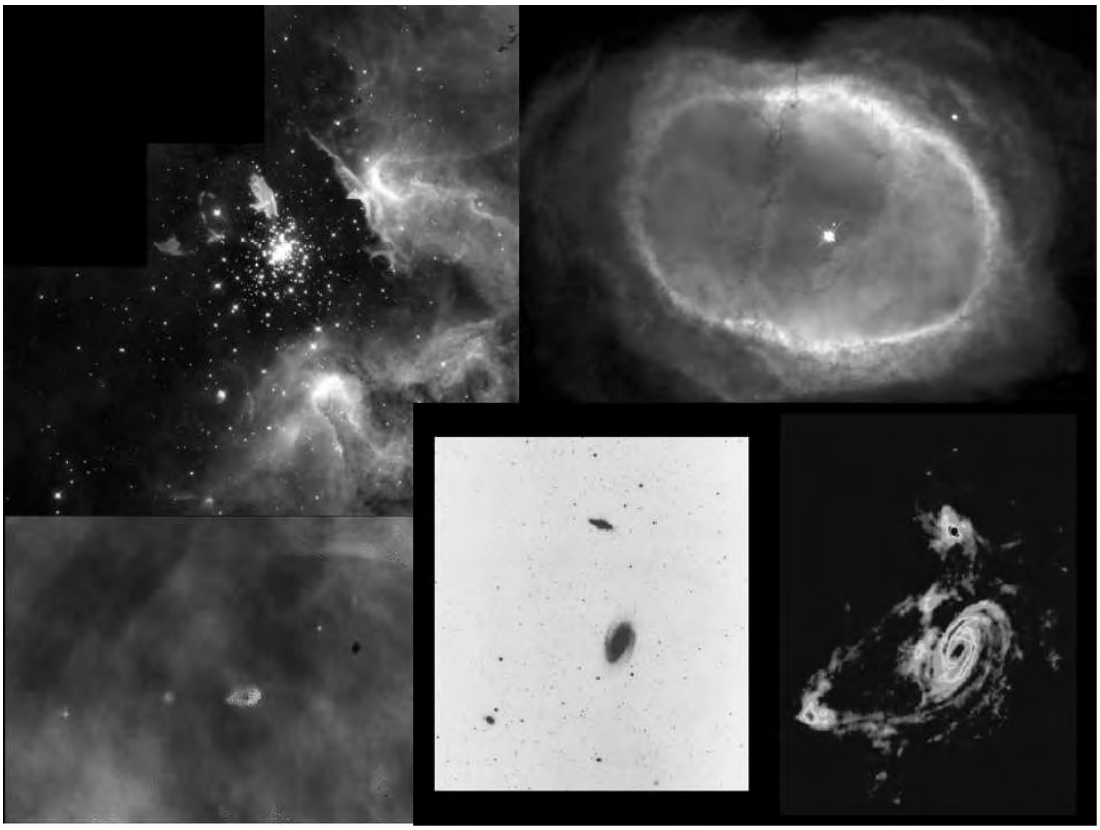

Fig. 1.3: *Photon-dominated regions are present in many different environments in our Universe. Examples are star-forming regions (upper left), planetary nebulae (upper right), protoplanetary disks (lower left), and in galaxies (lower right).*

1.2 The Clumpy Structure of Molecular Clouds

Molecular clouds show a clumpy structure where the stellar far-ultraviolet radiation field can penetrate deeper (Figure 1.4). In this context, the molecular cloud is composed of many discrete high-density clumps embedded in a low-density inter-clump medium, which spreads the far-ultraviolet photons via scattering (Boisse, 1990; Meixner & Tielens, 1993).

In models which represent the PDR as plane-parallel (e.g. Black & van Dishoeck, 1987; Le Bourlot et al., 1993; Tielens & Hollenbach, 1985; Sternberg & Dalgarno, 1989), the emission from the principal cooling lines in PDRs emerges from spatially separated regions. However, observations of the [C II] line emission have shown that they are spatially coexistent (e.g. Stutzki et al., 1988; Howe et al., 1991; Stacey et al., 1993; van der Werf et al., 1996). This suggests that the observed line emission is the integrated light from many individual PDRs on the surface of irradiated clumps, which are much smaller than the beam of the observations.

Further evidence for the existence of a clumpy medium arises from direct observations

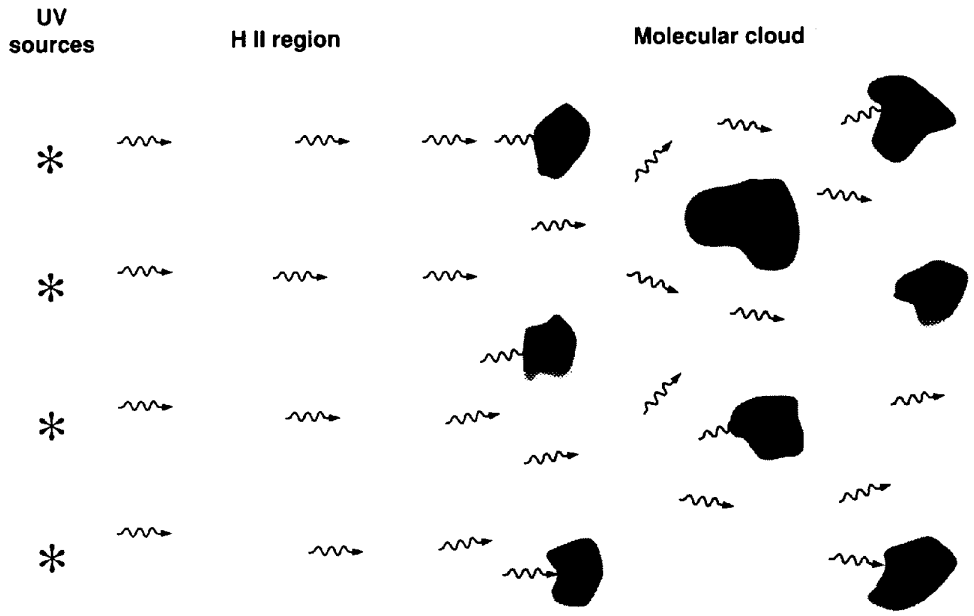

Fig. 1.4: *Illustration of a clumpy medium exposed to a far-ultraviolet radiation field. Taken from Meixner & Tielens (1993)*

of hierarchical, clumpy structures in molecular clouds (e.g. Kramer et al., 1998; Heithausen et al., 1998) and from the low volume filling factors estimated toward warm and dense cores (e.g. Ho & Townes, 1983; Snell et al., 1984; Evans et al., 1987).

1.3 PDR Models

In order to provide a self-consistent solution to the chemical structure and temperature of photon-dominated regions, we utilize a the spherically symmetric PDR model developed by (Störzer et al., 1996) (KOSMA$-\tau$) in the present thesis. The model assumes a spherical clump isotropically illuminated by an external far-ultraviolet radiation field. The density structure of the clump is given by a truncated power-law density profile of the form

$$n(r) = n_{\rm s}(r/r_{\rm c})^{-\alpha}, \tag{1.1}$$

for $r' \leq r \leq r_{\rm c}$, and

$$n(r) = n_{\rm s}(r'/r_{\rm c})^{-\alpha}, \tag{1.2}$$

for $r \leq r'$. Here n_s and r_c are the surface density and clump radius respectively. The PDR model solves the chemical network (abundance of species) and the thermal balance (heating & cooling) in an iterative process. This results in abundances of species as a function of cloud depth. The ONION radiative transfer code (Gierens et al., 1992) is then used to compute the emerging line intensity of the [C II] and [C I] fine structure transitions and the ^{12}CO and ^{13}CO rotational transitions.

Spherical symmetry is considered because it accounts for the fact that molecular clouds have small-scale substructure, which can have an important impact on the observed line emission. In the PDR modelling, we assume that the medium can be represented by an ensemble of clumps with uniform mass and density. These are the clumps that dominate the observed line ratios. Thus, we can study the medium by modelling one single clump. Clumps with different sizes or densities are not excluded but we assume that they do not dominate the observed line ratios.

The assumption of an isotropic far-ultraviolet radiation field is supported by the fact that in a clumpy medium the far-ultraviolet field penetrates deeper into the molecular material compared with a homogenous medium. Then, multiple scattering of photons is efficient in maintaining the isotropic far-ultraviolet radiation field (Boisse, 1990; Meixner & Tielens, 1993).

1.4 Aims and Outline

The aim of this thesis is to study the properties of photon-dominated regions under different physical conditions. Specifically, we are interested in the impact of the metallicity and strength of the FUV radiation field in the molecular gas traced by PDRs. Our approach is to study both parameters separately. As we can see in Figure 1.5, we can distinguish different PDRs, depending on the strength is the FUV radiation field to which it is exposed or how different the metallicity of the gas is compared to the solar vicinity.

We first study PDRs exposed to weak far-ultraviolet radiation fields because they allow us to minimize the effects of the UV radiation field in the molecular gas so that the impact of other parameters, such as the metallicity, can be studied. Note that most of the molecular in the Galaxy is exposed to low-FUV radiation fields.

In Chapter 2, we first study a solar-metallicity cloud exposed to a radiation field of the order of the mean interstellar radiation field: Barnard 68. Its roughly spherical morphology and accurately determined density profile (Alves et al., 2001) makes Barnard 68 an ideal "calibrator" for spherical PDR models. This allows us to study the impact of the chemistry in the model line emission in detail.

With a better understanding of a PDR exposed to weak far-ultraviolet radiation fields we study the impact of the metallicity on the properties of the molecular gas in the

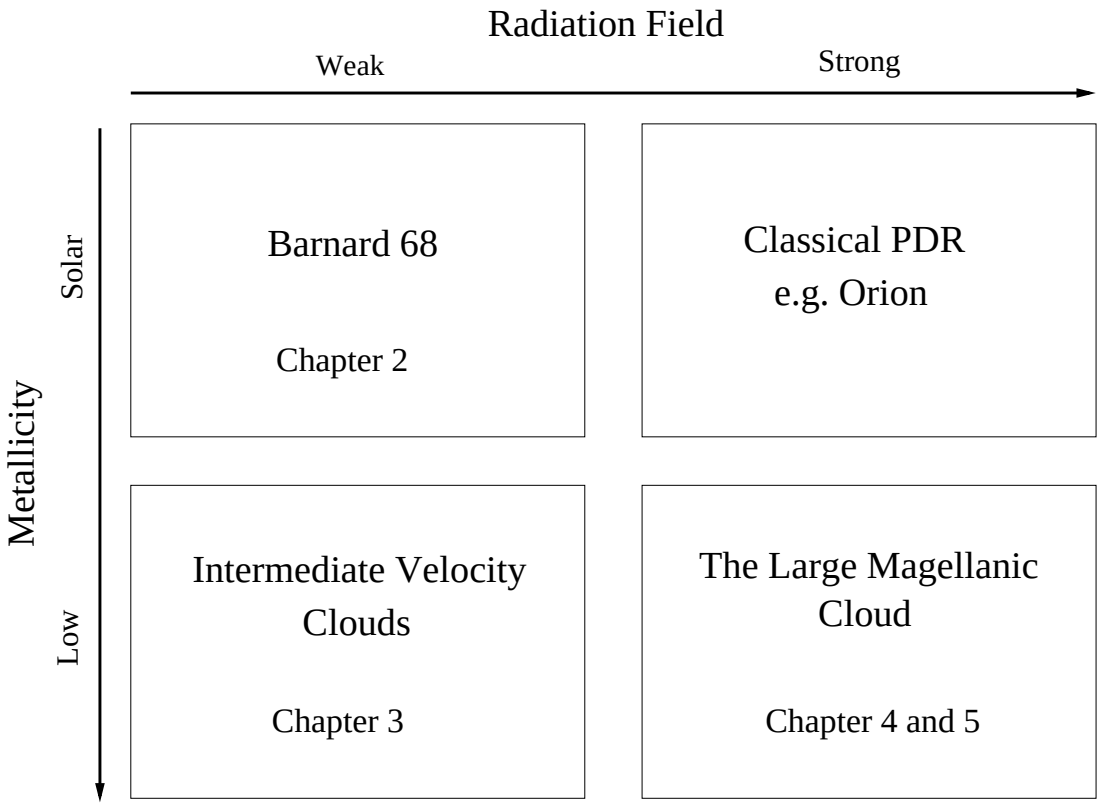

Fig. 1.5: *Different PDRs can be distinguished depending on the strength of the FUV radiation field and on the metallicity of the gas. The regime of weak FUV radiation fields and Solar metallicity is studied in Chapter 2. In Chapter 3 we study the impact of low metallicity in PDRs exposed to weak FUV radiation fields. Finally, low-metallicity environments exposed to strong FUV radiation fields are studied in Chapter 4 and 5. The solar-metallicity PDR exposed to a strong FUV radiation field has been extensively studied (For the case of Orion, see Tielens & Hollenbach 1985).*

regime of weak far-ultraviolet radiation fields in Chapter 3. These conditions can be observed in intermediate-velocity clouds (IVCs). IVCs are high-latitude translucent clouds with radial velocities in excess compared to those expected for galactic rotation. Ultraviolet absorption studies have revealed metallicities between 50-100% solar in IVCs (Wakker, 2001), and PDR models suggest that they are composed of young molecular material (Heithausen et al., 2001).

Having studied the properties of low-metallicity molecular gas exposed to weak FUV radiation fields, we study the effects of the strong FUV radiation fields in low-metallicity gas in Chapter 4. For that we focus in the most nearby example, the Large Magellanic Cloud (LMC). Its short distance (50 kpc; Feast, 1999) and nearly face-on orientation allow us to study it in great detail. The most prominent feature in the LMC is the 30 Doradus H II complex. Observations of the molecular gas in this region (Cohen et al., 1988; Fukui et al., 1999) have revealed a huge chain of molecular clouds, stretch-

ing south of 30 Doradus for nearly 2 kpc. This unique region represents clouds exposed to extreme FUV radiation fields and also regions exposed to weaker radiation fields. Therefore, it serves as a laboratory to study the properties of the low-metallicity molecular gas as a function of the far-ultraviolet radiation field. In Chapter 5 sub-millimeter observations of the N159W region in the LMC are analyzed with a PDR model. In Chapter 6 we investigate the effect of the FUV radiation field in the line ratios of PDR models with low-metallicity. A summary and future prospects are presented in Chapter 6.

2 Photon Dominated Region Modelling of Barnard 68

Parts of this chapter have been submitted for publication in Astronomy and Astrophysics (Pineda, J.L & Bensch, F., 2007).

2.1 Introduction

The understanding of Photon Dominated Regions (PDRs) is of great interest as they account for much of the millimitre, sub-millimitre and far-infrared line and continuum radiation, from the molecular interstellar medium (ISM) of nearby star-forming regions to clouds in the diffuse Galactic radiation field. Many numerical codes have been developed in order to model their emission and to understand the physical and chemical processes governing them (Hollenbach & Tielens, 1999). Typically, PDR models use a physical structure (morphology, density profile) to calculate a self-consistent solution for the chemistry (abundance of species) and the energy balance (heating and cooling). Practically, the numerical codes differ by the scope of the chemical networks and their reaction rates as well as by the degree of sophistication with which the heating, cooling and radiative transfer are calculated. In many cases the goal of the PDR modelling is to constrain the physical properties of the line-emitting region (for example, its density and column density) and the strength of the external far-ultraviolet (FUV) field. The coupling of the energy balance (heating & cooling) and the chemistry makes PDR modelling not a straightforward task. In particular, a large set of non-linear equations needs to be solved in order to obtain abundance profiles of species. Small changes in the initial elemental abundances or the reaction rates of individual reactions within their sometimes large error margins can result in large variations of the abundance profiles of individual species (Röllig et al., 2007). In some regions of the parameter space, more than one steady-state solution to the chemical network may exist (bistability, e.g. Le Bourlot et al., 1993). Additional complications arise from intrinsic variations of published PDR models which are noted even when identical source parameters and chemical reaction rates are used. The benchmarking study (Röllig et al., 2007) has shown that even for constant-density, plane-parallel models the emerging line intensity of different numerical codes vary by up to an order of magnitude for some of the fine structure transitions. These discrepancies likely reflect the different numerical methods which are used to solve the chemical structure as well as the numerical implementation of physical processes. Since the benchmarking models assume a plane-parallel geometry, they cannot be easily calibrated with observed clouds, which generally have more complex morphologies. It is therefore desirable to study clouds with a well-known geometry (density profile), which can be used to calibrate PDR models.

Barnard 68 is an example where the density profile is constrained to a very high precision (Alves et al., 2001), and its geometry is well matched by a spherically-symmetric

Tab. 2.1: *Spectral Line Observations Toward Barnard 68*

Telescope	Transition	# of Positions	Sampling [arcsec]	$\theta_{\rm mb}$ [arcsec]	$\eta_{\rm mb}$	Δv [km s^{-1}]
SWAS	[C I] $^3P_1 \rightarrow ^3P_0$	1	–	258	0.9	0.623
Mopra	^{12}CO $J = 1 \rightarrow 0$	144	15	33	0.42	0.08
KOSMA	^{12}CO $J = 2 \rightarrow 1$	49	60	130	0.76	0.1
KOSMA	^{12}CO $J = 3 \rightarrow 2$	49	60	80	0.78	0.294
KOSMA	^{12}CO $J = 3 \rightarrow 2$	1	–	80	0.78	0.024
CSO[1]	^{13}CO $J = 2 \rightarrow 1$	65	24	33	0.70	0.06
CSO[1]	^{13}CO $J = 3 \rightarrow 2$	144	24	22	0.75	0.04

[1] Published by Bergin et al. (2006).

PDR model. With no young stars nearby, the external FUV field is low, of the order of the diffuse Galactic radiation field. Because of its proximity to the Ophiuchus complex, we adopt a distance to the cloud of 125 pc (de Geus et al., 1989). Using near-infrared extinction techniques, Alves et al. (2001) derived an extinction map that was used to constrain the radial density profile of the cloud, suggesting that Barnard 68 is consistent with a pressure-confined self-gravitating cloud near equilibrium, a so-called Bonnor-Ebert sphere. Avoiding the uncertainly concerning the geometry and density structure we are able to study in detail the impact of the chemistry in the predicted line emission of the model.

Here, we present observations of the three lowest rotational transitions of ^{12}CO, the [C I] $^3P_1 \rightarrow ^3P_0$ fine structure transition of neutral carbon, ^{13}CO $J = 2 \rightarrow 1$, and ^{13}CO $J = 3 \rightarrow 2$ and compare them to the KOSMA-τ spherical PDR model originally published by Störzer et al. (1996). The observations are summarized in Section 4.3. Section 2.3 describes the employed model, and the results are discussed in Section 4.4. In Section 2.5 the gas heating and cooling is studied and predictions of the intensity for other important cooling lines are made. A summary is given in Section 4.6.

2.2 Observations

Observations were made of the three lowest rotational transitions of CO and the [C I] $^3P_1 \rightarrow ^3P_0$ fine structure transition of neutral carbon in Barnard 68. Additionally, we use the ^{13}CO $J = 3 \rightarrow 2$ and $J = 2 \rightarrow 1$ rotational transitions observed with the CSO telescope and published by Bergin et al. (2006). Using these transitions we deliberately limit ourselves to surface tracers, since the goal is to model of the PDR emission of a cloud in the diffuse Galactic radiation field.

The high signal-to-noise [C I] $^3P_1 \rightarrow ^3P_0$ observation was made in 2001 with the Sub-

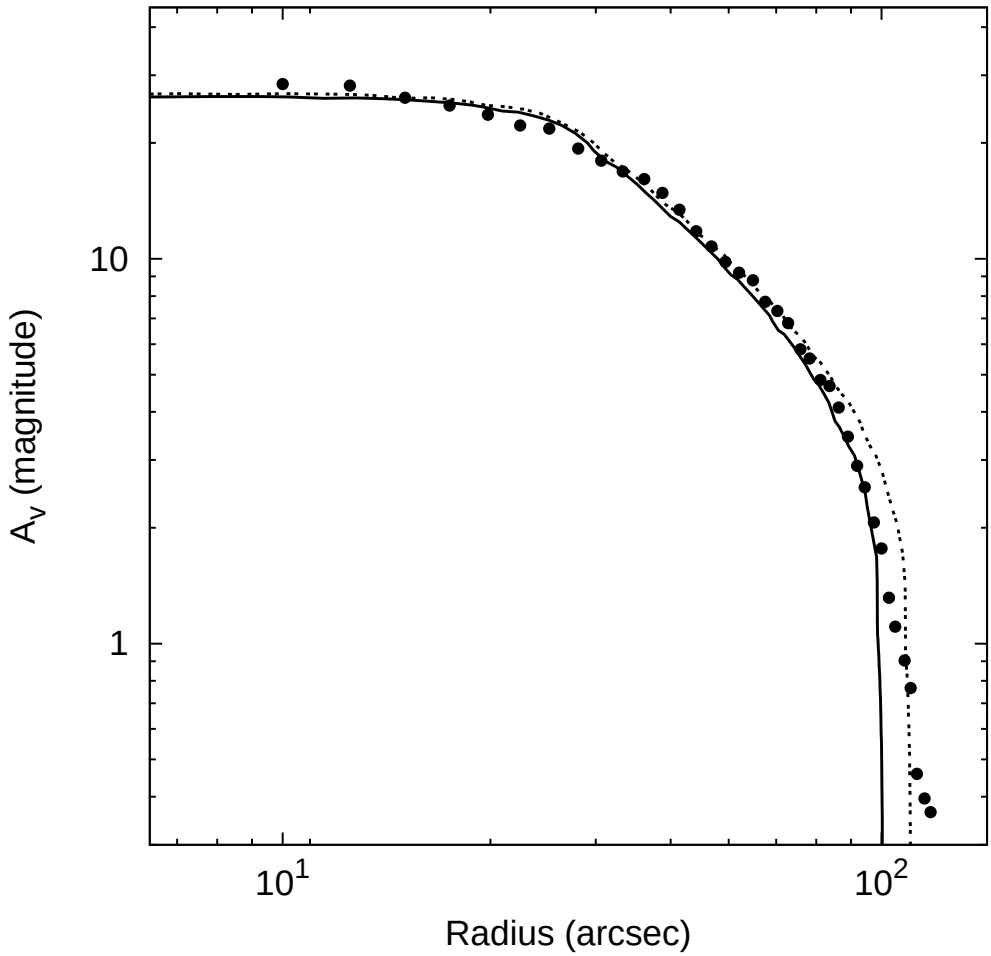

Fig. 2.6: *The solid line is the power-law density profile of the PDR model (Section 2.4.1). The dashed line is the same column density profile for a model with the same density power-law index but a 10% larger radius. Filled dots represent the measured A_v calculated by Alves et al. (2001), excluding the south-east prominence seen in the visual extinction map.*

millimiter Wave Astronomy Satellite (SWAS[2]) and has an angular resolution of 4′.3. It is pointed at a position offset by $\Delta\alpha = -0'.094$, $\Delta\delta = +0'.2$ from the column density peak of Barnard 68 at $\alpha = 17^h22^m38''.6$ and $\delta = -23°49'46''.0$ (J2000) (Di Francesco et al., 2002) and covers essentially the whole cloud. The r.m.s noise ΔT_{mb} is 23 mK per velocity channel (Δv= 0.623 km s^{-1}). A 3rd-order polynomial was fitted and subtracted from the spectra. SWAS simultaneously observes the transitions of four species, [C I] $^3P_1 \rightarrow {}^3P_0$ at 492 GHz, ^{13}CO $J = 5 \rightarrow 4$ at 550.9 GHz, H_2O at 556.0 GHz, and O_2 at 487.2 GHz. No emission is detected for the latter three species, however, and Bergin & Snell (2002) gave the resulting upper limits on the H_2O and O_2 column densities. The r.m.s noise of the ^{13}CO $J = 5 \rightarrow 4$ spectrum is 13 mK per velocity channel.

[2]See Melnick et al. (2000) for additional details about SWAS.

Tab. 2.2: *Fractional Abundances*[a]

He	0.1
C	1.32×10^{-4}
O	2.91×10^{-4}
N	8.5×10^{-5}
^{13}C	2.08×10^{-6}
S	1.87×10^{-6}
Mg	5.12×10^{-6}
Fe	6.19×10^{-6}
Si	8.21×10^{-7}
PAH[b]	1×10^{-7}

[a] Abundance relative to H nuclei.
[b] Not included in the reference model.

The ^{12}CO $J = 1 \rightarrow 0$ (115 GHz) rotational transition was observed in June 2005 with the Mopra 22-m telescope located in Australia. A $6' \times 6'$ area was mapped using the on-the-fly mapping mode. The data were smoothed to an angular resolution of $1'$ on a grid with a $30''$ spacing. The resulting spectra typically have a r.m.s noise $\Delta T_{\rm mb}$ better than 0.5 K per velocity channel (Δv= 0.08 km s^{-1}). A straight line was fitted and subtracted from each spectrum.

The ^{12}CO $J = 2 \rightarrow 1$ (230 GHz) and ^{12}CO $J = 3 \rightarrow 2$ (345 GHz) transitions were mapped simultaneously with the 230/345 GHz dual-channel receiver at the KOSMA 3-m telescope toward 49 positions, spaced by $1'$. For the ^{12}CO J = 2$\rightarrow$1 transition 90% of the spectra have a r.m.s noise $\Delta T_{\rm mb}$ smaller than 0.3 K per velocity channel (Δv= 0.1 km s^{-1}). The ^{12}CO $J = 3 \rightarrow 2$ spectra are smoothed to the $130''$ angular resolution of the 230 GHz beam, and 90% of the spectra have a r.m.s noise $\Delta T_{\rm mb}$ smaller than 0.5 K per velocity channel (Δv= 0.294 km s^{-1}). Typically, a sinusoidal or 3rd-order polynomial was fitted to and subtracted from each spectrum. The offsets are given relative to the position of the column density peak. Because of a small misalignment of both receiver channels the pointing of the 345 GHz beam is offset by ΔAZ=$-7''$ and ΔEL=$+28''$ in horizontal coordinates relative to the lower-frequency beam. The observations were completed within a relatively short period of time during the transit of the source. Thus, the offset in the horizontal system translates into an offset of approximately $\Delta\alpha = -7''$ and $\Delta\delta$=$-28''$ in equatorial coordinates, which was corrected for in the final map. We estimate the accuracy of this correction to be within $\sim 15''$.

The observed spectra are shown in Figure 2.7 and a summary of the observations is given in Table 2.1.

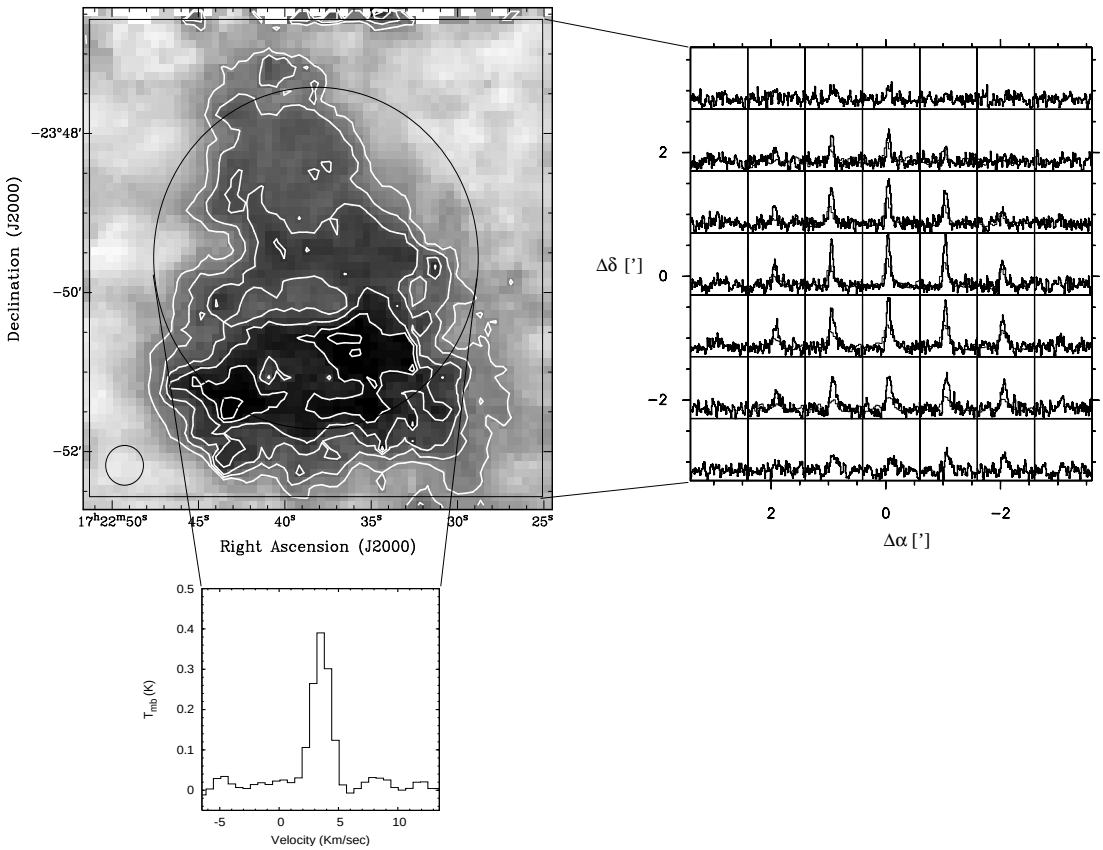

Fig. 2.7: *Upper left: Map of the* ^{12}CO $J = 1 \rightarrow 0$ *emission of Barnard 68, shown with its original resolution of 33″. The contours run from 40% to 90% of the peak intensity (72.6 K km s*$^{-1}$*) in steps of 10%. Upper right: Spectra of the* ^{12}CO $J = 2 \rightarrow 1$ *(thick lines) and* $J = 3 \rightarrow 2$ *(thin lines) transitions with a resolution of 130″. The velocity range is* $v = 0 \ldots 8$ *km s*$^{-1}$*, and the main-beam temperature shown is* $T_{\rm mb} = -1 \ldots 5$ *K . The offset is given in arcminutes. Lower left: [C I]* $^3P_1 \rightarrow {}^3P_0$ *emission toward the central position of Barnard 68. The 4′.3 beam size of SWAS covers a large fraction of the cloud.*

2.3 PDR Model

We employ the spherically symmetric PDR model originally developed by Störzer et al. (1996) (KOSMA-τ model). This model uses a spherical cloud with a truncated power-law density profile and an isotropic FUV radiation field. We adopt a density profile of, $n(r)$=$n_{\rm s}(r/r_{\rm c})^{-\alpha}$ for $0.3r_{\rm c} \leq r \leq r_{\rm c}$, and constant density, $n(r) = n_s(0.3)^{-\alpha}$ in the cloud center ($r < 0.3r_{\rm c}$). Here, $r_{\rm c}$ is the cloud radius and $n_{\rm s}$ is the density at the cloud surface. The chemical network of the model includes H, He, C, O, N, plus a number of heavier elements, such as S, Si, Fe, and Mg. ^{13}C is considered in the chemical network, including the isotope-selective reactions of ^{13}CO. Initial fractional abundances are listed in Table 2.2. Line intensities and line profiles are determined for the [C II] and the [C I] fine structure transitions and the ^{12}CO and ^{13}CO rotational

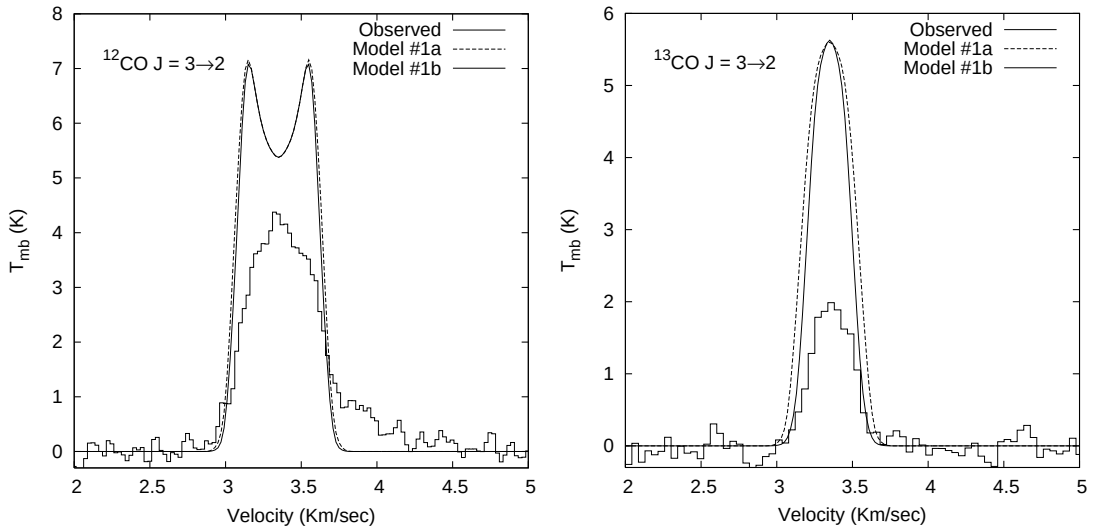

Fig. 2.8: *Observed ^{12}CO and ^{13}CO $J = 3 \rightarrow 2$ line profiles. The reference model (Model #1a) and a model which considers the effects of depletion (Model #1b) are also shown.*

transitions using the radiative transfer code by Gierens et al. (1992). For a comparison to the observed data we smoothed the model intensity distribution and line profiles to the angular and velocity resolution of our observations.

2.4 Results

2.4.1 Reference Model

In the following, we define a reference model (Model #1a) in which we adopt a power-law exponent of $\alpha = 1.96$ for the density profile, a cloud surface density $n_s = 2.01 \times 10^4$ cm^{-3}, and a cloud radius $r_c = 1.875 \times 10^{17}$ cm. This gives a reasonable fit to the measured column density profile for $r \lesssim 100''$, but does not account for the low-column density gas close to the surface at $100'' \lesssim r \lesssim 120''$ (Figure 2.6). We tested the response of the emerging CO emission to small variations of the model cloud size. An extreme case is shown in Figure 2.6 by the dotted line ($r_c = 2.09 \times 10^{17}$ cm), which matches the observed A_v at $100'' \lesssim r \lesssim 120''$, but overestimates the column density for $70'' \lesssim r \lesssim 100''$. The latter model produces CO emission that is typically larger by only a few percent, however.

The Doppler line-width in the model is $b = 0.11$ km s^{-1}, derived from the observed ^{13}CO $J = 2 \rightarrow 1$ line profile. This is slightly larger than the pure thermal line width of $\sim$0.1 km s^{-1} for CO in a 16 K gas (this gas temperature was measured for Barnard 68 by Bourke et al. 1995). The strength of the external FUV field in the reference model is $\chi = 1.0\,\chi_0$, where χ_0 is the intensity of the mean interstellar radiation field (Draine 1978).

Our modelling goal is to match the observed line-integrated intensity and line profiles towards the cloud center as well as the intensity distribution of the cloud. Table 2.3 shows the [C I], ^{12}CO, and ^{13}CO integrated intensity towards the cloud center (observations and the corresponding model simulation). Considering that the data were observed at different angular resolutions, we convolve the model results to any required resolution, in order to compare with the observations.

Model #1a reproduces the line-integrated intensity toward the cloud center for the [C I] $^3P_1 \rightarrow ^3P_0$, ^{12}CO $J = 1 \rightarrow 0$, and $J = 2 \rightarrow 1$ transition within 20%. However, the model ^{12}CO $J = 2 \rightarrow 1$ and $J = 3 \rightarrow 2$ line profiles show self-absorption, which is not observed (Figure 2.8). Moreover, the ^{12}CO $J = 3 \rightarrow 2$, and the ^{13}CO emission are significantly larger than observed. The largest discrepancy is noted for the ^{13}CO transitions, with line-integrated intensities in the model being larger by 1.9 and 3.2 for the $J = 2 \rightarrow 1$ and $J = 3 \rightarrow 2$ transitions, respectively.

We note that the ^{12}CO $J = 3 \rightarrow 2$ mapping observations for $r < 100''$ (Figure 2.11) have a larger line intensity than the observation in Figure 2.8 made toward the center position. The ^{12}CO observations made with a high velocity resolution of ~ 0.1 km s^{-1} show a red line wing, with emission at velocities between 3.7 and 4.3 km s^{-1} (e.g. left panel of Figure 2.8). This component cannot be modeled in the framework of a single, spherical clump; for a comparison to the PDR model simulations we calculated the observed line-integrated intensity excluding this red line wing. This was not possible for the ^{12}CO $J = 3 \rightarrow 2$ mapping data because of the insufficient velocity resolution, and we expect that the line-integrated intensity of ^{12}CO $J = 3 \rightarrow 2$ in Figure 2.11 is systematically overestimated. We estimate the magnitude of this effect to be of the order of 20%, based on our velocity-resolved ^{12}CO observations.

Since the density profile of Barnard 68 is well constrained, the discrepancies with the observations must have their origin in the chemical network or the strength of the FUV radiation field.

2.4.2 Depletion

The observed line emission is significantly overestimated by the model for those transitions that probe somewhat deeper layers into the cloud surface, most notably the ^{13}CO transitions. Observations of C^{18}O and C^{17}O in Barnard 68 reveal that CO, among other molecules, is depleted from the gas phase at $A_v \gtrsim 5$ due to freezing on dust grains (Hotzel et al., 2002; Di Francesco et al., 2002; Bergin et al., 2006). In the present model, we study the impact of the CO depletion on the line emission by truncating the ^{12}CO and ^{13}CO abundance profiles at $A_v = 5$ (setting the CO abundance to zero for $A_v \geq 5$; Model #1b). This is only a rough approximation, however, it allows us to assess the impact of depletion on the line emission. Figure 2.8 shows the ^{12}CO and ^{13}CO $J = 3 \rightarrow 2$ line profiles for Model #1a and Model #1b; the resulting line-integrated intensities for the observed transitions are summarized in Table 2.3. The line-integrated

intensities are smaller by 10−20% in the model with depletion, mainly because the line profiles are narrower. We confirm that depletion plays a negligible role for low−J ^{12}CO emission, but note a larger impact on both ^{13}CO transitions (20%) and the ^{12}CO $J = 3 \rightarrow 2$ transition (5%). However, the effect of depletion is much smaller than the factor of 2 to 3 discrepancy noted between the observations and the model line intensities. Thus, depletion of CO cannot solely account for the low integrated intensity observed for the latter transitions. In the following models (Model #2b, #3a, and #3b) we account for depletion in the same way as done in Model #1b.

2.4.3 Polycyclic Aromatic Hydrocarbons

Polycyclic Aromatic Hydrocarbons (PAHs) are known to play an important role in the carbon chemistry, increasing the C column density and decreasing the CO abundance in the cloud surface (Lepp & Dalgarno, 1988; Bakes & Tielens, 1998). Following Kaufman et al. (1999) we included PAHs with an initial abundance of 1×10^{-7} relative to H nuclei and assuming a MRN (Mathis et al., 1977) size distribution for PAHs containing between 30 and 1500 carbon atoms. We consider neutral PAHs in our chemical network, their singly charged variants (PAH^+, PAH^-), as well as PAHs with carbon and hydrogen ions adsorbed on their surface ($PAHC^+$, $PAHH^+$). We use a list of reactions provided by M. Kaufman (private communication) and calculate the reaction rates from the work of Draine & Sutin (1987) and Bakes & Tielens (1994). A comparison of the C^+, C^0, and CO abundance profiles and the gas temperature in the model with and without PAHs is shown in Figure 2.9. We note that the results are relatively insensitive to the initial PAH abundance as long as PAHs are included. Models with a factor of 4 larger PAH abundance give similar line-integrated intensities (to within 10 %).

One of the main impacts of PAHs is that the C^+ layer at the cloud surface becomes thinner, increasing the total atomic carbon column density. Close to the surface of the cloud PAH^- neutralizes with C^+, while CO is formed somewhat deeper into the cloud ($A_V > 0.4$). The larger neutral carbon column density and the higher gas temperature in the region with $A_V < 0.5$ (Figure 2.9) gives a stronger [C I] emission compared with the model without PAHs. The CO line intensity is reduced in Model #2b because the emission traces a slightly colder region somewhat deeper into the cloud. The lower CO abundance at $A_V < 0.4$ in Model #2b also removes the self-absorption in the ^{12}CO $J = 2 \rightarrow 1$ line toward the cloud center and reduces it for the ^{12}CO $J = 3 \rightarrow 2$ line.

Tab. 2.3: *Line-integrated intensity toward Barnard 68 center*

			Intensity (10^{-7} erg s^{-1} cm^{-2} sr^{-1})					
Species Transition	Telescope	Resolution ($''$)	Observed	Model #1a	Model #1b	Model #2b	Model #3a	Model #3b
[C I] $^3P_1 \rightarrow ^3P_0$	SWAS	258	0.928±0.05	0.902	0.913	1.443	1.290	0.388
^{12}CO $J = 1 \rightarrow 0$	Mopra	60	0.108±0.01	0.117	0.107	0.094	0.089	0.056
^{12}CO $J = 2 \rightarrow 1$	KOSMA	130	0.474±0.01	0.588	0.564	0.525	0.475	0.260
^{12}CO $J = 3 \rightarrow 2$	KOSMA	80	0.632±0.04	1.626	1.544	1.460	1.127	0.490
^{13}CO $J = 2 \rightarrow 1$	CSO	33	0.192±0.01	0.370	0.301	0.266	0.251	0.181
^{13}CO $J = 3 \rightarrow 2$	CSO	22	0.245±0.02	0.783	0.632	0.523	0.478	0.312

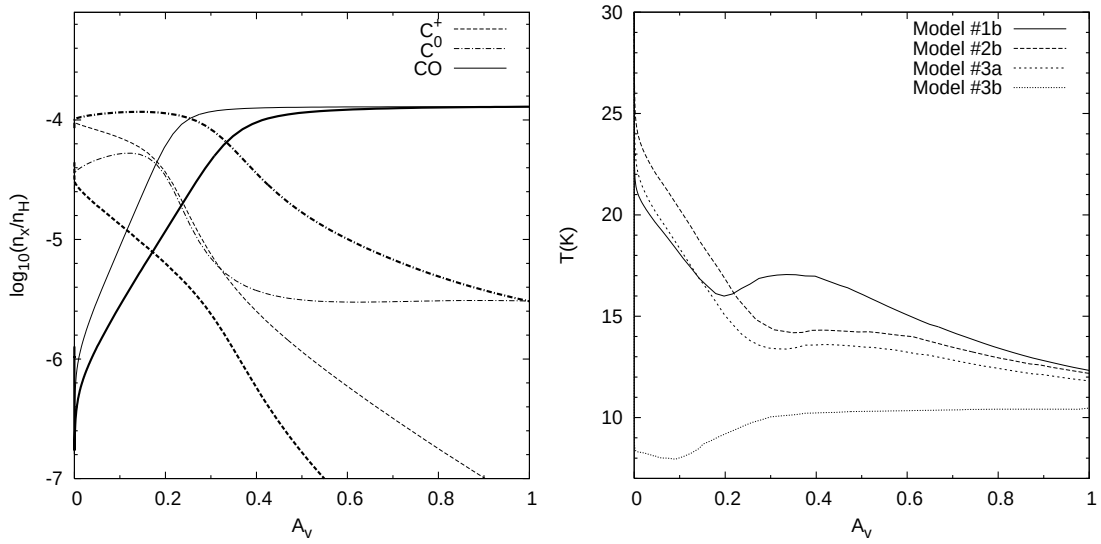

Fig. 2.9: *Left panel: The abundance profile of C^+, C^0, and CO for Model #1b (thin lines) and Model #2b (thick lines) are compared. Right panel: Gas temperature at the cloud surface as a function of A_V for models #1b, #2b,#3a, and #3b.*

While Model #2b gives [C I]/CO line ratios consistent with the observations and removes the ^{12}CO $J = 2 \rightarrow 1$ self-absorption noted in Model #1b, the line intensities of the [C I] and ^{13}CO transitions are still significantly larger than observed toward Barnard 68.

2.4.4 Variations of the Radiation Field

Generally, the line emission in the PDR model is reduced if a weaker external FUV radiation field is assumed. We explore the impact of lower external radiation field intensity as a next step. According to Bergin et al. (2006), the low ^{13}CO line intensities suggest that Barnard 68 is exposed to a FUV radiation field of rather low intensity, corresponding to $\chi = 0.12\,\chi_0$ (0.2 in units of the Habing (1968) field). We run two additional models, the first with a somewhat smaller $\chi = 0.75\,\chi_0$ (Model #3a) and a second with an intensity following Bergin et al. (2006) ($\chi = 0.12\,\chi_0$; Model #3b). All other model parameters are the same as for Model #2b. The observed CO line profiles and the model line profiles are shown in Figure 2.10, and the radial profiles of the line-integrated intensity are given in Figure 2.11. We excluded the lower half of the Barnard 68 data from comparison to the CO data because of the significant deviation from the spherical symmetry, visible in the dust extinction maps (Alves et al., 2001).

While the line intensities of both species, [C I] and CO, are reduced for a smaller χ, the [C I] emission is more sensitive to the intensity of the external FUV field than the CO rotational transitions. A weaker FUV radiation field significantly decreases

the gas temperature at the cloud surface (Figure 2.9a) but does not change the C^0 density appreciably (Figure 2.9b). Generally, the gas temperature in the models is below 23.6 K, the excitation energy of the carbon $^3P_1$ level above the ground state. In this domain the [C I] line intensity is very sensitive to the temperature and thus to χ. In contrast, reducing the FUV intensity results only in small changes of the gas temperature in the region where CO is the most abundant carbon species and thus has a correspondingly small impact on the optically thick CO lines. The exception is Model # 3b with an extremely low FUV radiation field of $\chi = 0.12\,\chi_0$. In this case the cosmic-ray heating prevails already at $A_v \gtrsim 0.4$, with even *lower* temperatures closer to the surface (Figure 2.9).

The strength of the FUV radiation field also influences the self-absorption in the ^{12}CO $J = 2 \rightarrow 1$ and $J = 3 \rightarrow 2$ line profiles of the model because it depends on the gas temperature at the cloud surface. As these transitions are sub-thermally excited in the lower-density gas near the cloud edge, the reduction of the gas temperature in the low-FUV model results in stronger self-absorption (Figure 2.10; thin dotted lines).

The lower FUV intensity significantly reduces the [C I] and ^{13}CO emission. The model with $\chi = 0.12\,\chi_0$ (Model #3b) reproduces the observed ^{13}CO intensities and line-integrated intensity profiles to within ∼40%, confirming the results by Bergin et al. (2006). However, this model cannot account for the observed [C I] and ^{12}CO emission, which is underestimated by as much as a factor of 2. Additionally, we note that models with a low FUV radiation field produce clear self-absorption in the ^{12}CO $J = 2 \rightarrow 1$ and $J = 3 \rightarrow 2$ line profiles, which is not observed. The model with a slightly reduced FUV radiation field ($\chi = 0.75\,\chi_0$; Model #3a) reduces the [C I] and ^{13}CO emission by 10% compared to the $\chi = 1.0\,\chi_0$ model. While the ^{12}CO model intensity still marginally agrees with the data, the ^{13}CO emission is significantly more intense than observed. Any further reduction brings the ^{13}CO model intensity closer to the observations, but at the same time produces [C I] and ^{12}CO intensities that are too small.

We notice that the model predictions for the ^{12}CO $J = 1 \rightarrow 0$ integrated intensity profile show larger discrepancies at radii between 90″ and 150″. This is possibly due to deviations from spherical symmetry at angular scales $\lesssim 60''$ (note, for example, the deviations of the iso-intensity contours from circular symmetry in Figure 2.7; recall that we excluded the southern half of Barnard 68 for the same reason). These deviations are therefore more noticeable in the high-angular resolution ^{12}CO $J = 1 \rightarrow 0$ map than in the KOSMA maps (angular resolution 130″). We checked for any possible contribution from stray-emission picked up by the Mopra error beam (∼60″, Ladd et al. 2005) and concluded that this cannot account for any significant fraction of the excess emission observed at $90'' \lesssim r \lesssim 150''$. Also note that emission from a low-A_v region at $100 \lesssim r \lesssim 120$ (Figure 2.6) cannot account for this excess (see discussion in Section 2.4.1).

Tab. 2.4: *Predicted line integrated intensity toward Barnad 68 center*

Species Transition	Resolution - Instrument	Intensity (10^{-7} erg s^{-1} cm^{-2} sr^{-1})			
		Model #1a	Model #1b	Model #2b	Model #3a
[C II] $^2P_{3/2} \rightarrow ^2P_{1/2}$	18″-GREAT-SOFIA	9.49	9.49	4.77	2.44
	13″-HIFI-Herschel	9.47	9.47	4.76	2.43
[C I] $^3P_2 \rightarrow ^3P_1$	25″-NANTEN2	2.83	2.86	6.65	5.43
	25″-HIFI-Herschel				
	8″-APEX	2.83	2.86	6.62	5.40
^{12}CO $J = 5 \rightarrow 4$	39″-HIFI-Herschel	2.49	2.38	1.60	1.37
	56″-CASIMIR-SOFIA	2.51	2.39	1.61	1.37
^{12}CO $J = 4 \rightarrow 3$	17″-APEX-CSO	2.22	2.12	1.83	1.56
	45″-NANTEN2	2.23	2.13	1.84	1.56

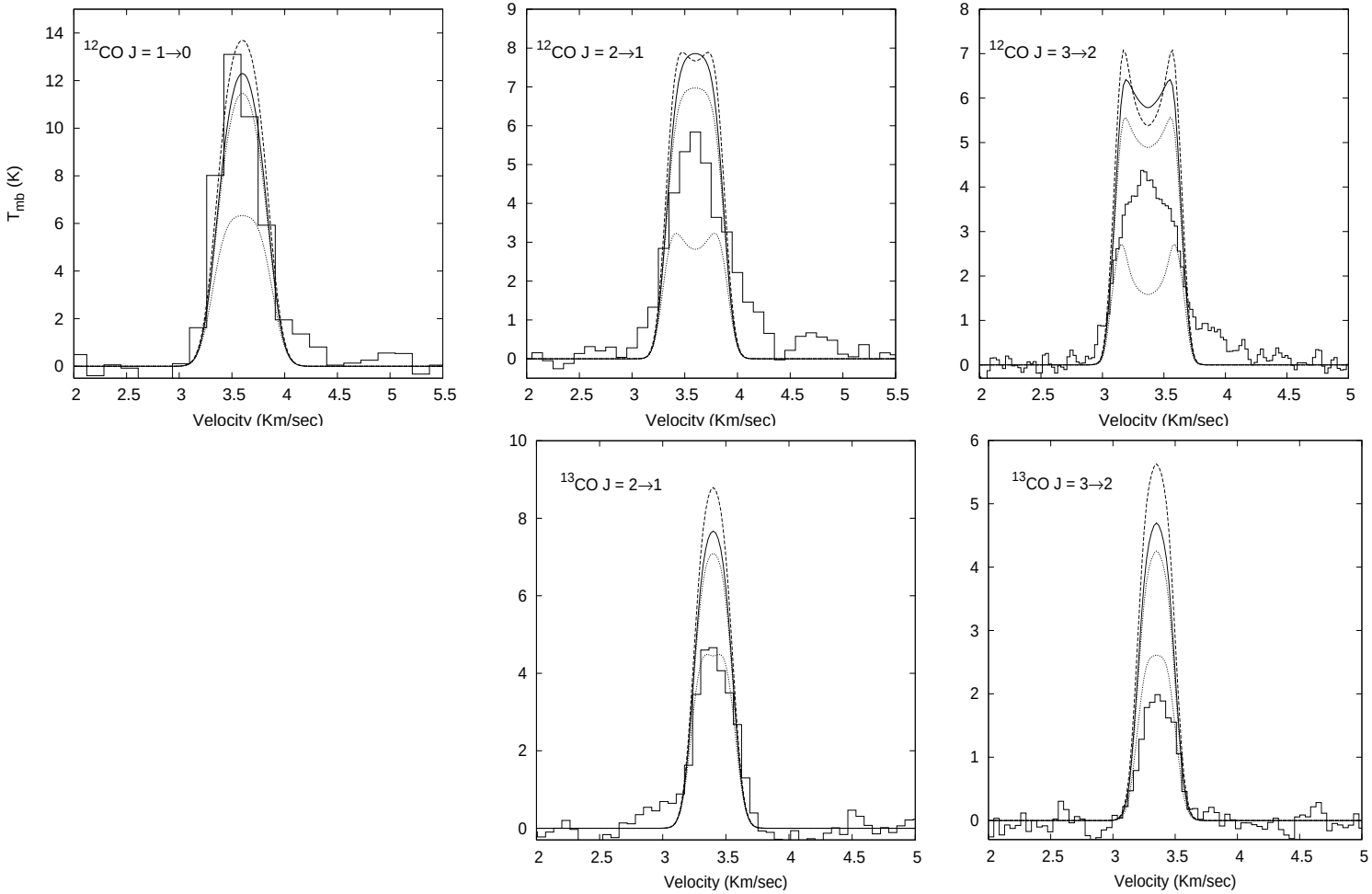

Fig. 2.10: *Observed line profiles compared with Model #1b (dashed), #2b (solid),#3a (thick dotted), and #3b (thin dotted). The transitions are indicated in the upper left corner of each panel.*

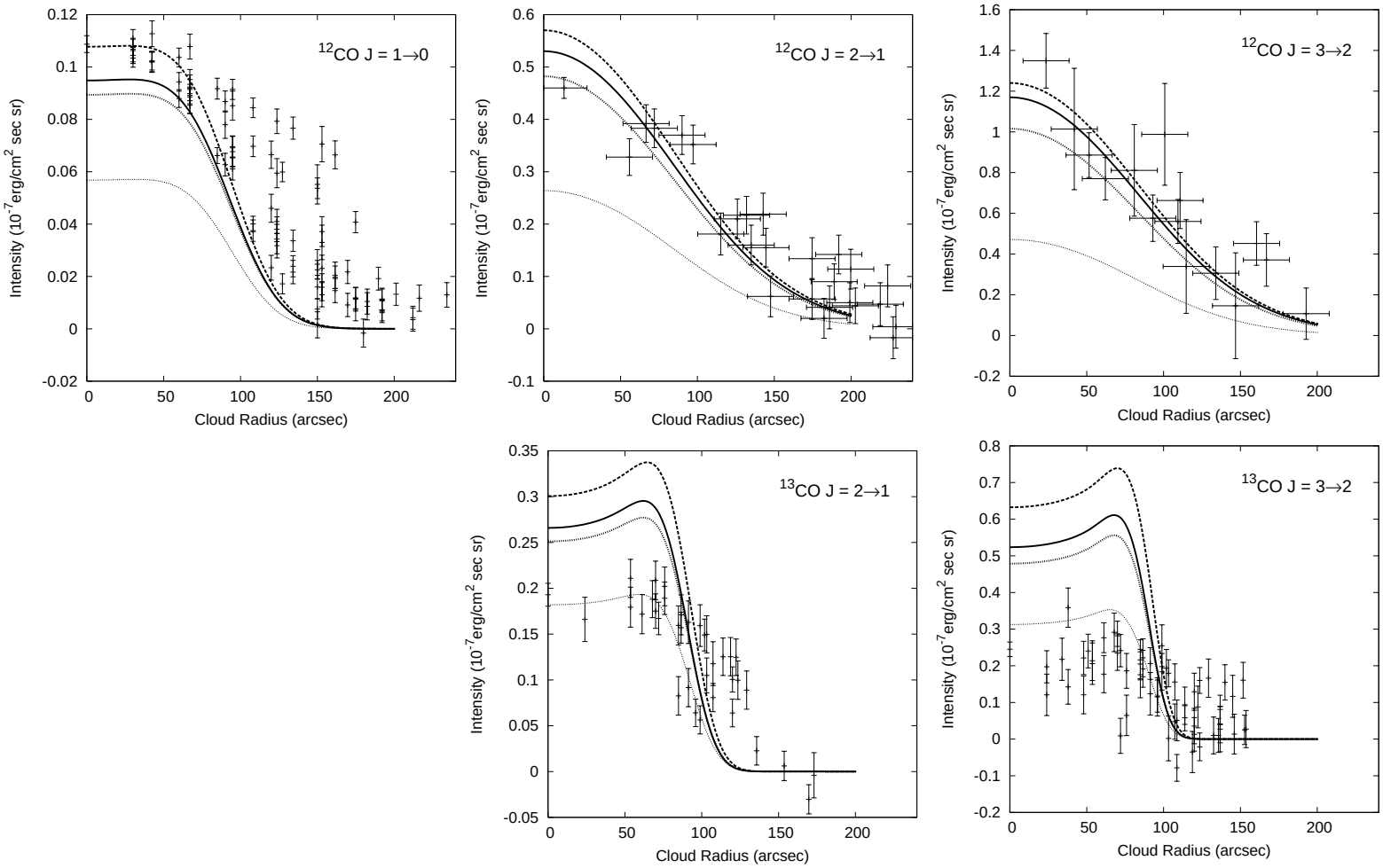

Fig. 2.11: *Line-integrated intensities as a function of cloud radius. The transitions are indicated in the upper right corner of each panel. The observations (error bars) are compared with predictions for Model #1b (dashed), #2b (solid),#3a (thick dotted), and #3b (thin dotted). Horizontal error bars in the* ^{12}CO $J = 2 \rightarrow 1$ *and* $J = 3 \rightarrow 2$ *emission correspond to the uncertainly in the correction for the receiver beam offset for the KOSMA observations (see Section 4.3).*

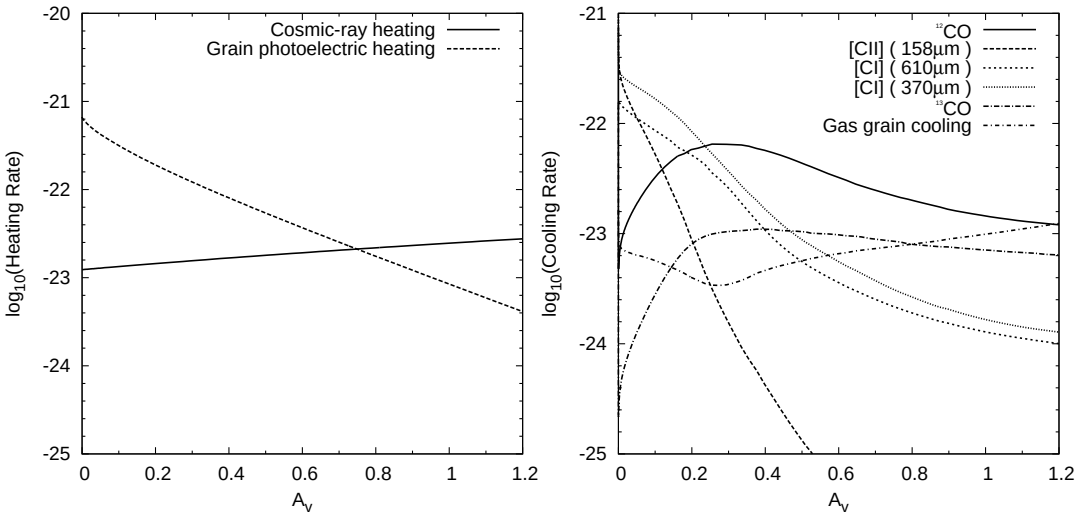

Fig. 2.12: *Dominant heating and cooling processes for Model #3a.The heating and cooling rates are in units of erg s^{-1} cm^{-3}.*

2.5 Discussion

2.5.1 Influence of the radiation field

We conclude that for the given density profile of Barnard 68 it is not possible to find a PDR model that matches all observations. The main difficulty is to simultaneously match the ^{12}CO and ^{13}CO transitions. The weak ^{13}CO lines suggest a low FUV intensity of $\chi = 0.12\,\chi_0$, but underestimate the [C I] and ^{12}CO intensity by up to a factor of 2 and produce deep self-absorbed ^{12}CO line profiles towards the cloud center. The ^{12}CO and [C I] intensities suggest a moderately reduced FUV field, $\chi = 0.75\,\chi_0$. However, this overestimates the ^{13}CO intensity by a factor of 2. A smaller impact is noticed by including PAHs in the chemical network of the model. The [C I] intensity is increased by 60%, while the CO intensity is reduced by 20%. PAHs help to remove or reduce the self-absorption and make the line profiles more consistent with the observations. Finally, we note that depletion affects the observed transitions only to a small degree.

Observations of higher–J CO, [C I] $^3P_2 \rightarrow {}^3P_1$, and [C II] transitions are useful to discriminate between the impact of relevant model parameters and to check whether the low ^{13}CO intensities indeed result from a low FUV field. They will also allow to better assess the impact of PAHs and/or depletion due to freezing on dust even at the cloud surface. Predictions for Model #1b, #2b, #3a, and #3b are listed in Table 3.14 for observations with present and future observatories. The impact of PAHs is a reduction of the [C II] intensity by a factor of 2, while the [C I] $^3P_2 \rightarrow {}^3P_1$ intensity is increased by the same factor. Because of their high excitation energy, both the [C II] and [C I] $^3P_2 \rightarrow {}^3P_1$ transitions also show a high sensitivity to the FUV field. They are reduced

Tab. 2.5: *Line-integrated intensity averaged over the projected clump area for Model #3a ($\chi = 0.75\chi_0$).*

Species Transition	Intensity (10^{-7} erg s^{-1} cm^{-2} sr^{-1})
[C II] $^2P_{3/2}\rightarrow{}^2P_{1/2}$	3.94
[C I] $^3P_1 \rightarrow{}^3 P_0$	3.76
[C I] $^3P_2 \rightarrow{}^3 P_1$	6.95
^{12}CO $J = 3 \rightarrow 2$	1.19
^{12}CO $J = 4 \rightarrow 3$	1.38
^{12}CO $J = 5 \rightarrow 4$	1.13
^{13}CO $J = 2 \rightarrow 1$	0.23
^{13}CO $J = 3 \rightarrow 2$	0.45
^{13}CO $J = 4 \rightarrow 3$	0.30

by up to a factor of 2 when the FUV field is reduced to $\chi = 0.75\chi_0$, and by as much as a factor of 7300 for $\chi = 0.12\chi_0$. The ^{12}CO $J = 5 \rightarrow 4$ and $J = 4 \rightarrow 3$ line intensities are more moderately reduced. Together, the inclusion of PAHs and a somewhat lower FUV field ($\chi = 0.75\chi_0$) reduce them by 40%.

The detection of the ^{12}CO $J = 4 \rightarrow 3$ with (with APEX, NANTEN2) and ^{12}CO $J = 5 \rightarrow 4$ (with HIFI Herschel, GREAT SOFIA) transitions can be obtained within a few minutes or less of observing time. A substantially longer integration time is required for the [C II] $^2P_{3/2}\rightarrow{}^2P_{1/2}$ transitions. The detection of the [C I] $^3P_2\rightarrow{}^3P_1$ transition might also prove very difficult from ground based observatories. However, with HIFI-Herschel, the [C I] $^3P_2\rightarrow{}^3P_1$ transition can be detected in less than a minute.

2.5.2 Heating and cooling

In Figure 2.12 we show the heating and cooling for different processes as a function of the visual extinction A_v (Model #3a, $\chi = 0.75\chi_0$). Photoelectric heating dominates the gas heating at $A_v \lesssim 0.8$, being replaced by cosmic-ray heating at larger depths. Gas cooling is governed by the [C I] $^3P_1\rightarrow{}^3P_0$ and $^3P_2\rightarrow{}^3P_1$ fine structure transitions for $A_v < 0.2$, and by the ^{12}CO (and ^{13}CO) rotational transitions for $0.2 < A_v < 1.2$. Gas-grain coupling dominates at $A_v > 1.2$. It is interesting to note that the [C II] transition does not dominate the cooling in this case, even very close to the cloud surface (C^+ dominates only at $A_v \lesssim 0.05$).

Table 2.5 lists the clump-averaged line emission for Model #3a ($\chi = 0.75\chi_0$). The [C I] fine structure transitions dominate with a total intensity of 1.1×10^{-6} erg s^{-1} cm^{-2} sr^{-1}, followed by the ^{12}CO and ^{13}CO rotational transitions with a total intensity of 4.7×10^{-7} erg s^{-1} cm^{-2} sr^{-1}. The [C II] $^2P_{3/2}\rightarrow{}^2P_{1/2}$ fine structure transition contributes with a total intensity of 3.9×10^{-7} erg s^{-1} cm^{-2} sr^{-1}. This relatively low value is attributed to

the low FUV radiation field of Model #3a and to the presence of PAHs in the chemical network of the model, which significantly decreases the abundance of C^+ close to the surface of the cloud.

2.6 Summary and Conclusions

We present simulations using a spherical PDR code to model the line emission in Barnard 68. Its approximately spherical geometry makes Barnard 68 an ideal test for such a spherically-symmetric PDR model. We compare the model results with the line profiles and the azimuthally averaged intensity profiles of the three lowest rotational transitions of ^{12}CO, ^{13}CO $J = 3 \rightarrow 2$, $J = 2 \rightarrow 1$, and the spatially and spectrally unresolved [C I] $^3P_1 \rightarrow {}^3P_0$ transition. This is the first time that a spherical PDR code was used to model the line emission in a low-FUV cloud in such a detail.

We have tested the impact of including PAHs in the chemical network of the model, reducing the FUV radiation field, and considering the effects of depletion in the emerging model line intensities. We find it difficult to simultaneously model the observed ^{12}CO and ^{13}CO emission, with residual differences up to a factor of 2 between PDR models and observed line intensities. They seem to require a steep drop in either the excitation conditions or in the abundances in a layer between the regions which dominate the ^{12}CO and ^{13}CO emission, respectively. While the ^{13}CO observations argue for either a low abundance and low excitation (Bergin et al., 2006), a model with a low external FUV field is clearly incompatible with the ^{12}CO and [C I] observations. We find evidence that PAHs play a role in the chemical network. This results in a larger C^0 layer, while the C^+ layer is very thin making the [C II] emission very faint and difficult to discriminate from emission from the ambient Warm Ionized Medium (WIM) in spectrally unresolved observations. Depletion is not likely to play an important role in the observed transitions.

Observations with the current and future telescopes (NANTEN2, APEX, SOFIA, Herschel) will allow a test of our results and assess the importance of different model parameters.

3 Molecular Gas in Intermediate Velocity Clouds

3.1 Introduction

Intermediate-velocity clouds (IVCs) are clouds at high Galactic latitudes which have radial velocities that deviate from the normal Galactic rotation. Originally observed in neutral hydrogen (H I) surveys, they are distinguished from High Velocity Clouds (HVC) by an arbitrary velocity threshold defined by $|v_{lsr}|$ =100 km s^{-1} (Wesselius & Fejes, 1973; Kuntz & Danly, 1996). A lower limit to the distance of 200 pc was found for IVCs, suggesting that their *z*-distances to the Galactic mid-plane is more than one scale height of the molecular gas (Gladders et al., 1999), but they are closer than HVCs (Wakker, 2001). This suggests that IVC clouds are located at the boundary between the Galactic disk and the Galactic halo and that they seem to be falling into the Galactic gaseous disk (Gladders et al., 1999). This idea is supported by the observed morphology in some IVCs which resembles the asymetric intensity distribution of shocked material (Weiß et al., 1999).

Intermediate-velocity clouds have visual extinctions which are similar to those found in translucent clouds ($A_v \simeq 1-5$ mag), while they show metallicities between 50-100% solar (Wakker, 2001). In this visual extinction regime, the chemistry and thermal balance of the clouds are dominated by the influence of stellar far-ultraviolet (FUV) photons. Therefore, IVCs can be studied as Photon Dominated Regions (PDRs) exposed to the mean interstellar FUV radiation field ($\chi_0 = 2.7\times10^{-3}$ erg cm^{-2} sec^{-1}, Draine 1978), as they are generally not associated with star formation. As PDR models suggest, the transition between C^+/C^0/CO occurs at $A_v \simeq 1-5$ mag, hence IVCs are traced by fine-structure transitions of C^+ and C as well as by rotational transitions of CO and its isotopomers.

Molecular hydrogen has been detected in absorption toward few IVCs, with H_2 column densities ranging from $\sim10^{14}$ cm^{-2} to $\sim10^{17}$ cm^{-2} (Richter et al., 2003; Wakker, 2006). They have been also detected in CO (Mebold et al., 1985; Heiles et al., 1988; Weiß et al., 1999; Heithausen et al., 2001; Desert et al., 1990). Heithausen et al. (2001) have detected the ^{12}CO $J = 3 \rightarrow 2$ and ^{12}CO $J = 2 \rightarrow 1$ rotational transitions and the [C I] $^3P_1-^3P_0$ fine structure transition toward IVC 135+54-46. The PDR models presented by Heithausen et al. (2001) suggest a relatively high gas density of few times 10^4 cm^{-3}.

In this section, we present observations of the three lowest rotational transitions of ^{12}CO and ^{13}CO as well as the [C I] $^3P_1-^3P_0$ fine structure transition of neutral carbon in the intermediate-velocity cloud IVC210. Observations of the three lowest rotational transitions of ^{12}CO and ^{13}CO are also presented for the intermediate-velocity cloud IVC140. Based on these observations, the physical conditions are derived using an escape probability model. Additionally, a self-consistent solution of the chemical structure (abundances of species) and of the temperature (thermal balance of the gas) is given using a photon-dominated-region code.

The present study enlarges the avaliable sample of IVCs observed in CO and [C I] and aims at understanding the properties of the molecular gas in this type of clouds. In addition, as the low-metallicity gas in IVCs is exposed to weak FUV radiation fields, we have the opportunity here to study how the metallicity influences the properties of the ISM without any strong influence of a FUV radiation field.

The observations are described in Section 3.3. The analysis of the observations is presented in Section 3.4 and discussed in Section 3.5. A summary is presented in Section 3.6.

3.2 IVC210 and IVC140

The intermediate-velocity cloud IVC210 was originally observed in neutral atomic hydrogen (H I) surveys (Meng & Kraus, 1970; Verschuur, 1971; Wesselius & Fejes, 1973; Heiles & Habing, 1974). It was later observed in the infrared continuum emission (IRAS, Desert et al., 1988) and in CO (Desert et al., 1990). Observations of the calcium absorption line (3933Å) in the nearby cloud IVC NHX 210+70-40 indicate a distance to IVC210 between 12 and 400 pc (Wesselius & Fejes, 1973). In the following, we adopt a distance of 100 pc to IVC210, as this is the value assumed by Desert et al. (1988). The emerging emission in IVC210 shows double-peaked line profiles in all observed transitions, with components at -41 km s^{-1} (C#1) and -38 km s^{-1} (C#2).

The intermediate-velocity cloud IVC140 was originally observed in H I, CO, and in the infrared continuum emission (IRAS) by Heiles et al. (1988). Its distance is estimated to be between 129 to 257 pc (Burns et al., 2003). In this chapter, we choose an intermediate value for the distance to IVC140 of 200 pc. The local standard of rest (LSR) velocity of this cloud is -14 km s^{-1}.

3.3 Observations

We present observations of the three lowest rotational transitions of ^{12}CO and ^{13}CO in IVC210 and IVC140, and of the [C I] $^3P_1 \rightarrow {}^3P_0$ fine structure transition in IVC210. A summary of the observations is presented in Table 3.6.

Maps of the ^{12}CO $J = 2 \rightarrow 1$ (230 GHz) and $J = 3 \rightarrow 2$ (345 GHz) rotational transitions toward IVC210 and IVC140 were made using the 230/345 GHz dual-channel receiver, installed in the KOSMA 3-m telescope. The parameters of the observations are listed in Table 3.6. The central positions of the maps are $\alpha = 10^h50^m22\overset{''}{.}0$ and $\delta = 25°12'13\overset{''}{.}0$ (B1950) for IVC210 and $\alpha = 10^h49^m40\overset{''}{.}0$ and $\delta = 64°38'48\overset{''}{.}01$ (B1950) for IVC140. The ^{12}CO $J = 3 \rightarrow 2$ spectra were convolved to an angular resolution of $130''$ in order to match the KOSMA 3-m beam at 230 GHz. The ^{13}CO $J = 2 \rightarrow 1$ (220 GHz) transition was observed toward IVC210 with a cross-cut centered on the position defined above.

The ^{13}CO $J = 2 \rightarrow 1$ (220 GHz) transition was not detected in IVC140. For all observed transitions, a straight line was fitted and subtracted to the baseline of each spectrum. The spectra obtained with KOSMA are shown in Figs. 3.13 and 3.14.

High-angular resolution maps were made for the two lowest transitions of ^{12}CO and ^{13}CO toward IVC210 and IVC140 using the IRAM 30-m telescope in the on-the-fly (OTF) mapping mode. The central position of the IVC210 map is located at $\alpha = 10^{\rm h}50^{\rm m}21\overset{\prime\prime}{.}1$ and $\delta = 25^\circ12'06\overset{\prime\prime}{.}4$ (B1950). In case of the IVC140, the observed map is centered on $\alpha = 10^{\rm h}49^{\rm m}39\overset{\prime\prime}{.}12$ and $\delta = 64^\circ38'18\overset{\prime\prime}{.}89$ (B1950). After fitting and subtracting straight lines to the baselines of the spectra, the originally oversampled OTF scans were re-gridded to a regular grid of 12″ spacing for the ^{12}CO and ^{13}CO $J = 1 \rightarrow 0$ transitions, and to a 6″ spacing for the ^{12}CO and ^{13}CO $J = 2 \rightarrow 1$ transitions. In both clouds the ^{13}CO $J = 2 \rightarrow 1$ transition was not detected. The ^{12}CO $J = 2 \rightarrow 1$ and ^{13}CO $J = 2 \rightarrow 1$ maps were convolved to a 22″ angular resolution. The maps of integrated intensity are shown in Figs. 3.15 and 3.16.

The region observed in IVC210 was also mapped in the ^{12}CO $J = 3 \rightarrow 2$ rotational transition using the JCMT 15-m telescope. The spectra were observed in raster mapping mode. Straight lines are fitted and subtracted to the baseline of each spectrum, and the map is convolved to 22″ resolution in order to compare it with the ^{12}CO $J = 1 \rightarrow 0$ and ^{12}CO $J = 2 \rightarrow 1$ transitions, respectively. The spectral map of the ^{12}CO $J = 3 \rightarrow 2$ observations is shown in Fig. 3.17.

The [C I] $^3P_1$–$^3P_0$ (492 GHz) fine-structure transition of neutral carbon was mapped with the KOSMA 3-m telescope using the 2×4 pixel SubMillimeter Array Receiver for Two frequencies (SMART[3]) in IVC210. The fully sampled map was made using the OTF mapping mode. A straight line is fitted and subtracted from the baseline of spectra, and the observations are convolved to a 130″ resolution on a 40″ grid. The map is centered on a position offset by 80″ west from the ^{12}CO $J = 2 \rightarrow 1$ map made with the KOSMA 3-m telescope. The SMART receiver was set up to simultaneously observe the [C I] $^3P_1$–$^3P_0$ (490 GHz) and $^3P_2$–$^3P_1$ (810 GHz) fine structure transitions. No emission was detected for the latter transition. The observed [C I] $^3P_1$–$^3P_0$ spectra are shown in Fig. 3.18.

[3] See Graf et al. (2003) for additional details about the SMART receiver.

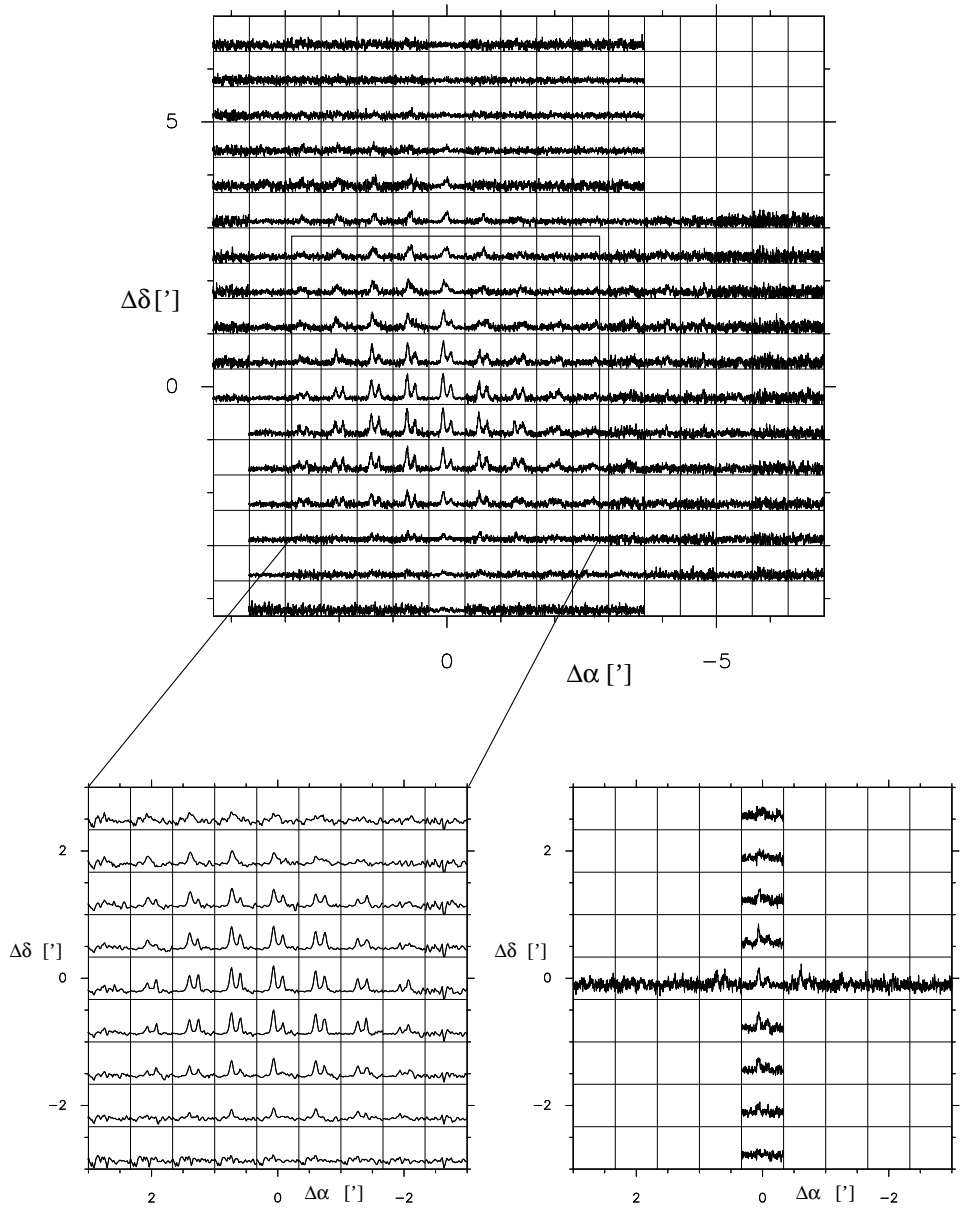

Fig. 3.13: *Observations of the* ^{12}CO $J = 2 \rightarrow 1$ *(upper panel),* $J = 3 \rightarrow 2$ *(lower left panel), and* ^{13}CO $J = 2 \rightarrow 1$ *(lower right panel) rotational transitions made with the KOSMA 3-m telescope toward IVC210. A cross-cut centered in this region was made for the* ^{13}CO $J = 2 \rightarrow 1$ *transition. The main-beam temperature scale is* $T_{\rm mb} = -0.3 \ldots 2.3$ *K for* ^{12}CO $J = 2 \rightarrow 1$, $T_{\rm mb} = -0.3 \ldots 1.1$ *K for* ^{12}CO $J = 3 \rightarrow 2$, *and* $T_{\rm mb} = -0.15 \ldots 0.35$ *K for* ^{13}CO $J = 2 \rightarrow 1$. *The offsets are given in arcminutes. The velocity range in all spectra is* $v = -48 \ldots -31$ *km* s^{-1}. *All observed positions are on a 40′ grid.*

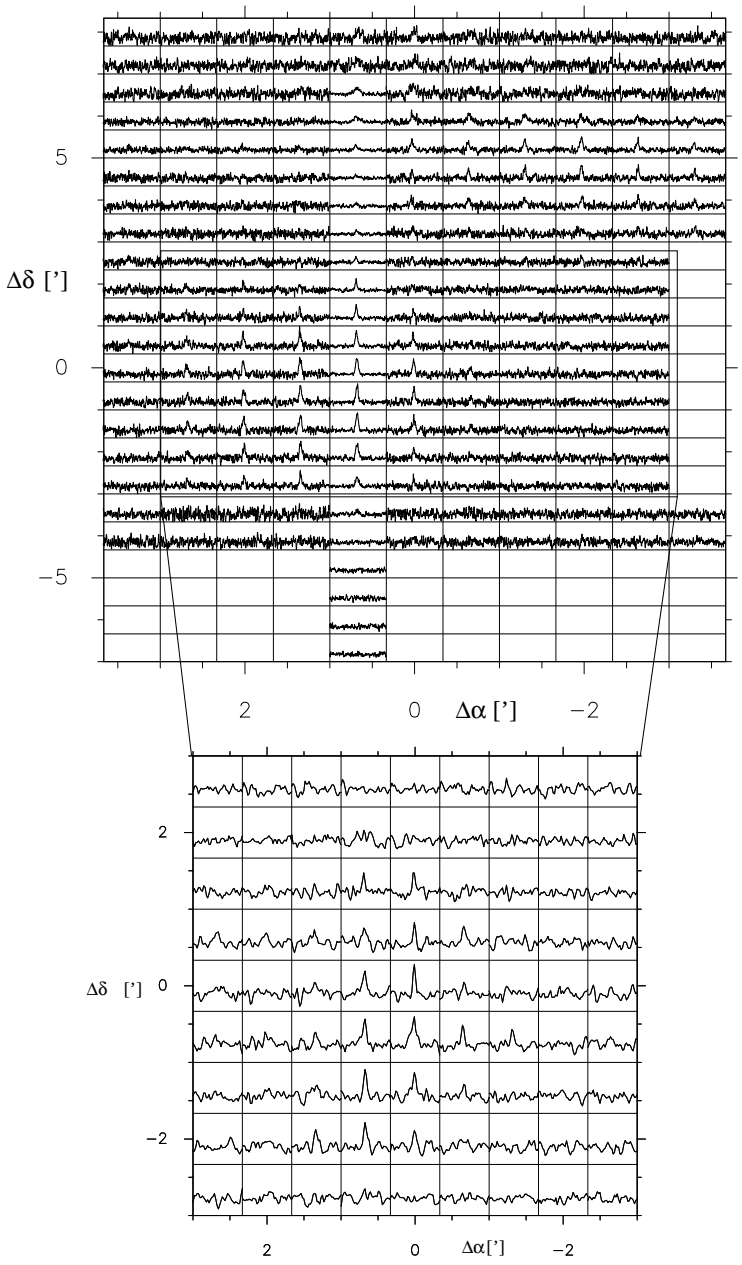

Fig. 3.14: *Observations of the ^{12}CO $J = 2 \rightarrow 1$ (upper panel), $J = 3 \rightarrow 2$ (lower panel) rotational transitions observed with the the KOSMA 3-m telescope toward IVC140. The main-beam temperature scale is $T_{\rm mb} = -0.5 \ldots 1.4$ K for ^{12}CO $J = 2 \rightarrow 1$ and $T_{\rm mb} = -0.3 \ldots 0.6$ K for ^{12}CO $J = 3 \rightarrow 2$. The offsets are given in arcminutes. The velocity range in both maps is v $= -20 \ldots -7$ km s^{-1}. All observed positions are spaced in a 40″ grid.*

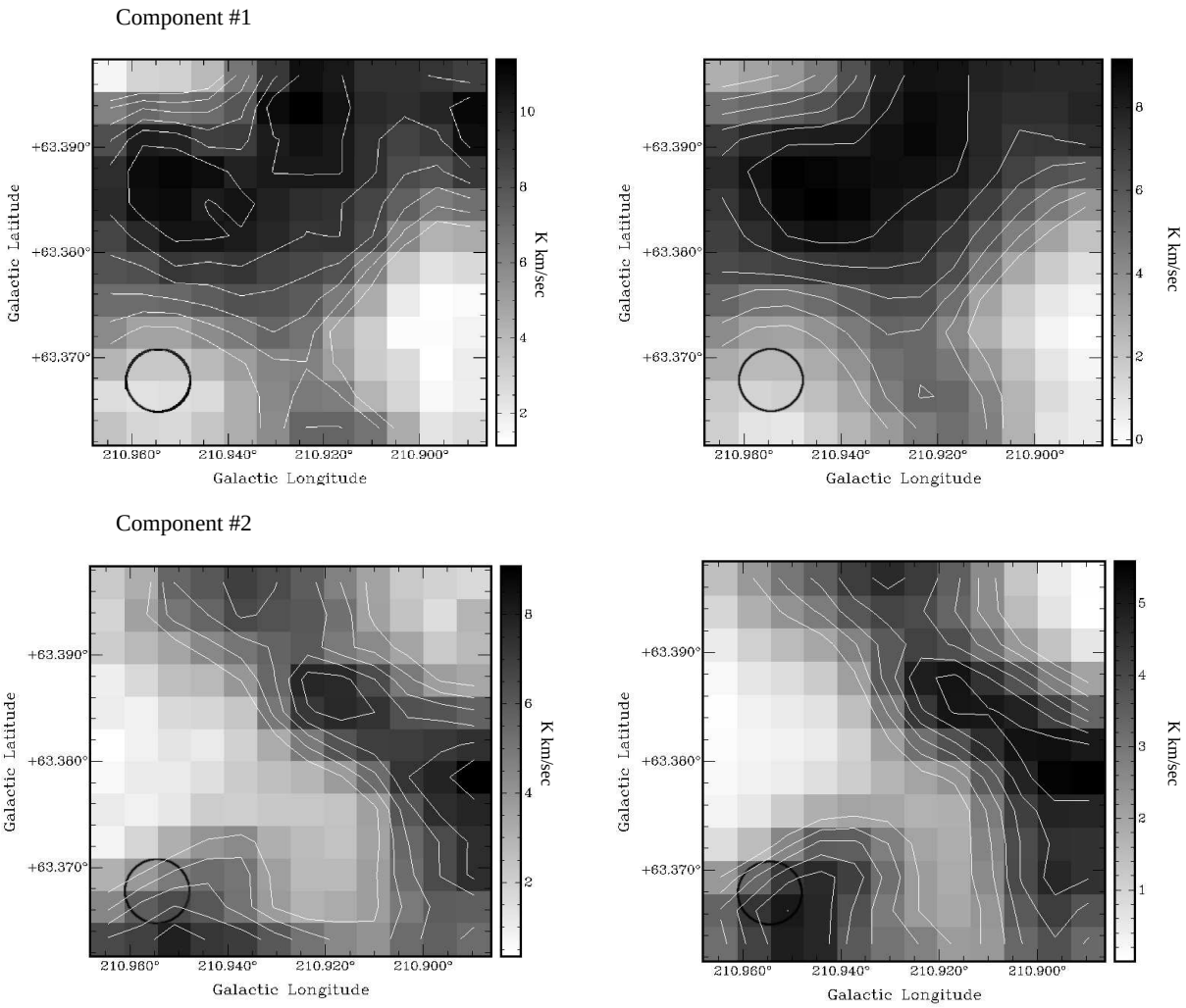

Fig. 3.15: *Integrated intensity maps of the* ^{12}CO $J = 1 \rightarrow 0$ *(left) and* $J = 2 \rightarrow 1$ *(right) rotational transitions observed with the IRAM 30-m telescope toward IVC210. The maps are split into Component #1 (integration range -40 to -44 km* s^{-1}*) and Component #2 (integration range -36.5 to -40 km* s^{-1}*). They correspond to a* $2'.5 \times 2'.5$ *field with an angular resolution of* $22''$ *for* ^{12}CO $J = 1 \rightarrow 0$ *and* $12''$ *for* ^{12}CO $J = 2 \rightarrow 1$*. In all maps the contours range from 40% to 90% of the peak intensity (11.4 and 9.1 K km sec*$^{-1}$ *for* ^{12}CO $J = 1 \rightarrow 0$ *and* $J = 2 \rightarrow 1$ *in Component #1, and 9.1 and 5.6 K km sec*$^{-1}$ *for* ^{12}CO $J = 1 \rightarrow 0$ *and* $J = 2 \rightarrow 1$ *in Component #2) in steps of 10%.*

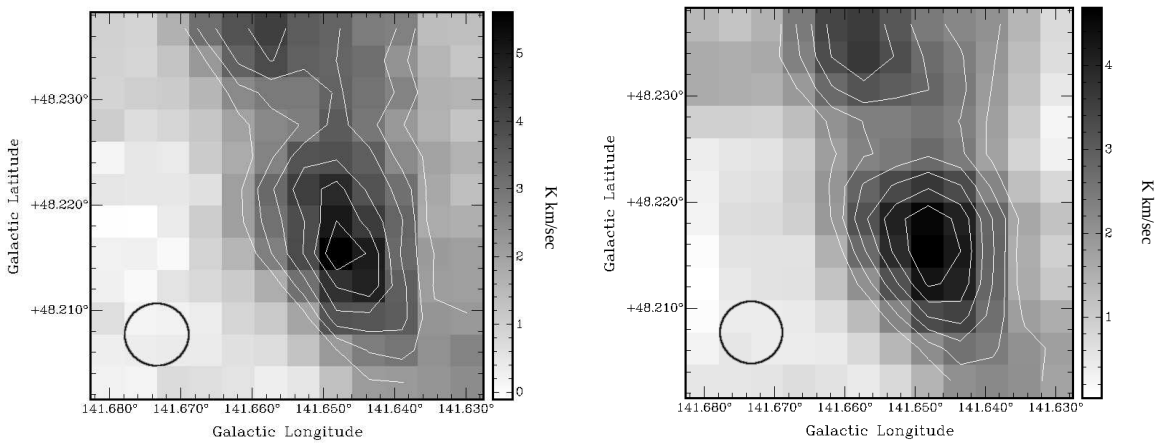

Fig. 3.16: *Integrated intensity maps of the* $^{12}CO\ J = 1 \rightarrow 0$ *(left) and* $J = 2 \rightarrow 1$ *(right) rotational transitions observed with the IRAM 30-m telescope toward IVC140. The panels correspond to a* $2'.5 \times 2'.5$ *field and the contours range from 40% to 90% of the peak emission (5.6 K km sec*$^{-1}$ *for* $^{12}CO\ J = 1 \rightarrow 0$ *and 4.7 K km sec*$^{-1}$ *for* $^{12}CO\ J = 2 \rightarrow 1$ *) in steps of 10%. The integration range is from -12.5 to -14.9 km s*$^{-1}$*. The maps have an angular resolution of* $22''$*.*

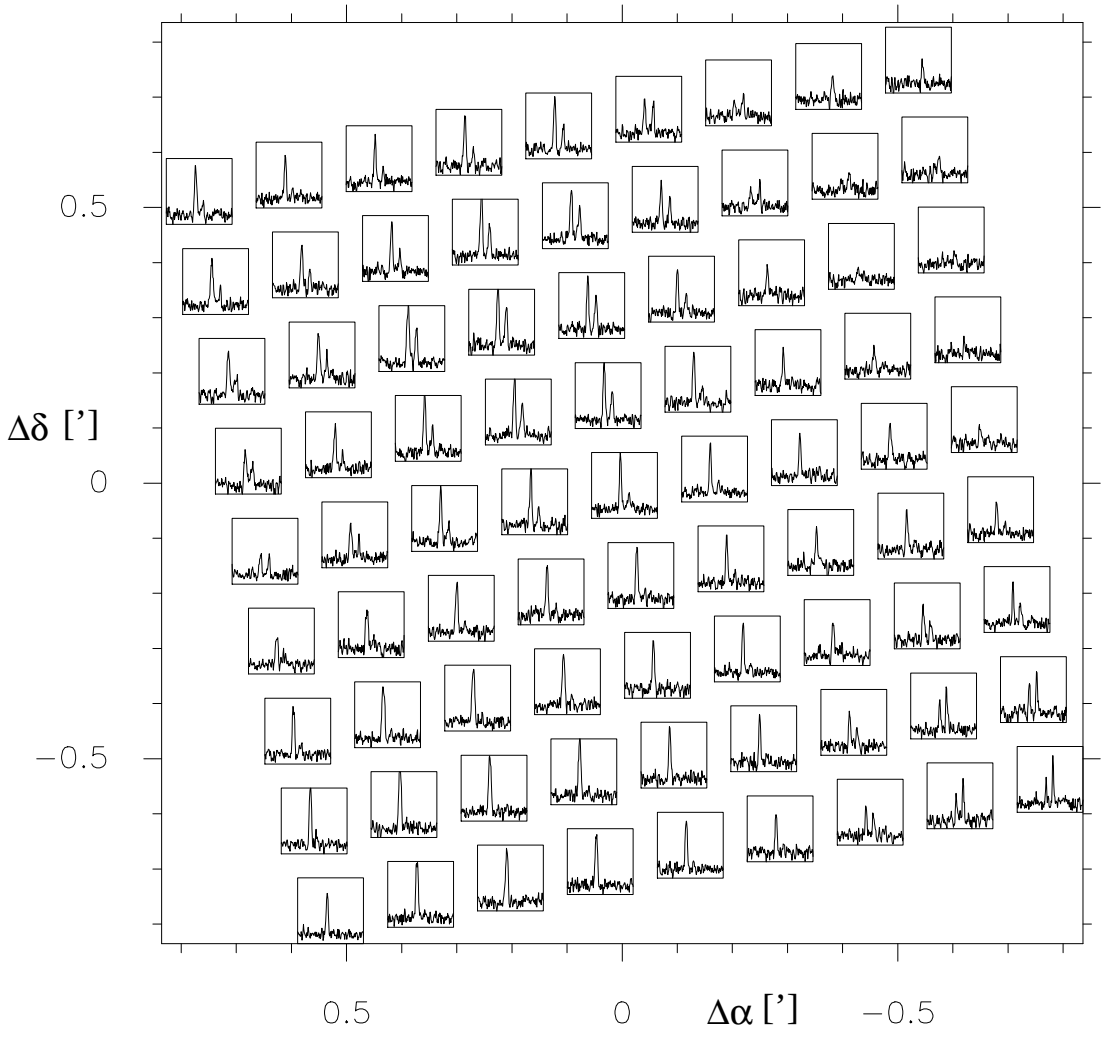

Fig. 3.17: *Spectra of the* ^{12}CO $J = 3 \rightarrow 2$ *transition toward IVC210. The velocity range is* $v = -55 \ldots -25$ *km sec*$^{-1}$ *and the main-beam temperature scale is* $T_{\rm mb} = -0.5 \ldots 3$ *K. The map was observed in epoch B1950.*

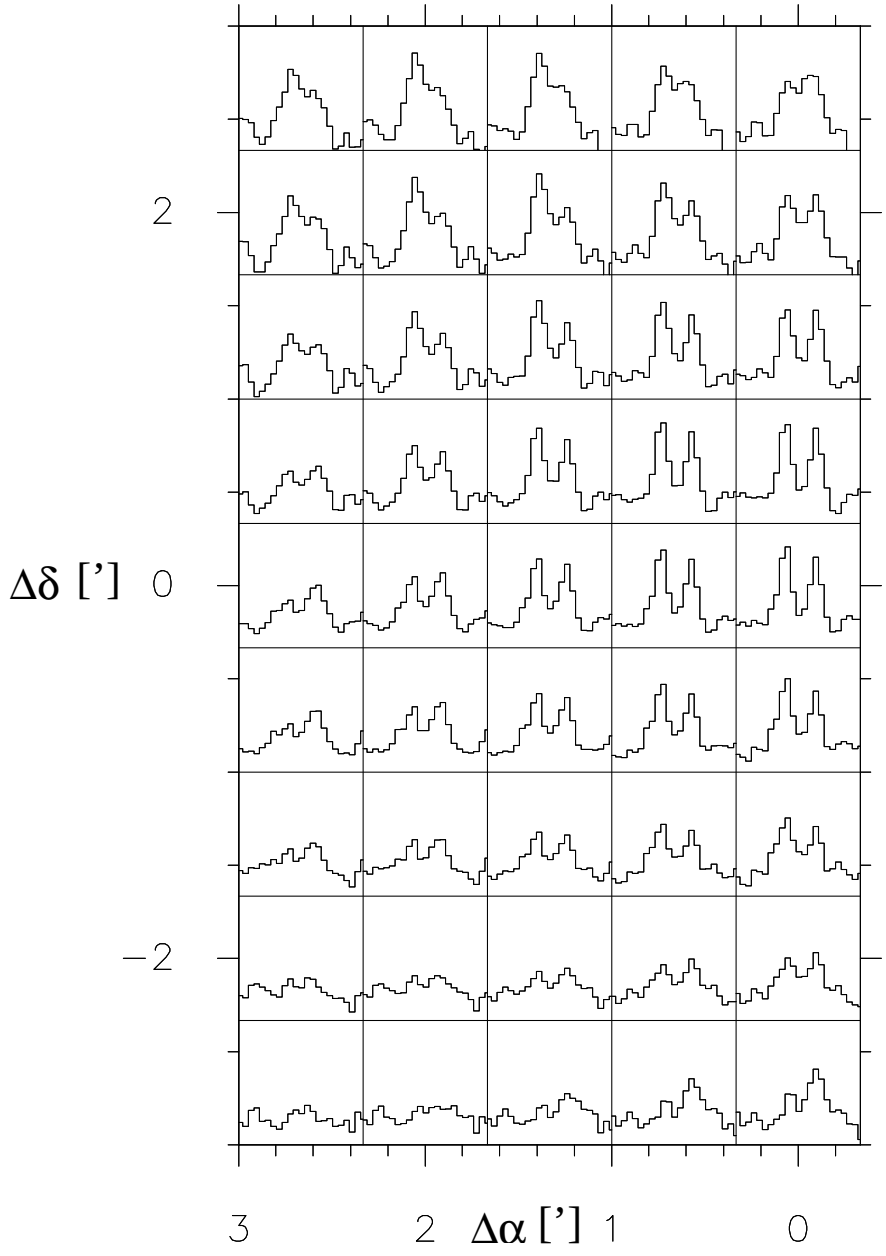

Fig. 3.18: *Spectra of the [C I] $^3P_1$-$^3P_0$ fine structure transition of neutral carbon toward IVC210 observed with the KOSMA 3-m telescope. The velocity range is* $v = -48 \ldots -34$ *km sec*$^{-1}$ *and the main-beam temperature scale is* $T_{\rm mb} = -0.05 \ldots 0.3$ *K.*

Tab. 3.6: *Spectral Line Observations Toward IVC Clouds*

Telescope	Transition	# of Pointings	Sampling [arcsec]	Map [arcmin^2]	θ_{mb} [arcsec]	η_{mb}	Δv [km sec^{-1}]	r.m.s. noise [K/Channel]
IVC210								
IRAM 30-m	^{12}CO $J = 1 \rightarrow 0$	144	12	$2\farcm5 \times 2\farcm5$	22	0.75	0.2	0.2
IRAM 30-m	^{12}CO $J = 2 \rightarrow 1$	576	6	$2\farcm5 \times 2\farcm5$	11	0.52	0.05	0.35
KOSMA	^{12}CO $J = 2 \rightarrow 1$	261	40	$11\farcm0 \times 11\farcm0$	130	0.76	0.05	0.16
JCMT	^{12}CO $J = 3 \rightarrow 2$	81	10	$1\farcm3 \times 1\farcm3$	14	0.56	0.2	0.2
KOSMA	^{12}CO $J = 3 \rightarrow 2$	261	40	$11\farcm0 \times 11\farcm0$	82	0.78	0.35	0.24
IRAM 30-m	^{13}CO $J = 1 \rightarrow 0$	144	12	$2\farcm5 \times 2\farcm5$	22	0.75	0.2	0.16
IRAM 30-m	^{13}CO $J = 2 \rightarrow 1$	546	6	$2\farcm5 \times 2\farcm5$	11	0.52	0.05	0.27
KOSMA	^{13}CO $J = 2 \rightarrow 1$	17	40	–[a]	130	0.76	0.05	0.2
KOSMA	[CI] $^3P_1 \rightarrow ^3P_0$	45	28	$6\farcm0 \times 3\farcm0$	55	0.62	0.623	0.036
IVC140								
IRAM 30-m	^{12}CO $J = 1 \rightarrow 0$	144	12	$2\farcm5 \times 2\farcm5$	22	0.75	0.2	0.21
IRAM 30-m	^{13}CO $J = 1 \rightarrow 0$	144	12	$2\farcm5 \times 2\farcm5$	22	0.75	0.2	0.16
IRAM 30-m	^{12}CO $J = 2 \rightarrow 1$	576	6	$2\farcm5 \times 2\farcm5$	11	0.52	0.05	0.2
KOSMA	^{12}CO $J = 2 \rightarrow 1$	204	40	$15\farcm0 \times 7\farcm0$	130	0.76	0.05	0.13
KOSMA	^{12}CO $J = 3 \rightarrow 2$	204	40	$15\farcm0 \times 7\farcm0$	82	0.78	0.35	0.24

[a] $6\farcm0 \times 6\farcm0$ cross-cut.

Tab. 3.7: *Cloud Properties*

Source	Distance [pc]	z-Distance [pc]	v_{lsr} [km s^{-1}]	Area [pc^2]	Mass[a] [$M_\odot$]
IVC210	100	89	-39	0.054	$(4.5 \pm 0.8) \times 10^{-3}$
IVC140	200	150	-14	0.078	$(2.2 \pm 0.3) \times 10^{-3}$

[a] Assuming a CO-to-H_2 conversion factor for the ^{12}CO $J = 2 \rightarrow 1$ transition of $X_{CO} = 0.24 \times 10^{20}$ cm^{-2} (K km s^{-1})$^{-1}$, Corneliussen 1996.

3.4 Analysis and Results

3.4.1 Cloud Properties

As the ^{12}CO $J = 2 \rightarrow 1$ observations made with the KOSMA 3-m telescope are extended and cover a large portion of the clouds, we utilize them in order to characterize some global properties of the molecular gas. A summary of these parameters is listed in Table 3.7.

The cloud area is calculated considering positions which have a ^{12}CO $J = 2 \rightarrow 1$ integrated intensity larger than three times the r.m.s noise. The total CO intensity is estimated by averaging all ^{12}CO $J = 2 \rightarrow 1$ spectra with integrated intensities above the 3σ level. Note that in case of IVC210, we include the two observed velocity components in the calculation of the total CO intensity. The resulting integrated intensity is then multiplied by the estimated cloud area in order to obtain an estimation of the ^{12}CO $J = 2 \rightarrow 1$ luminosity of the cloud. We convert the ^{12}CO $J = 2 \rightarrow 1$ luminosity to H_2 mass by applying a CO-to-H_2 conversion factor for this transition of 0.24×10^{20} cm^{-2} (K km s^{-1})$^{-1}$. This conversion factor was estimated in a translucent cloud by Corneliussen (1996). An additional correction for helium and other heavy elements of 1.36 is also applied (Allen, 1973). The resulting H_2 mass is $(4.5 \pm 0.8) \times 10^{-3}$ and $(2.2 \pm 0.3) \times 10^{-3}$ $M_\odot$ in IVC210 and IVC140, respectively. The derived mass in IVC210 is lower compared to that obtained by Desert et al. 1988 based on infrared observations (1.8 $M_\odot$) over the entire H I cloud. This can be due to the possibly low metallicity of the gas which can result in a reduction of the CO abundance relative to H_2. This potentially underestimates the total molecular mass when derived using CO observations, although it cannot be underestimated by more than a factor of 2, as the metallicity in IVCs is thought to be larger than 50% solar (Wakker, 2001). This suggests that the molecular gas traced by CO represents only a small portion of the entire H I cloud and therefore IVC clouds may represent clouds where molecular hydrogen is being formed.

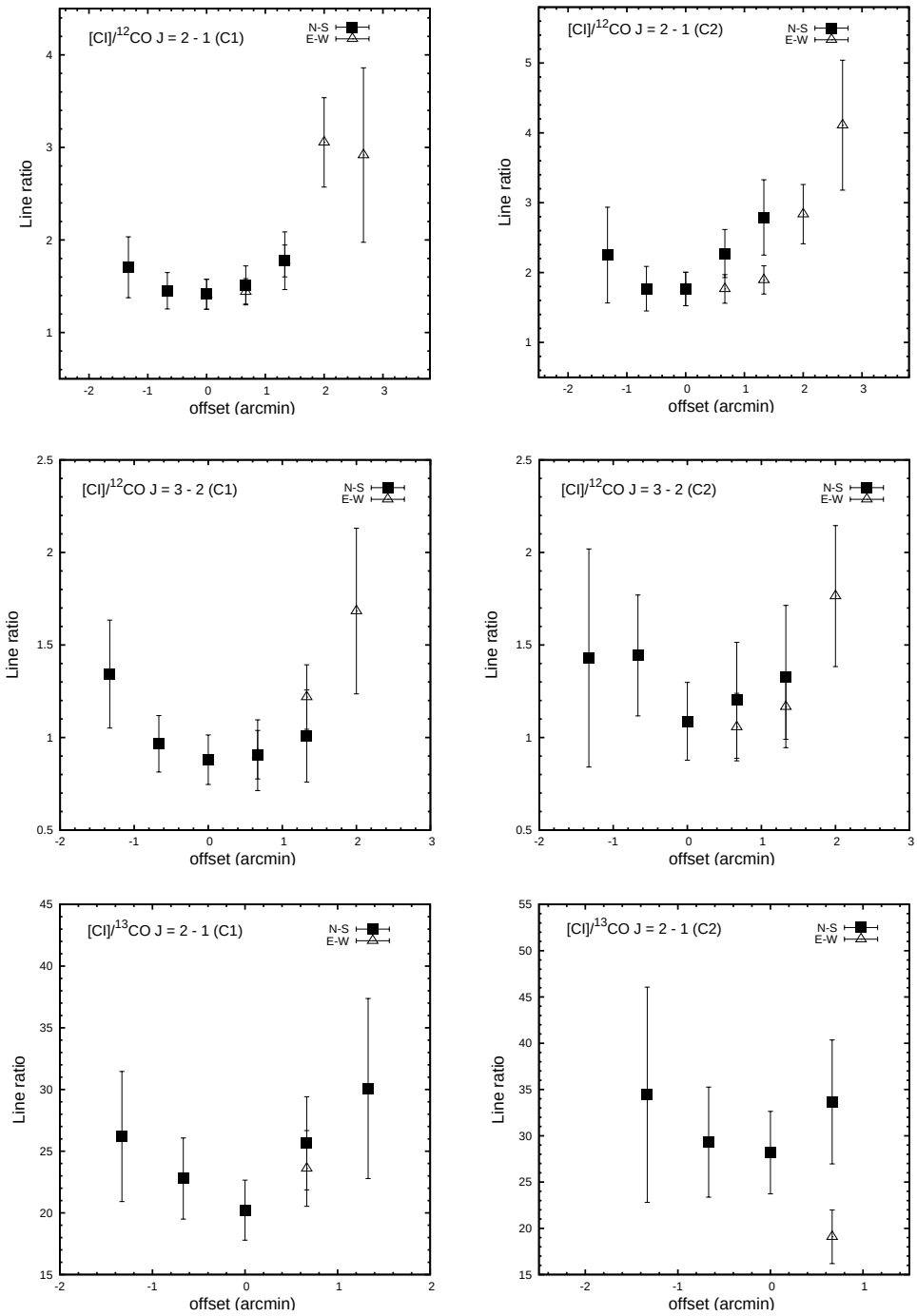

Fig. 3.19: *[CI]/^{12}CO and [CI]/^{13}CO line-integrated intensity ratios along E-W and N-S cuts in IVC210 (line intensity in units of erg cm^{-2} s^{-1} sr^{-1}). The left and right panels correspond to the observed components C#1 and C#2, respectively. The error bars represent the r.m.s. noise of the observations.*

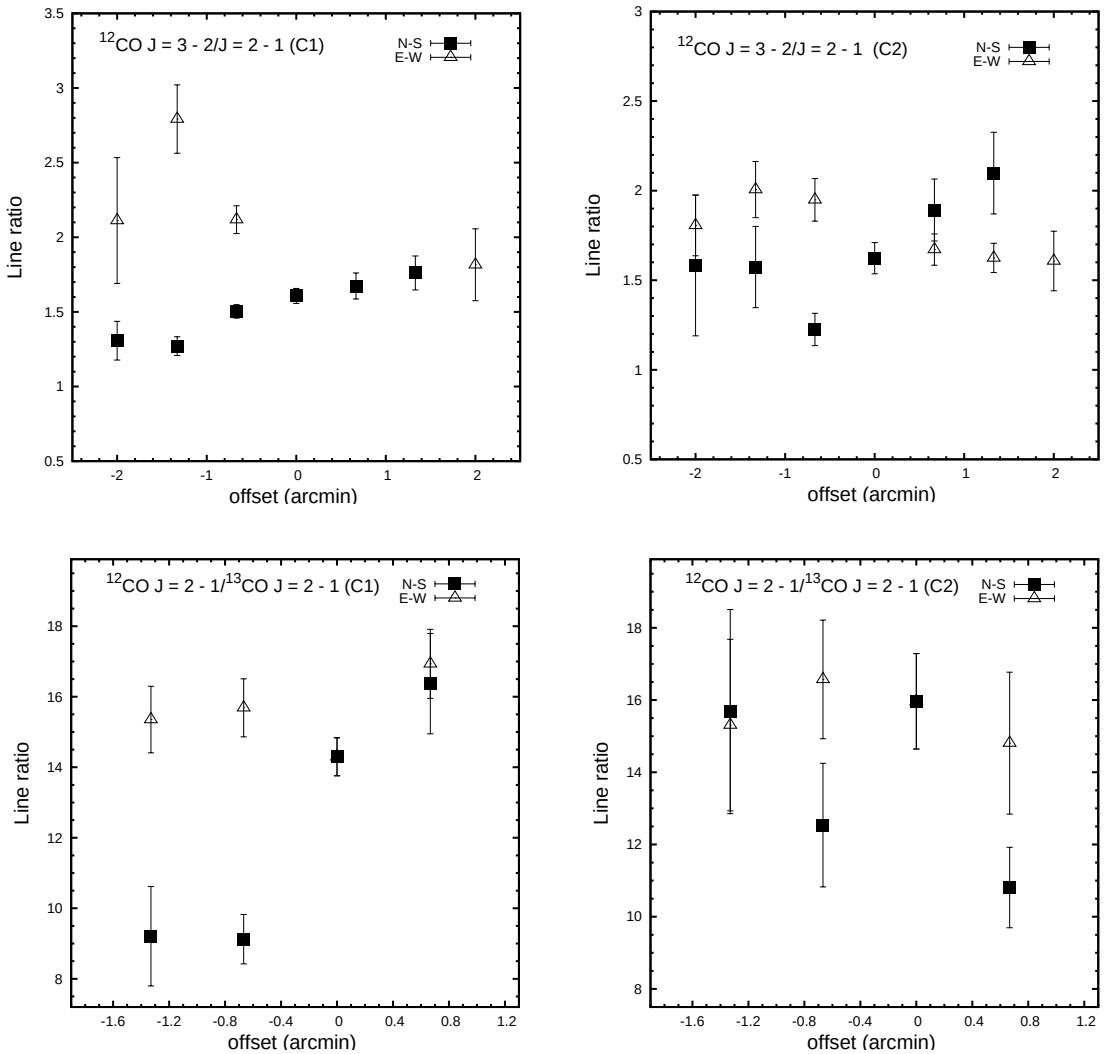

Fig. 3.20: *^{12}CO and ^{13}CO line-integrated intensity ratios along E-W and N-S cuts in IVC210 (line intensity in units of erg cm^{-2} s^{-1} sr^{-1}). The left and right panels correspond to the observed components C#1 and C#2, respectively. The error bars represent the r.m.s. noise of the observations.*

3.4.2 Line Ratios

We calculate line ratios from the observed line-integrated intensities. The advantage of using line ratios is that they are not very sensitive to beam-filling effects when clouds have substructure smaller than the beam. We utilize line-integrated intensity ratios in the escape probability model calculations (Section 3.4.3) and in the PDR modelling of the observations (Section 3.4.4).

Table 3.8 lists the [C I]/^{12}CO and [C I]/^{13}CO line-integrated intensity ratios, averaged over all positions where emission is detected (i.e. emission over the 3σ level). Error

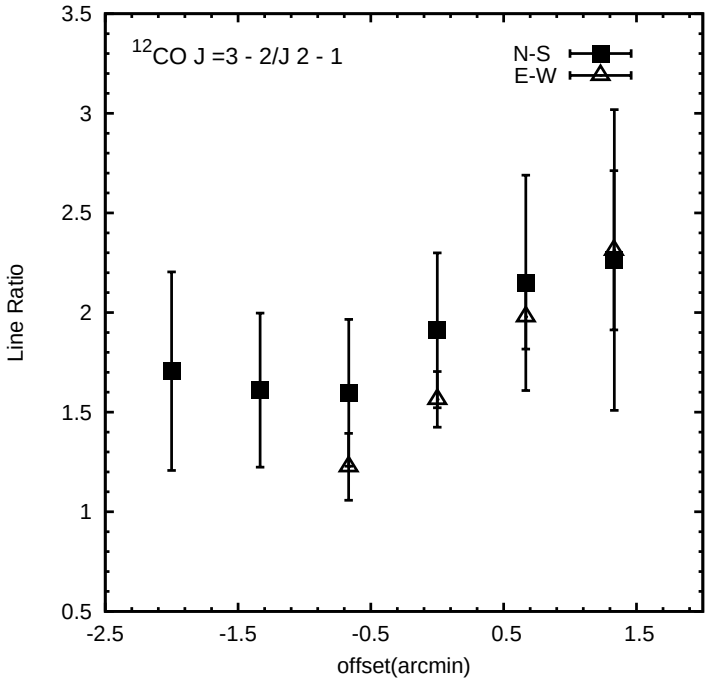

Fig. 3.21: $^{12}CO\ J = 3 \rightarrow 2/J = 2 \rightarrow 1$ *line-integrated intensity ratios along E-W and N-S cuts in IVC140 (line intensity in units of erg* $cm^{-2}\ s^{-1}\ sr^{-1}$*). The error bars represent the r.m.s. noise of the observations.*

bars are calculated from the r.m.s. noise of the observations. The standard deviation of the line-integrated intensity ratios across the map (the line-integrated intensity is in units of erg $cm^{-2}\ s^{-1}\ sr^{-1}$) is also shown. The line ratios are compared with those obtained at the edge of the B5 cloud (Bensch, 2006) and the translucent cloud MCLD 123.5+24.9 (Bensch et al., 2003). As we can see, the observed line ratios are larger compared to those at the edge of the B5 cloud and in MCLD 123.5+24.9.

The [C I]/CO and CO line-integrated intensity ratios as a function of the distance from the central position in both observed components in IVC210 are shown in Figs. 3.19 and 3.20, respectively. The spatial variation of the CO ratios in IVC140 is shown in Fig. 3.21. In all cases, the large error bars do not allow the identification of any specific trend of the line ratios. Nevertheless, rather constant line ratios have been observed in IVC135+54-46 (Heithausen et al., 2001, F. Bensch, private communication). The average values of the CO line-integrated intensity ratios calculated for the complete cloud are listed in Table 3.9.

3.4.3 Excitation Analysis

In the following, we use the ^{12}CO and ^{13}CO data in order to study the excitation conditions of the molecular gas. This provides estimates of physical parameters such

Tab. 3.8: *[C I]/^{12}CO and [C I]/^{13}CO line-integrated intensity ratios.*

Line Ratio	IVC210 C#1	IVC210 C#2	B5 edge	MCLD 123.5+24.9
[C I]/^{12}CO $J = 2 \rightarrow 1$	2.70±0.3(±1.9)[a]	3.44±0.4(±2.7)[a]	1.7±0.3	1.4±0.4
[C I]/^{12}CO $J = 3 \rightarrow 2$	1.27±0.3(±0.4)[a]	1.43±0.5(±0.5)[a]	1.1±0.2	1.06±0.4
[C I]/^{13}CO $J = 2 \rightarrow 1$	26.3±2.9(±5.2)[a]	28.9±1.9(±6.1)[a]	15.4±3.6	10.5±3.9

[a] This value correspond to the standard deviation of the line ratios throughout the cloud.

Tab. 3.9: *^{12}CO and ^{13}CO line-integrated intensity ratios toward IVC210 and IVC140.*

Line Ratio	IVC210 C#1	IVC210 C#2	IVC140
^{12}CO $J = 2 \rightarrow 1/1 \rightarrow 0$[a]	6.3±1.1	5.3±1.0	7.2±2.0
^{12}CO $J = 3 \rightarrow 2/2 \rightarrow 1$[b]	1.4±0.4	1.4±0.8	–
^{12}CO $J = 3 \rightarrow 2/2 \rightarrow 1$[c]	1.8±0.8	1.6±0.4	1.8±0.5
^{12}CO/^{13}CO $J = 1 \rightarrow 0$[a]	10.8±2.9	9.5±2.2	9.2±4.6
^{12}CO/^{13}CO $J = 2 \rightarrow 1$[a]	10.5±4.8	10.1±1.6	–
^{12}CO/^{13}CO $J = 2 \rightarrow 1$[c]	13.6±3.7	14.3±2.2	–

[a] Line ratio at 22″ resolution.
[b] Line ratio at 15″ resolution.
[c] Line ratio at 130″ resolution.

as temperatures, densities, and CO column densities. Our data set is divided into two subsets with different angular resolutions (22″ and 130″). As the extent of the 22″ maps is not sufficient to be convolved to a 130″ resolution, the two data-sets are treated separately.

We first estimate the excitation temperature and the CO column density of the gas using local thermodynamic equilibrium (LTE) assumptions. From the ^{12}CO $J = 1 \rightarrow 0$ and $J = 2 \rightarrow 1$ peak intensity positions observed toward IVC210 and IVC140, we derive lower limits for the excitation temperature. We assume that these transitions are optically thick in the high-resolution data (22″). We find that in both clouds and for both observed transitions the lower limit to the excitation temperature is about $T_{\rm ex} \gtrsim 12$ K.

We estimate the CO column density from the ^{13}CO $J = 1 \rightarrow 0$ line in a 22″ beam using the standard LTE equation for the total ^{13}CO column density given by (Dickman, 1978; Rohlfs & Wilson, 2004),

$$\left(\frac{N^{10}_{^{13}\rm CO}}{\rm cm^{-2}}\right) = 3\times10^{14}\left(\frac{T_{\rm ex}}{\rm K}\right)(1-e^{-(5.3\,\rm K)/T_{\rm ex}})^{-1}\int\tau^{10}(\rm v)\left(\frac{d\rm v}{km\,s^{-1}}\right), \qquad (3.3)$$

where τ^{10} is the optical depth of the ^{13}CO $J = 1 \rightarrow 0$ transition.

For small optical depths ($\tau^{10} < 1$) we can use the approximation,

Tab. 3.10: *Local Thermodynamic Equilibrium (LTE) ratios*[a].

Line Ratio	$T = 6$ K	8 K	9 K	10 K	12 K	14 K	20 K	25 K
^{12}CO $J = 2 \rightarrow 1/1 \rightarrow 0$	5.33	5.94	6.15	6.33	6.60	6.79	7.15	7.3
^{12}CO $J = 3 \rightarrow 2/2 \rightarrow 1$	1.92	2.25	2.37	2.47	2.62	2.73	2.92	3.0

[a] Considering optically thick emission.

$$T_{\rm ex}\int_{-\infty}^{\infty}\tau^{10}({\rm v})d{\rm v} \simeq \frac{\tau_0^{10}}{1-e^{-\tau_0^{10}}}\int_{-\infty}^{\infty}T_{\rm mb}^{10}({\rm v})d{\rm v}, \tag{3.4}$$

to express Equation (3.3) in terms of the ^{13}CO $J = 1 \rightarrow 0$ main-beam brightness temperature ($T_{\rm mb}^{10}$),

$$\left(\frac{N_{^{13}{\rm CO}}^{10}}{{\rm cm}^{-2}}\right) = 3\times10^{14}\frac{\tau_0^{10}}{1-e^{-\tau_0^{10}}}(1-e^{-(5.3{\rm K})/T_{\rm ex}})^{-1}\int_{-\infty}^{\infty}\left(\frac{T_{\rm mb}^{10}}{\rm K}\right)\left(\frac{d{\rm v}}{{\rm km\,s^{-1}}}\right). \tag{3.5}$$

The optical depth of the ^{13}CO $J = 1 \rightarrow 0$ line is obtained from the main-beam brightness temperature using

$$\tau_0^{10} = -ln\left[1-\frac{T_{\rm mb}^{10}}{(5.3\,{\rm K})}\left(\left[e^{(5.3{\rm K})/T_{\rm ex}}\right]^{-1}-0.16\right)^{-1}\right]. \tag{3.6}$$

We also derive the total CO column density using the ^{13}CO $J = 2 \rightarrow 1$ transition at a resolution of 130″. To this end, we use an expression similar to Equation (4.12) which, considering the optical depth effects, is given by

$$\left(\frac{N_{^{13}{\rm CO}}^{21}}{{\rm cm}^{-2}}\right) = 1.5\times10^{14}\frac{\tau_0^{21}}{1-e^{-\tau_0^{21}}}\frac{e^{(5.3{\rm K})/T_{\rm ex}}}{1-e^{-(10.6{\rm K})/T_{\rm ex}}}\int_{-\infty}^{\infty}\left(\frac{T_{\rm mb}^{21}({\rm v})}{\rm K}\right)\left(\frac{d{\rm v}}{{\rm km\,s^{-1}}}\right), \tag{3.7}$$

where the τ_0^{21} and $T_{\rm mb}^{21}$ are the optical depth and main-beam brightness temperature of the ^{13}CO $J = 2 \rightarrow 1$ transition, respectively.

The optical depth of the ^{13}CO $J = 2 \rightarrow 1$ transition is related to $T_{\rm mb}^{21}$ by

$$\tau_0^{21} = -ln\left[1-\frac{T_{\rm mb}^{21}}{(10.6\,{\rm K})}\left(\left[e^{(10.6{\rm K})/T_{\rm ex}}\right]^{-1}-0.02\right)^{-1}\right]. \tag{3.8}$$

For the calculation of the CO column densities we use the derived lower limit of the excitation temperature of $T_{\rm ex} \gtrsim 12$ K and a CO abundance ratio of [^{12}CO]/[^{13}CO] =

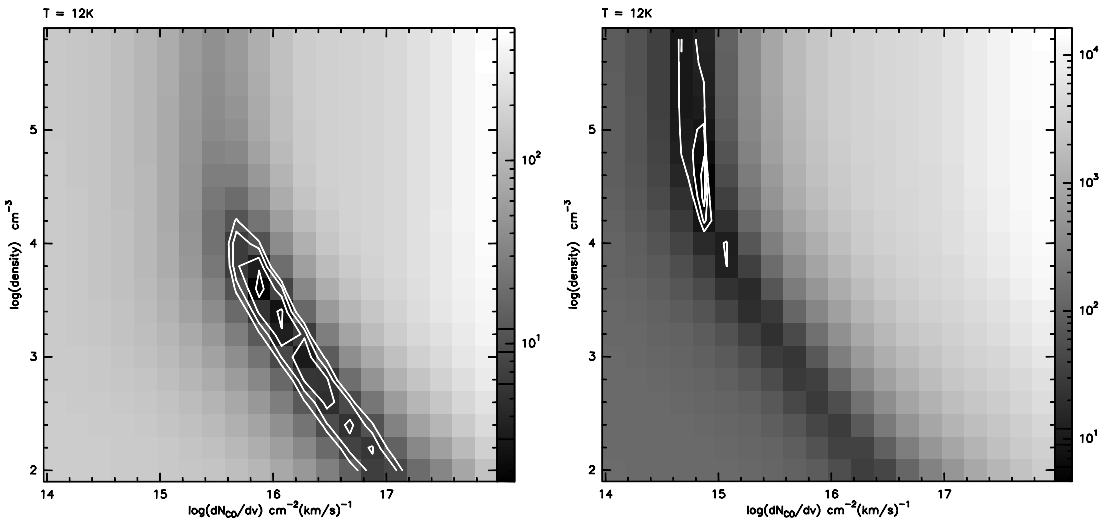

Fig. 3.22: *The Q^2 surface as a function of the gas density and CO column density per interval of velocity for a constant temperature of $T_{\rm kin}$ = 12 K. The panels correspond to the observations at 22″ (left) and at 130″ (right) resolution. In both figures the contours are Q^2 = 3, 6, 9, 12.*

65. Using the 22″ data, we obtain a total CO column density in the intensity peaks in IVC210 and IVC140 of $N_{\rm CO} \gtrsim 1.0 \times 10^{17}$ cm^{-2}. We also analyze regions away from the peak intensity positions in IVC210, resulting in a total CO column density of $N_{\rm CO} \gtrsim 5.2 \times 10^{16}$ cm^{-2}. The CO column density derived in IVC210 based on the ^{13}CO $J = 2 \rightarrow 1$ observation with a 130″ beam is $N_{\rm CO} \gtrsim 2.8 \times 10^{15}$ cm^{-2}. In general the CO column densities tend to be lower compared to those obtained for the high resolution data. This is probably caused by the substructure present on scales smaller than the 130″ beam (0.063 pc at a distance of 100 pc), as more material with a low CO column density is traced.

Table 3.9 lists the ^{12}CO and ^{13}CO line-integrated intensity ratios for IVC210 and IVC140. The ratios correspond to the average calculated over the entire map, and the quoted errors are the standard deviation of the calculated line ratios. Additionally, line ratios calculated assuming LTE and different excitation temperatures $T_{\rm ex}$ are shown in Table 3.10.

The ^{12}CO $J = 2 \rightarrow 1 / J = 1 \rightarrow 0$ line-integrated intensity ratios calculated in IVC210 and IVC140 are consistent with a $T_{\rm ex} \simeq 12$ K gas in LTE. This value of $T_{\rm ex}$ agrees with the lower limit of the excitation temperature derived from the peak intensities of the ^{12}CO $J = 2 \rightarrow 1$ and $J = 1 \rightarrow 0$ transitions. The ^{12}CO $J = 3 \rightarrow 2 / J = 2 \rightarrow 1$ ratio is lower compared to the LTE ratio in both observed clouds. This suggests that the assumptions of LTE and/or optically thick emission are not valid for the ^{12}CO $J = 3 \rightarrow 2$ transition. In the following we study the possible cause of this difference.

In order to constrain the excitation conditions in the observed IVC clouds, we analyze the CO observations using the escape probability code produced by Stutzki & Win-

newisser (1985). This code assumes spherical clouds of uniform density and accounts for non-LTE excitation and effects of finite optical depth. The model calculates the CO line peak temperature in a parameter space defined by the gas temperature, the gas density, and the CO column density per velocity interval $dN_{\rm CO}/d$v. The range of parameters used in our calculations is 8 K $\leq T \leq$ 60 K, $10^{2.0}\,{\rm cm}^{-3} \leq n \leq 10^{6.3}\,{\rm cm}^{-3}$, and $10^{14}\,{\rm cm}^{-2}({\rm km\,s}^{-1})^{-1} \leq dN_{\rm CO}/dv \leq 10^{18}\,{\rm cm}^{-2}({\rm km\,s}^{-1})^{-1}$, corresponding to a grid of $9\times20\times20$ models. The quantity

$$Q^2 = m^{-1}\sum_{i}^{m}(T_{\rm i,obs} - T_{\rm i,mod})^2/\Delta T^2 \tag{3.9}$$

is calculated for each model. Here, $T_{\rm i,obs}$ is the observed peak temperature, $T_{\rm i,mod}$ the model result, and ΔT is the accuracy of the observed peak temperature. They are added over all observed ^{12}CO and ^{13}CO transitions. The defined Q^2 represents a measure of how close the model is to the observations. For example, Q^2 =1 indicates that on average the model matches the observations to within one sigma. Note that Q^2 does not represent a fit to the model results, hence is not to be confused with χ^2. We plot Q^2 as a function of the model parameters, where the minimum Q^2 represents the model with line intensities that are closest to the observations.

We compare the escape probability model with observations toward a number of intensity peaks present in the 22″ and 130″ resolution maps. In IVC210, off-center positions with weaker ^{12}CO emission in both maps are also considered in the analysis. Results of the escape probability analysis are listed in Table 3.11. An example of a Q^2 surface for a constant temperature of 12 K is shown in Fig. 3.22.

Based on the IRAM observations of IVC210 at 22″ resolution, the escape probability model results in typical kinetic temperatures $T_{\rm kin} = 10-16$ K and gas densities below $n = 10^4$ cm^{-3} for components C#1 and C#2. The CO column density per velocity interval is $10^{16}-10^{17}$ cm^{-2} (km s^{-1})$^{-1}$ in component C#1, while in case of component C#2 it is constrained to be larger than $10^{15.5}$ cm^{-2} (km s^{-1})$^{-1}$. The values found in off-center positions are somewhat lower (∼30%) compared to those obtained in the peak positions.

The analysis based on the KOSMA observations of IVC210 at 130″ resolution gives typical kinetic temperatures lower than 14 K for component C#1, while for component C#2 the kinetic temperature could not be well constrained. Gas densities are usually larger than 10^3 cm^{-3} in both components. We obtain better individual constraints for the CO column density per interval of velocity. The overall range $10^{14.5}-10^{16}$ cm^{-2} (km s^{-1})$^{-1}$ for C#1 and $10^{14}-10^{16}$ cm^{-2} (km s^{-1})$^{-1}$ for C#2. Similar to the high-resolution data, we note that the range of CO column densities per velocity interval allows lower values for component C#2 compared to C#1.

The escape probability analysis based on observations of IVC140 at 22″ resolution suggests typical kinetic temperatures of $T_{\rm kin} = 12-16$ K. The range of CO column

Tab. 3.11: *Results of the escape probability model.*

IVC210 Component #1 at 22″ resolution					
Position	Δl^d (″)	Δb^d (″)	$\log(dN_{CO}/dv)$	$\log(n)$	T_{kin}
#1[a]	-10.8	64.8	16.0 – 17.0	<4.0	10.0 – 16.0
#2[a]	43.2	-21.6	>16.0	<3.5	12.0 – 16.0
#3[a]	0	-43.2	>16.0	<3.8	12.0 – 14.0
#4[a]	-54	64.8	14.0 – 15.0	3.0 – 4.0	–[c]
#5[b]	0	32.4	15.5 – 16.5	3.0 – 4.0	10.0 – 16.0
#6[b]	-21.6	0	16.0 – 17.0	3.0 – 4.0	10.0 – 12.0
IVC210 Component #1 at 130″ resolution					
Position	ΔRA^d (″)	ΔDEC^d (″)	$\log(dN_{CO}/dv)$	$\log(n)$	T_{kin}
#1[a]	0	0	15.0 – 16.0	3 – 4.5	8.0 – 14.0
#2[b]	0	80	14.5 – 16.0	>3.8	8.0 – 14.0
#3[b]	0	-80	14.5 – 16.0	>3.5	–[c]
IVC210 Component #2 at 22″ resolution					
Position	Δl^d (″)	Δb^d (″)	$\log(dN_{CO}/dv)$	$\log(n)$	T_{kin}
#1[a]	-43.2	10.8	16.0 – 17.0	<4.0	10.0 – 16.0
#2[a]	-10.8	-21.6	>16.0	<3.5	12.0 – 16.0
#3[a]	43.2	54	>16.0	<3.8	12.0 – 14.0
#4[a]	21.6	-43.2	14.0 – 15.0	3.0 – 4.0	–[c]
#5[b]	32.4	43.2	15.5 – 16.5	3.0 – 4.0	10.0 – 16.0
IVC210 Component #2 at 130″ resolution					
Position	ΔRA^d (″)	ΔDEC^d (″)	$\log(dN_{CO}/dv)$	$\log(n)$	T_{kin}
#1[a]	0	0	14.5 – 16.0	3.5 – 4.5	–[c]
#2[b]	0	-40	14.0 – 16.0	–[c]	–[c]
IVC140 at 22″ resolution					
Position	Δl^d (″)	Δb^d (″)	$\log(dN_{CO}/dv)$	$\log(n)$	T_{kin}
#1[a]	-20	-10	16.0 – 17.0	< 4.5	12.0 – 16.0

[a] This position correspond to a peak of the ^{12}CO emission.
[b] This position correspond to a regions offset from the ^{12}CO emission peaks.
[c] The Q^2 does not show any well defined minimum.
[d] Offset from the map center position.

densities per interval of velocity are similar to that found in IVC210, being in the range $10^{16} - 10^{17.5}$ cm^{-2} (km s^{-1})$^{-1}$. The gas densities are constrained to be lower than $10^{4.5}$cm^{-3}.

The ranges of temperatures found in the escape probability analysis is consistent with the values found for the thermalized ^{12}CO $J = 2 \rightarrow 1$ and $J = 1 \rightarrow 0$ transitions (T_{kin} = 12 K). The ranges obtained for the CO column density are consistent with those derived

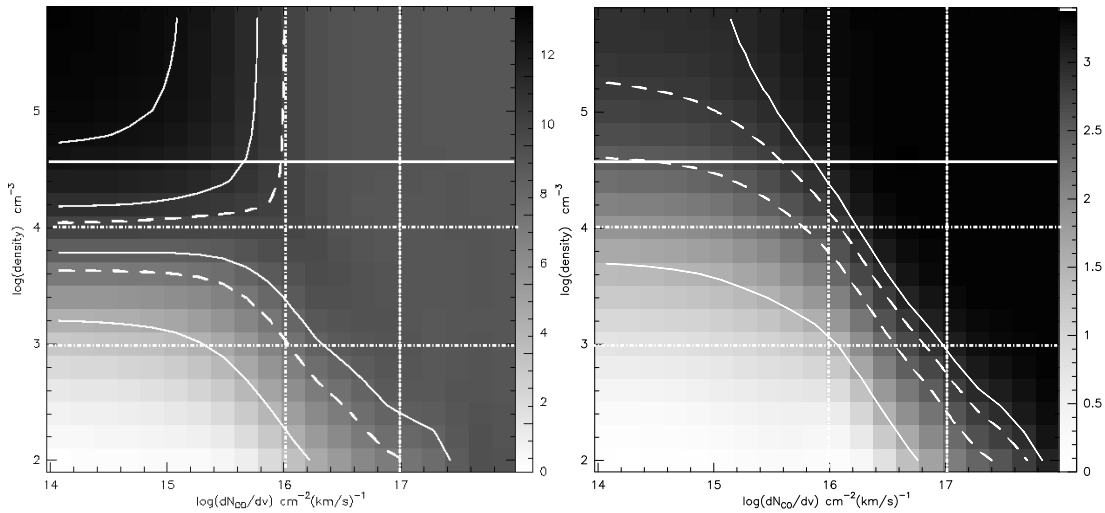

Fig. 3.23: *(a)* ^{12}*CO* $J = 2 \rightarrow 1/J = 1 \rightarrow 0$ *line peak temperature ratio as a function of gas density and CO column density per velocity interval for a 12 K gas. The solid contours correspond to 3, 6, 9, 12, while the dashed contours represent the range of values found with our observations of IVC210. (b)* ^{12}*CO* $J = 3 \rightarrow 2/J = 2 \rightarrow 1$ *line peak temperature ratio as a function of gas density and CO column density per velocity interval for a 12 K gas. The solid contours correspond to 0.7, 2, 2.7, while the dashed contours represent the range of values found with our observations of IVC210. In both panels the limits in gas density and CO column density per velocity interval are depicted by dashed-dotted and solid lines.*

from ^{13}CO under the assumption of LTE, i.e. $\mathrm{d}N_{\mathrm{CO}}/\mathrm{dv} \simeq 10^{16} - 10^{17}$ cm^{-2} (km s^{-1})$^{-1}$ in a 22″ beam and, in case of IVC210, $\mathrm{d}N_{\mathrm{CO}}/\mathrm{dv} \simeq 10^{14} - 10^{16}$ cm^{-2} (km s^{-1})$^{-1}$ in a 130″ beam.

The analysis of the observations at 130″ resolution suggests that the gas density is larger than 10^3 cm^{-3}. The gas density obtained from these observations cannot be larger than the values derived from the observations with a 22″ beam, which is constrained to be lower than 10^4 cm^{-3}. This yields a range for the gas density between $10^3 - 10^4$ cm^{-3}.

Fig. 3.23 shows the ^{12}CO $J = 2 \rightarrow 1/J = 1 \rightarrow 0$ and $J = 3 \rightarrow 2/J = 2 \rightarrow 1$ line-integrated intensity ratios as a function of gas density and CO column density per velocity interval for a 12 K gas. The region with high CO column densities and high gas densities represents the regime where the line temperature ratios are consistent with LTE (Table 3.10). In this region both, the ^{12}CO $J = 2 \rightarrow 1/J = 1 \rightarrow 0$ and $J = 3 \rightarrow 2/J = 2 \rightarrow 1$ line-temperature ratios show a plateau in their distribution. As the gas density decreases to values below the critical density of the involved transitions, the line ratios are still close to LTE at large $dN_{\mathrm{CO}}/d\mathrm{v}$ because of line trapping.

In the regime of low CO column densities, line-temperature ratios in the high density region are dominated by optical depth effects. In case of the ^{12}CO $J = 2 \rightarrow 1/J =$

$1 \rightarrow 0$ line-temperature ratio (Fig. 3.23a), its value increases as the $J = 1 \rightarrow 0$ emission is optically thinner compared to the $J = 2 \rightarrow 1$ transition, making it more sensitive to changes of the CO column density. In contrast, as we can see in Fig. 3.23b, the ^{12}CO $J = 3 \rightarrow 2/J = 2 \rightarrow 1$ line-temperature ratio decreases because the $J = 3 \rightarrow 2$ transition is optically thinner compared to the $J = 2 \rightarrow 1$ transition. As the gas density decreases, the transitions with higher critical densities become sub-thermally excited, thus decreasing both line-temperature ratios.

Considering the range of CO column densities and gas densities obtained in the escape probability analysis, we find that the observed ^{12}CO $J = 3 \rightarrow 2/J = 2 \rightarrow 1$ line-integrated intensity ratio extends into a region of the parameter space where sub-thermal excitation of the ^{12}CO $J = 3 \rightarrow 2$ transition is likely to contribute. The observed ^{12}CO $J = 2 \rightarrow 1/J = 1 \rightarrow 0$ ratios are in a regime consistent with LTE.

The physical parameters estimated in this Section suggest that IVC clouds have temperatures and densities which are similar to those found in translucent clouds. However, the derived CO column densities are lower compared to the typical values found in those clouds.

3.4.4 Photon Dominated Region Modelling

In order to study whether IVCs can be explained by current photochemical models, we study the CO and [C I] emission in IVC210 using the PDR model developed by Störzer et al. (1996). This model assumes a spherical clump isotropically irradiated by an external FUV radiation field. A truncated power-law profile of the form

$$n(r) \propto r^{-1.5} \tag{3.10}$$

for $0.2 \leq r/r_{\rm cl} \leq 1$ and

$$n(r) = const. \tag{3.11}$$

for $r/r_{\rm cl} \leq 0.2$, where $r_{\rm cl}$ is the clump radius, is adopted for the density distribution of the cloud. This density profile corresponds to that of a marginally bound polytropic gas sphere (Chieze, 1987). The external FUV radiation field is measured in units of the mean interstellar FUV radiation field estimated by Draine (1978). The PDR model provides a self-consistent solution of the thermal balance and chemical structure as a function of clump radius. This results in abundances and temperature profiles which are then used by the `ONION` radiative transfer code (Gierens et al., 1992) in order to calculate the peak and line-integrated intensity of the ^{12}CO and ^{13}CO rotational transitions as well as the [C I] and [C II] fine structure transitions. The initial parameters and fractional abundances used in our calculations are summarized in Table 3.12.

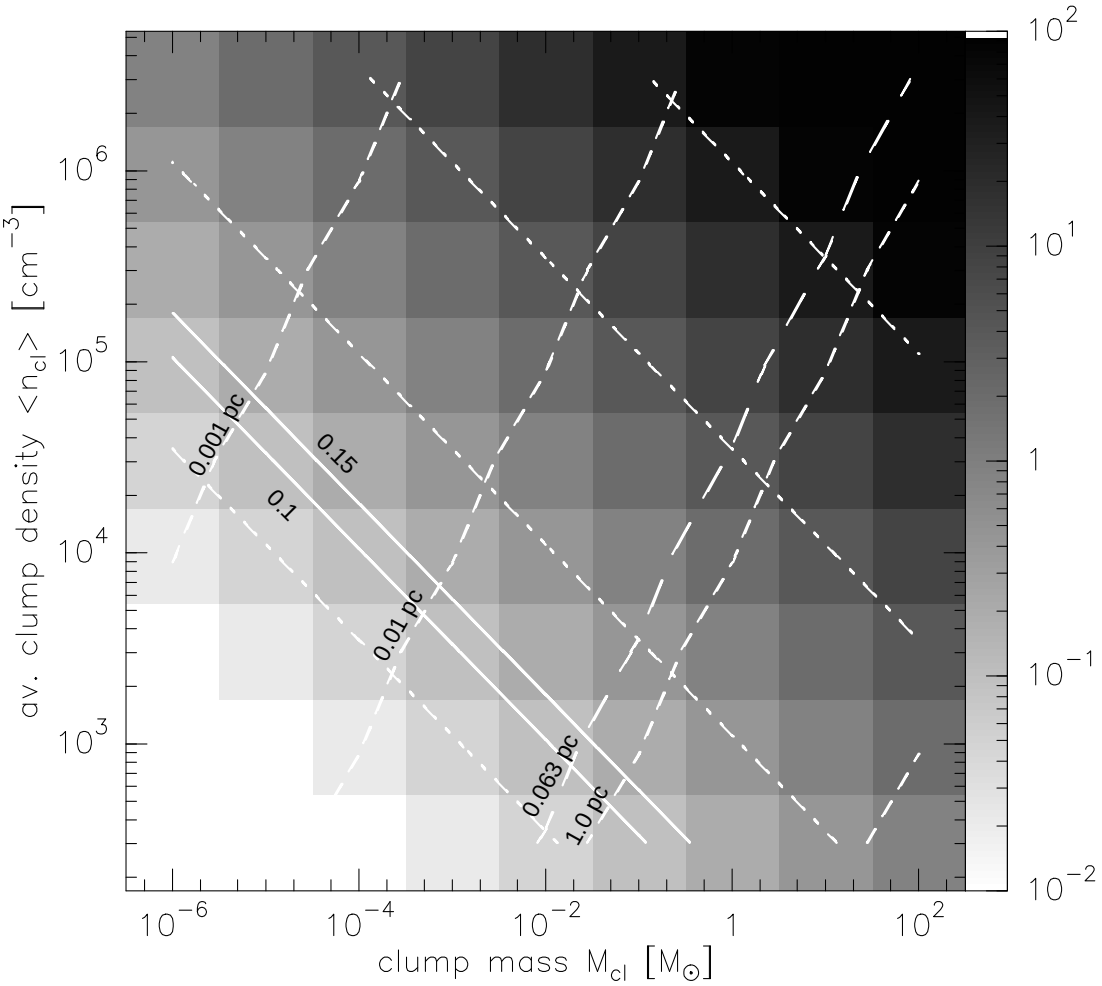

Fig. 3.24: *Clump-averaged visual extinction A_v for the 9×9 models of grid10. The dashed-dotted lines indicate A_v = 0.05, 0.5, 5, and 50. The solid line represent the visual extinction obtained from the extinction map at a resolution of 366″. The dashed lines correspond to the clump radius R_{cl}= 0.001,0.01,0.1, and 1.0 pc. The long-dashed line denote the radius of the 130″ KOSMA-3m beam at distance of 100 pc. The wiggles of the dashed lines result from numerical artifacts.*

The PDR model provides the typical mass and density of the clumps that dominate the observed emission. In the present analysis, we calculate a grid of 9×9 models. The range in mass and density of the clump is given by $3 \times 10^2 \leq \langle n \rangle_{cl} \leq 3 \times 10^6$ cm^{-3} and 10^{-6} M$_\odot \leq M_{cl} \leq 100$ M$_\odot$. The metallicity and strength of the far-ultraviolet radiation field are parameters that are constant for each grid, but are varied in subsequent models in order to study their impact on the emerging line emission.

A cloud-averaged value of the visual extinction of $A_v = 0.32$ is found in the central position of IVC210 using the dust extinction map published by Schlegel et al. (1998), at an angular resolution of 366″. The contribution of H I to the observed visual extinction

Tab. 3.12: *Model parameters of the spherical PDR code.*

Model Parameters		
$M_{\rm cl}$	$10^{-6}\ldots100$ M$_\odot$	Clump mass
$\langle n\rangle_{\rm cl}$	$300\ldots3\times10^6$ cm^{-3}	average clump density
$n_{\rm s}$	$n_{\rm s}\approx0.5\times\langle n\rangle_{\rm cl}$	clump surface density[a]
$\zeta_{\rm CR}$	5×10^{-17}s^{-1}	CR ionization rate
$A_{\rm v}$	$6.3{\times}10^{-22}\times N_{\rm H_{tot}}$	visual extinction
$\tau_{\rm UV}$	$3.68A_{\rm v}$	FUV dust attenuation
b	1 km s^{-1}	Doppler width
He	0.1	abundances[b]
C	1.4×10^{-4}	
O	3.0×10^{-4}	
N	7.9×10^{-5}	
^{13}C	2.15×10^{-6}	
S	2.8×10^{-5}	
Mg	1.1×10^{-6}	
Fe	1.7×10^{-7}	
Si	1.7×10^{-6}	
PAH	4.0×10^{-7}	

[a] For a truncated power-law density profile $n\propto r^{-1.5}$.
[b] Initial abundance, relative to H nuclei.

is estimated using an H I column density of 1×10^{20}cm^{-2} observed with a 10′ beam by Verschuur (1971). This results in a visual extinction of about $A_v = 0.06$ due to the presence of H I gas. Consequently, the contribution of H_2 is $A_v = 0.26$. As we can see, most of the visual extinction is produced by dust associated with H_2. Assuming that the H I column density in the clumps modeled by the PDR model is negligible, we find that H I is mainly present in a diffuse interclump medium. This medium does not have any significant contribution to the emerging line emission and does not significantly attenuate the FUV radiation field ($\lesssim 10$ % for a total line-of-sight visual extinction of $A_v \simeq 0.03$). Note that both of the two components observed in IVC210 contribute to the observed visual extinction. Although the relative contribution is uncertain, we use a relation 60% for C#1 and 40% for C#2, based on the relation between the derived CO column densities (Section 3.4.3).

A PDR model that can explain the observed line-integrated intensity ratios should also be able to account for the observed visual extinction. We consider a cloud composed of an ensemble of dense clumps and assume that the excitation conditions of these clumps are uniform throughout the cloud (Section 3.4.3). Then we can describe this ensemble of clumps by modeling one single "typical" clump (see Section 1.3). We estimate the visual extinction resulting from the model by comparing their line peak temperatures

with the observations convolved to a resolution of 366″. This results in beam-filling factors f for each component. These beam-filling factors can then be applied to the clump-averaged visual extinction of the models in order to obtain the visual extinction at 366″ resolution for each component. The model suggests that in the clumps the column density of H_2 is much larger than that of H I. Therefore, the contribution from H I to the total visual extinction mainly comes from a diffuse H I gas. Consequently, we compare the visual extinction at 366″ resolution estimated from the model with the visual extinction only produced by H_2. We apply this procedure to test if the models which best explain the line-integrated intensity ratios are also able to account for the observed visual extinction.

Fig. 3.24 shows the clump-averaged visual extinction for a 9×9 model grid. The solid lines denote the levels which correspond to the visual extinction obtained from the dust extinction map and distributed in the two components observed toward IVC210. If we consider a clumpy medium composed of dense clumps embedded in a diffuse, low-A_v inter-clump medium, the visual extinction obtained from the observations is the average of the visual extinction of the dense clumps and that of the diffuse medium. Thus, the beam-averaged visual extinction has to be lower compared with the A_v of the individual dense clumps. This sets a limit for the clump-averaged visual extinction suggested by the PDR model. Models with a clump-averaged visual extinction that is lower than the observed value can therefore be discarded.

The radius of the 130″ KOSMA beam at an adopted distance of 100 pc (0.063 pc) is represented by the long-dashed line in Fig. 3.24. If the models that best explain the observations suggest typical clumps that are larger than the projected diameter of the beam they can also be discarded because this contradicts the small-scale structure observed in the 22″ resolution CO maps toward IVC210.

For each grid, we calculate the [C I]/^{12}CO $J = 2 \rightarrow 1$, [C I]/^{12}CO $J = 3 \rightarrow 2$, and [C I]/^{13}CO $J = 2 \rightarrow 1$ line-integrated intensity ratios which are then plotted as a function of $\langle n \rangle_{\rm cl}$ and $M_{\rm cl}$. Fig. 3.25 shows the line-integrated intensity ratios obtained in several model grids. In general, the [C I]/^{12}CO and [C I]/^{13}CO line-integrated intensity ratios increase as the clumps are less dense and less massive. In all considered grids the results apply to both components in IVC210, as the line-integrated intensity ratios observed toward each component are generally explained by similar models. We compare the observations to the model results by calculating a reduced Q^2 using the same procedure described in Section 3.4.3. The quantity Q^2 is plotted as a function of the average clump mass and clump density. It is shown for several grids in Fig. 3.26, and a summary of the obtained results is shown in Table 3.13.

We first run a reference grid (grid10) which considers the mean interstellar FUV radiation field ($\chi = 1.0\,\chi_0$) and solar metallicity ($Z = 1.0\,Z_\odot$). The models that best match the observations suggest that in both components the gas is typically composed of clumps with an average density of $\langle n \rangle_{\rm cl} = 10^{5.48}$ cm^{-3} and masses of $10^{-3} - 10^{-4}$ M$_\odot$. The gas density suggested by the model is inconsistent with the limits of the gas density

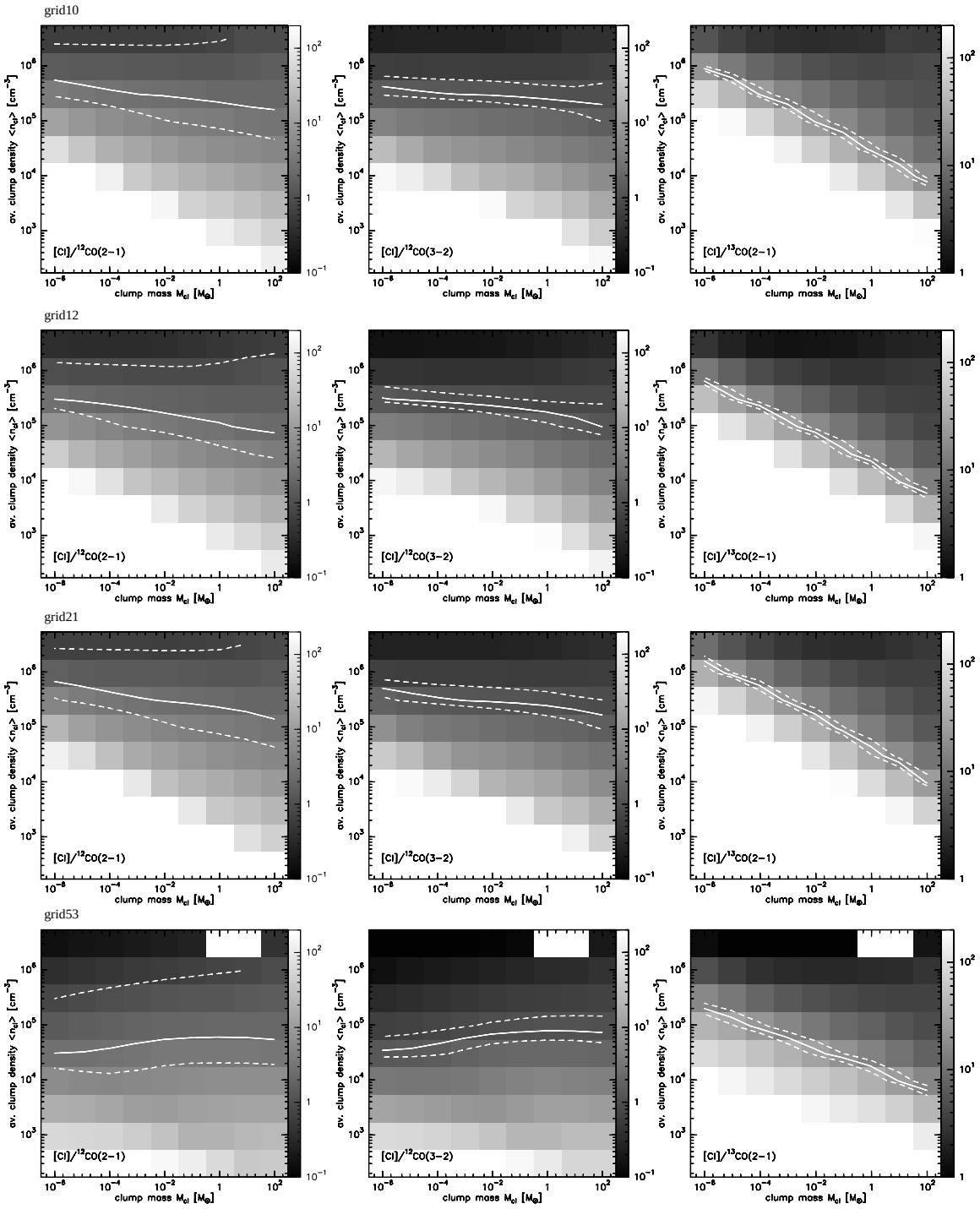

Fig. 3.25: *Model $[C_1]/^{12}CO$ $J = 2 \rightarrow 1$, $J = 3 \rightarrow 2$, and $[C_1]/^{13}CO$ $J = 2 \rightarrow 1$ line-integrated intensity ratios obtained in different model grids. The solid contours represent the observed line-integrated intensity ratios while the dashed ones denote the standard deviation (σ) of the observed line ratios across the map.*

Tab. 3.13: *PDR model-grid results*

Grid	FUV field	$N_{\mathrm{pre,H_2}}$	Metallicity	IVC210 C#1		IVC210 C#2	
#	χ_0	($\mathrm{cm^{-2}}$)	$\mathrm{Z_\odot}$	$\log(\langle n\rangle_{\mathrm{cl}})^a$	M^a_{cl}	$\log(\langle n\rangle_{\mathrm{cl}})^a$	M^a_{cl}
10	1.0	0.0	1.0	5.48	10^{-4}	5.48	10^{-4}
12	0.5	0.0	1.0	5.48	10^{-5}	5.48	10^{-5}
21	1.0	0.0	0.5	5.48	10^{-3}	5.48	10^{-3}
53	1.0	5.0×10^{19}	1.0	4.98	10^{-4}	4.48	10^{-2}

[a] $\langle n\rangle_{\mathrm{cl}}$ and M_{cl} are in units of $\mathrm{cm^{-3}}$ and $\mathrm{M_\odot}$, respectively.

suggested by the escape probability model ($n < 10^{4.0}$ $\mathrm{cm^{-3}}$; Section 3.4.3). The model suggests a clump-averaged visual extinction of $\mathrm{A_v} = 1.16$. Comparing the observed ^{12}CO $J = 2 \rightarrow 1$ line-peak temperature with the corresponding model line-peak temperature, beam-filling factors of $f_1 = 0.17$ for C#1 and $f_2 = 0.105$ for C#2 are obtained at the angular resolution of the $\mathrm{A_v}$ data. This translates into visual extinctions of $\mathrm{A_v} = 0.2$ in C#1 and $\mathrm{A_v} = 0.1$ in C#2, resulting in a total $\mathrm{A_v}$ of 0.3. This is somewhat in excess compared to the observed visual extinction produced by $\mathrm{H_2}$. We therefore discard the reference grid as it is unable to reproduce simultaneously the observed line-integrated intensity ratios and independent constraints of the gas density and visual extinction.

We now consider a PDR model grid with a reduced far-ultraviolet radiation field (grid12). Taking into account that IVCs are likely to be at the interface between the Galaxy halo and the Galactic disc, they are mainly illuminated from only one side by the mean interstellar FUV radiation field. Therefore, the strength of the FUV radiation field is probably reduced in IVC clouds. We study the effect of reducing the strength of the FUV radiation field considering a grid with $\chi = 0.5\chi_0$. The model grids suggest a range of clump masses $M_{\mathrm{cl}} = 10^{-4} - 10^{-5}$ $\mathrm{M_\odot}$ and clump-averaged densities of $\langle n\rangle_{\mathrm{cl}} = 10^{5.0} - 10^{5.5}$ $\mathrm{cm^{-3}}$. The suggested densities are still in excess compared with the upper limit derived in the escape probability modelling.

We run a PDR model grid with reduced metallicity (grid21). Absorption line observations have suggested that IVCs have metallicities ranging between 50% to 100% solar (Wakker, 2001). In the following we consider models with a metallicity of $Z = 0.5\,Z_\odot$. The range of clump masses suggested by the model is between $M_{\mathrm{cl}} = 10^{-3} - 10^{-2}$ $\mathrm{M_\odot}$, while the clump-averaged density is about $\langle n\rangle_{\mathrm{cl}} = 10^{5.0} - 10^{5.5}$ $\mathrm{cm^{-3}}$. Similar to the results from grid10 and grid12, the gas densities are still incompatible with our previous results.

We finally consider grids in which the spherical clumps are surrounded by a halo with a small column density of $\mathrm{H_2}$, but have very low visual extinction (grid53). This pre-shielding is motivated by previous studies, which suggest that a small amount of molecular hydrogen in a diffuse interclump medium can explain the observed [CI]/^{12}CO and [CI]/^{13}CO line-integrated intensity ratios in translucent clouds (Bensch et al., 2003; Bensch, 2006). The presence of pre-shielding is further supported by studies

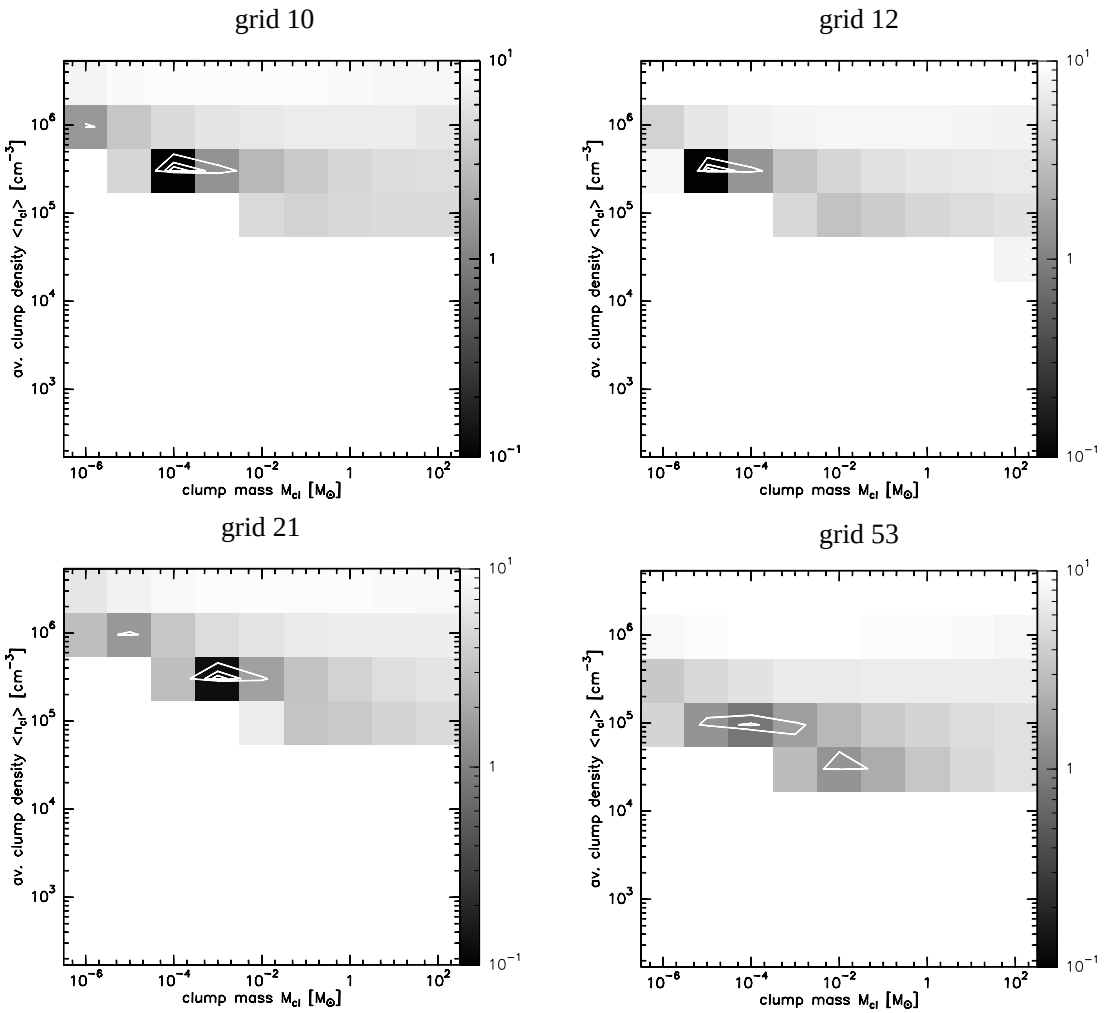

Fig. 3.26: *Reduced Q^2 resulting from the comparison between the observed [C I]/^{12}CO and [C I]/^{13}CO line-integrated intensity ratios toward IVC210 C#1 and several model grids. The contours represent Q^2 =0.5, 1, and 2.*

of H_2 absorption, which have revealed the existence of a ubiquitous, diffuse molecular hydrogen component in IVCs (Richter et al., 2003).

We assume that at least half of the observed H_2 column density is distributed in clumps, while less than half is contained in the diffuse inter-clump medium. Considering that the clumps are uniformly surrounded by a diffuse gas, half of the H_2 column density distributed in it is located as a foreground between the clump and the observer. We therefore use a pre-shielding column density that corresponds to the 25% of the total H_2 column density estimated from the observed visual extinction ($N_{\mathrm{pre,H_2}} = 5 \times 10^{19}$ cm^{-2}). We consider this value to be an upper limit of the pre-shielding column density.

The model grids suggest a range of clump masses of $M_{\mathrm{cl}} = 10^{-5} - 10^{-1}$ M$_\odot$. The range of clump averaged densities is $\langle n \rangle_{\mathrm{cl}} = 10^{4.5} - 10^{5.0}$ cm^{-3}, which is consistent

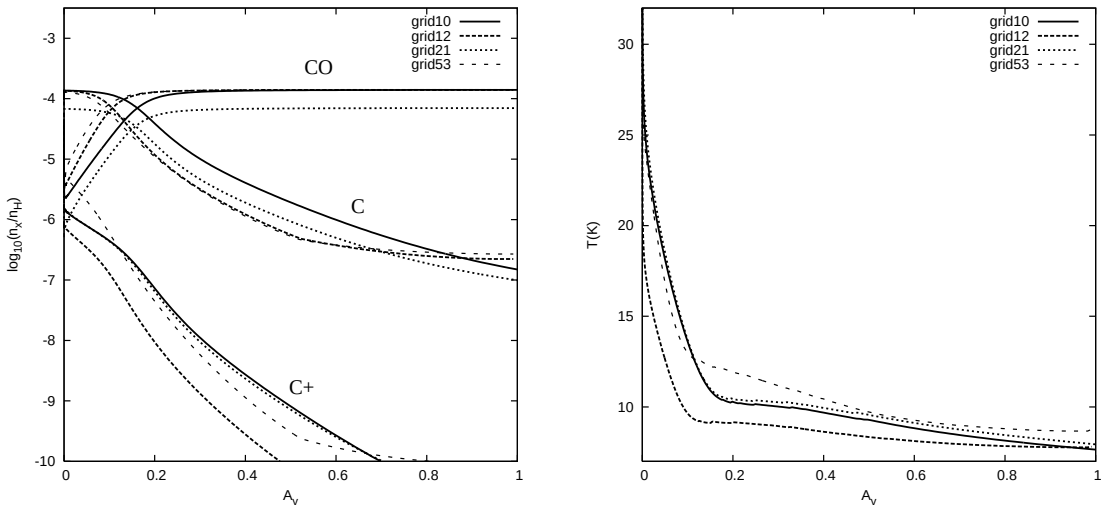

Fig. 3.27: *Abundances of C^+, C^0, and CO (left) and gas temperature (right) as a function of visual extinction for each considered model grid. The abundance and temperature profiles correspond to the model with the lowest Q^2 in each PDR model grid.*

with the values obtained in the escape probability analysis (Section 3.4.3). The visual extinction calculated from the model ($A_V = 0.22$) is also consistent with the observed value.

Fig. 3.27 shows the abundances of C^+, C^0, and CO and the gas temperature as a function of the visual extinction for grid10, grid12, grid21, and grid53.

In grid12, the reduced strength of the far-ultraviolet radiation field lowers the gas temperature near the surface of the cloud. The C^0/CO transition layer is shifted to the cloud surface, reducing the C^0 column density. The reduced flux of far-ultraviolet photons decreases the rate of C^0 ionization and therefore decreases the abundance of C^+. The lower gas temperature and reduced C^0 column density reduces the [C I] line emission, while the increased CO column density makes the CO emission stronger. This reduces the value of the [C I]/^{12}CO and [C I]/^{13}CO line-integrated intensity ratios.

In grid21, the reduced metallicity of the gas decreases the C^0 and CO abundances, while the abundance of C^+ remains unaltered. The temperature profile does not any show significant changes compared to grid10. The lower abundance of C^0 and CO reduce the model intensities of both species. However, the relative intensity between [C I] and CO is not significantly affected by the reduction of the metallicity. Therefore the model [C I]/^{12}CO and [C I]/^{13}CO line-integrated intensity ratios are not sensitive to the metallicity.

In grid53, the presence of a pre-shielding column density shifts the C^0/CO transition layer to the cloud surface. The increase of the CO abundance near the cloud center coincides with an increase of the gas temperature between $A_V \simeq 0.15 - 0.5$, increasing

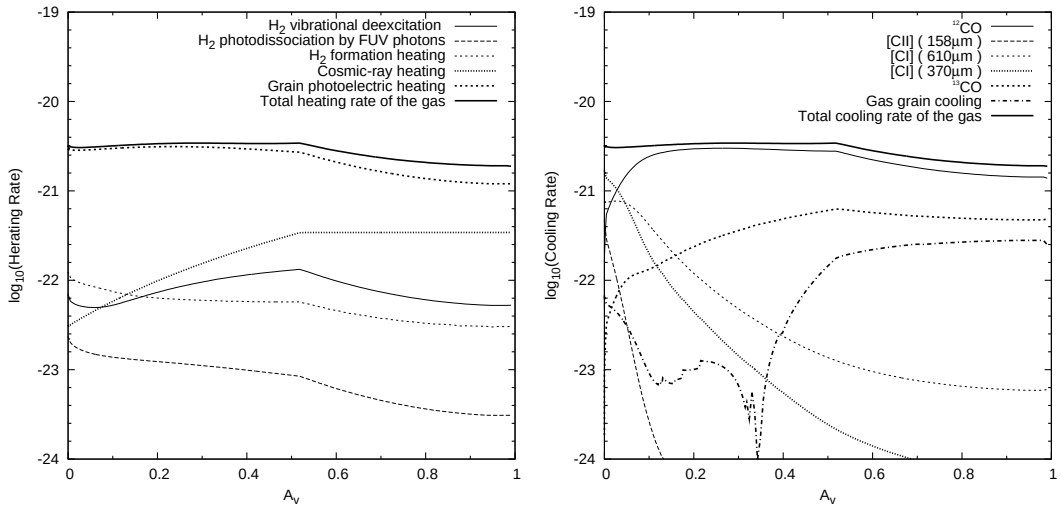

Fig. 3.28: *Heating and cooling rates as a function of visual extinction for the dominant mechanisms. The rates correspond to the model that best matches the observed line-integrated intensity ratios in grid53.*

the intensity of the CO transitions. Near the surface of the cloud, the abundance of C^0 relative to C^+ is reduced, making the [C I] intensity weaker. Thus, the model [C I]/^{12}CO and [C I]/^{13}CO line-integrated intensity ratios are reduced.

3.5 Discussion

The analysis of the observations presented in this chapter suggests that the observed intermediate-velocity clouds (IVC210 and IVC140) have a low molecular mass (0.045 and 0.023 $M_\odot$, respectively), low excitation temperatures ($T_{\rm ex} \simeq 12$ K) and low CO column densities ($N_{\rm CO} \simeq 10^{16} - 10^{17}$ cm^{-2}). The gas density in IVC210 is between $n = 10^3 - 10^4$ cm^{-3}. In case of IVC140, we find an upper limit for the gas density of $10^{4.5}$ cm^{-3}. This suggests that IVCs are similar to translucent clouds in the regime of low CO column densities.

In the PDR analysis of IVC210 we have found that the inclusion of a halo with a low column density of molecular hydrogen surrounding the dense clumps can simultaneously explain the observed [C I]/^{12}CO and [C I]/^{13}CO line-integrated intensity ratios and the independent constraints of the gas density and visual extinction. The principal effect of the inclusion of pre-shielding is that CO is more efficiently shielded by H_2 due to their similar dissociation energies, hence the abundance of CO increases near the surface of the cloud, while the C^0 abundance is decreased. This reduces the [C I]/^{12}CO and [C I]/^{13}CO line-integrated intensity ratios of the model.

Reducing the metallicity of the gas in our PDR models by 50% has no significant im-

pact on the [C I]/^{12}CO and [C I]/^{13}CO line-integrated intensity ratios. The reason is that the line emission of both species is reduced approximately by the same amount so that their relative emission is unaltered. However, the abundance of C^+ relative to C^0 and CO shows larger differences compared to a model with solar metallicity. Observations of the [C II] $^2P_{3/2}\rightarrow{}^2P_{1/2}$ fine structure transition will be helpful to assess the impact of a low metallicity on the emerging line emission from PDR models exposed to weak far-ultraviolet radiation fields.

Fig. 3.28 shows heating and cooling rates for different processes as a function of visual extinction A_v for the PDR model with the smallest Q^2, on the grid that includes pre-shielding (grid53). The photoelectric effect on dust grains dominates the gas heating at the cloud surface followed by cosmic-ray heating which becomes more important at larger depths. The gas cooling is mainly governed by the ^{12}CO rotational transitions except in a thin layer ($A_v < 0.05$) where the [C I] fine structure transitions dominates. Note that the [C II] transition does not dominate the cooling, even very close to the cloud surface. This is attributed to the presence of PAHs in the chemical network of our models, which enhance the charge transfer between PAH^- and C^+, hence reducing the abundance of C^+ (see Chapter 2).

In the PDR model with the smallest Q^2 in grid53, the ^{12}CO rotational transitions dominate the global line emission over the projected cross-section of the clump, with a total intensity of 1.4×10^{-6} erg s^{-1} cm^{-2} sr^{-1}, followed by the [C I] fine structure transitions with a total intensity of 8.9×10^{-7} erg s^{-1} cm^{-2} sr^{-1}. The [C II] $^2P_{3/2}\rightarrow{}^2P_{1/2}$ fine structure transition contributes with a total intensity of only 6.5×10^{-8} erg s^{-1} cm^{-2} sr^{-1}.

Additional observations can be used to test our model of IVC210. Table 3.14 lists the peak temperature predicted by the models that best explain the observation in each considered grid. Based on the observations of IVC210 at 22″ resolution, we expect that the beam filling is close to unity. Thus, we can use the listed values as predictions for future observations as long as they are observed at a similar or higher resolution. In general, the model with a reduced far-ultraviolet radiation field predicts reduced line peak temperatures in all listed transitions as compared to the reference model. The peak temperature of the [C II] $^2P_{3/2}\rightarrow{}^2P_{1/2}$ fine structure transition is especially sensitive to this parameter, being reduced by a factor of 10. The model with reduced metallicity has no significant differences in the predicted line peak temperature compared to the reference model, except for the [C II] $^2P_{3/2}\rightarrow{}^2P_{1/2}$ fine structure transition which is enhanced by a factor of 2. Finally, the models with pre-shielding have enhanced [C II] and low$-J$ ^{12}CO line peak temperatures, while they are reduced in case of the [C I] and ^{13}CO transitions. Line peak temperatures in the high$-J$ ^{12}CO transitions are more similar to those in the reference model.

Tab. 3.14: *PDR model predictions of the peak temperature (in K) of several transitions.*

Transition	grid10 $\log(\langle \frac{n}{\mathrm{cm}^{-3}} \rangle_{\mathrm{cl}}) = 5.2$ $M_{\mathrm{cl}} = 10^{-3}\ \mathrm{M}_{\odot}$	grid12 $\log(\langle \frac{n}{\mathrm{cm}^{-3}} \rangle_{\mathrm{cl}}) = 5.2$ $M_{\mathrm{cl}} = 10^{-5}\ \mathrm{M}_{\odot}$	grid21 $\log(\langle \frac{n}{\mathrm{cm}^{-3}} \rangle_{\mathrm{cl}}) = 4.7$ $M_{\mathrm{cl}} = 10^{-3}\ \mathrm{M}_{\odot}$	grid53 $\log(\langle \frac{n}{\mathrm{cm}^{-3}} \rangle_{\mathrm{cl}}) = 4.7$ $M_{\mathrm{cl}} = 10^{-4}\ \mathrm{M}_{\odot}$
[C II] $^2P_{3/2} \rightarrow {}^2P_{3/2}$	0.21×10^{-2}	0.02×10^{-2}	0.49×10^{-2}	0.47×10^{-2}
[C I] $^3P_1 \rightarrow {}^3P_0$	2.62	1.39	2.67	1.65
[C I] $^3P_2 \rightarrow {}^3P_1$	0.72	0.22	0.77	0.46
$^{12}CO J = 1 \rightarrow 0$	5.67	4.14	5.91	6.49
$^{12}CO J = 2 \rightarrow 1$	5.69	4.05	5.83	6.45
$^{12}CO J = 3 \rightarrow 2$	4.02	2.52	4.14	4.17
$^{12}CO J = 4 \rightarrow 3$	1.94	0.95	2.06	1.79
$^{12}CO J = 5 \rightarrow 4$	0.43	0.12	0.49	0.36
$^{12}CO J = 6 \rightarrow 5$	0.03	0.006	0.03	0.02
$^{13}CO J = 1 \rightarrow 0$	1.16	0.56	1.27	0.68
$^{13}CO J = 2 \rightarrow 1$	1.14	0.54	1.26	0.79
$^{13}CO J = 3 \rightarrow 2$	0.55	0.23	0.62	0.42
$^{13}CO J = 4 \rightarrow 3$	0.12	0.04	0.14	0.10
$^{13}CO J = 5 \rightarrow 4$	0.01	0.004	0.01	0.01

3.6 Summary and Conclusions

In this chapter we have studied the nature of two intermediate velocity clouds (IVC210 and IVC140) using the rotational transitions of ^{12}CO and ^{13}CO as well as the fine structure transition of [C I]. From the analysis of these observations we conclude:

- The global parameters obtained deduced from the CO observations with a 130″ beam suggest that the observed intermediate velocity clouds have molecular masses of (4.5 ± 0.8) $\times 10^{-3}$ and (2.2 ± 0.3) $\times 10^{-3}$ $M_\odot$ and subtend areas of 0.054 and 0.078 pc^2 for IVC210 and IVC140, respectively.
- The excitation analysis of the ^{12}CO and ^{13}CO observations toward IVC210 and IVC140 suggest an excitation temperature $T_{ex} \simeq 12$ K and total CO column densities $N_{CO} \simeq 10^{16} - 10^{17}$ cm^{-2} in a 22″ beam. The gas density in IVC210 is in the range $n = 10^3 - 10^4$ cm^{-3}, while in IVC140 we have found an upper limit of $n < 10^{4.5}$ cm^{-3}. The ^{12}CO $J = 2 \rightarrow 1$ and ^{12}CO $J = 1 \rightarrow 0$ transitions are consistent with LTE, while the ^{12}CO $J = 3 \rightarrow 2$ transition is probably affected by subthermal excitation or optical depth effects.
- The results of the PDR model analysis suggest that a spherical clump surrounded by a layer of diffuse gas with a small column density of H_2 (5×10^{19} cm^{-2}) can simultaneously explain the observed [C I]/^{12}CO and [C I]/^{13}CO line-integrated intensity ratios and the independent constraints of the gas density and visual extinction. Models with reduced metallicity do not show any significant change of the model line-integrated intensity ratios.

Our study suggests that the physical conditions in IVC clouds are similar to those in translucent clouds although they have lower CO column densities. The molecular gas represent only a small portion of the H I cloud, suggesting that IVCs may be an early stage in the formation of translucent clouds.

4 Molecular Gas in the Vicinity of the 30 Doradus Region in the LMC

Parts of this chapter have been submitted for publication in Astrophysical Journal (Pineda, J.L, Ott,J., Klein, U., Wong,T., Muller, E. and Hughes, A., 2007).

4.1 Introduction

The study of the interstellar medium (ISM) in dwarf galaxies provides important insights into the star formation history of the Universe. In massive spiral galaxies the progenitor molecular gas and the young stellar component are generally detached, due to the influence of shear forces (differential rotation), making the study of the relation between them difficult. Dwarf galaxies, in general, show little evidence of shear so that we can study the relation between star formation and its prerequisites at their very locations. They may also be considered as local templates of the earliest galaxies. They are thought to be survivors of the merging processes that lead to the formation of larger galaxies, such as the Milky Way. Thus, the detailed study of the low-metallicity molecular gas in dwarf galaxies may help to understand the physical conditions under which star formation takes place in the main population of galaxies in the early Universe. This understanding is crucial in order to interpret observations of the ISM in galaxies at high redshift.

It is in this context that the Large Magellanic Cloud (LMC) is an ideal extragalactic laboratory to study the details of star formation and feedback. Its proximity (∼50 kpc; Feast 1999, a value which we will use throughout the paper) and nearly face-on orientation allows us to study individual clouds at high spatial resolution, while its strongly varying far-ultraviolet radiation fields provide the opportunity to study very different physical conditions in a low-metallicity environment (30 – 50% solar; Westerlund 1997).

4.2 The Molecular Ridge Near 30 Dor in the Large Magellanic Cloud

The most prominent feature in the LMC is the 30 Doradus (hereafter 30 Dor) H II complex, the most massive star forming region in the Local Group. The young stellar cluster R 136 in the center of 30 Dor produces an extreme far-ultraviolet (FUV) radiation field. Previous surveys of molecular gas in the LMC (e.g. Cohen et al., 1988; Fukui et al., 1999) revealed a huge and prominent complex of molecular clouds extending south from 30 Dor for nearly 2 kpc. This molecular structure is outstanding, as it marks what may be a region of propagating star formation. Parts of the 30 Dor

molecular ridge has been previously observed at high angular resolution with the SEST telescope (Johansson, 1991; Israel et al., 1993; Booth, 1993; Johansson et al., 1994; Kutner et al., 1997; Johansson et al., 1998). In Fig. 4.29 we show the ^{12}CO(1−0) map of the south-eastern part of the LMC obtained with the NANTEN telescope (Fukui et al., 1999). The entire LMC observed in H I is shown in Fig. 4.30.

The origin of the 30 Dor ridge might be connected with ram pressure, exerted onto the ISM as a result of the motion of the LMC through the gaseous halo of the Milky Way (e.g. Mastropietro et al., 2005). de Boer et al. (1998) found evidence for an age structure of the stellar population along the north-eastern through north-western periphery of the LMC, which they attribute to the motion and (clock-wise) rotation of the LMC. In this scenario, an enhanced formation of molecular clouds and, subsequently, of stars is triggered by the ram pressure that the leading edge of the LMC is prone to. It is therefore near at hand to conjecture that the eastern edge of the LMC is a region with enhanced formation of molecular clouds, going along with large-scale shocks. Alternatively, this structure can also be produced by tidal interaction between the Large Magellanic Cloud (LMC), the Small Magellanic Cloud (SMC), and the Milky Way (e.g. Bekki & Chiba, 2005).

In this Chapter, we present a complete ^{12}CO $J = 1 \rightarrow 0$ map of the 30 Dor molecular ridge in the Large Magellanic Cloud obtained with the ATNF Mopra 22-m telescope at high angular and velocity resolution. The observations are summarized in Sect. 4.3. The analysis of the data is described in Sect. 4.4 and the results are discussed in Sect. 4.5. A summary is given in Sect. 4.6.

4.3 Observations

The ^{12}CO $J = 1 \rightarrow 0$ (115 GHz) observations were made using the 22-m ATNF Mopra[4] telescope between June and September 2005. The ^{12}CO $J = 1 \rightarrow 0$ map of the 30 Dor molecular ridge is shown in Fig. 4.31.

A total of 140 fields, 5′×5′ in size, were mapped using the on-the-fly mapping mode, encompassing the whole molecular ridge. Typical values of the single side-band (SSB) system temperature $T^*_{\rm sys}$ of about 600 K were obtained under clear atmospheric conditions. Prior to each map, the pointing accuracy was checked using the SiO maser R Dor, with corrections typically below 5″.

The digital correlator was configured to output 1024 channels across a 64 MHz band in two polarizations, corresponding to a velocity resolution of 0.16 km s^{-1}. We used the AIPS++ tasks *LiveData* and *Gridzilla* to calibrate the spectra and to subtract straight lines from them. The data was then gridded onto data cubes.

[4]The Mopra radio telescope is part of the Australia Telescope which is funded by the Commonwealth of Australia for operation as a National Facility managed by CSIRO.

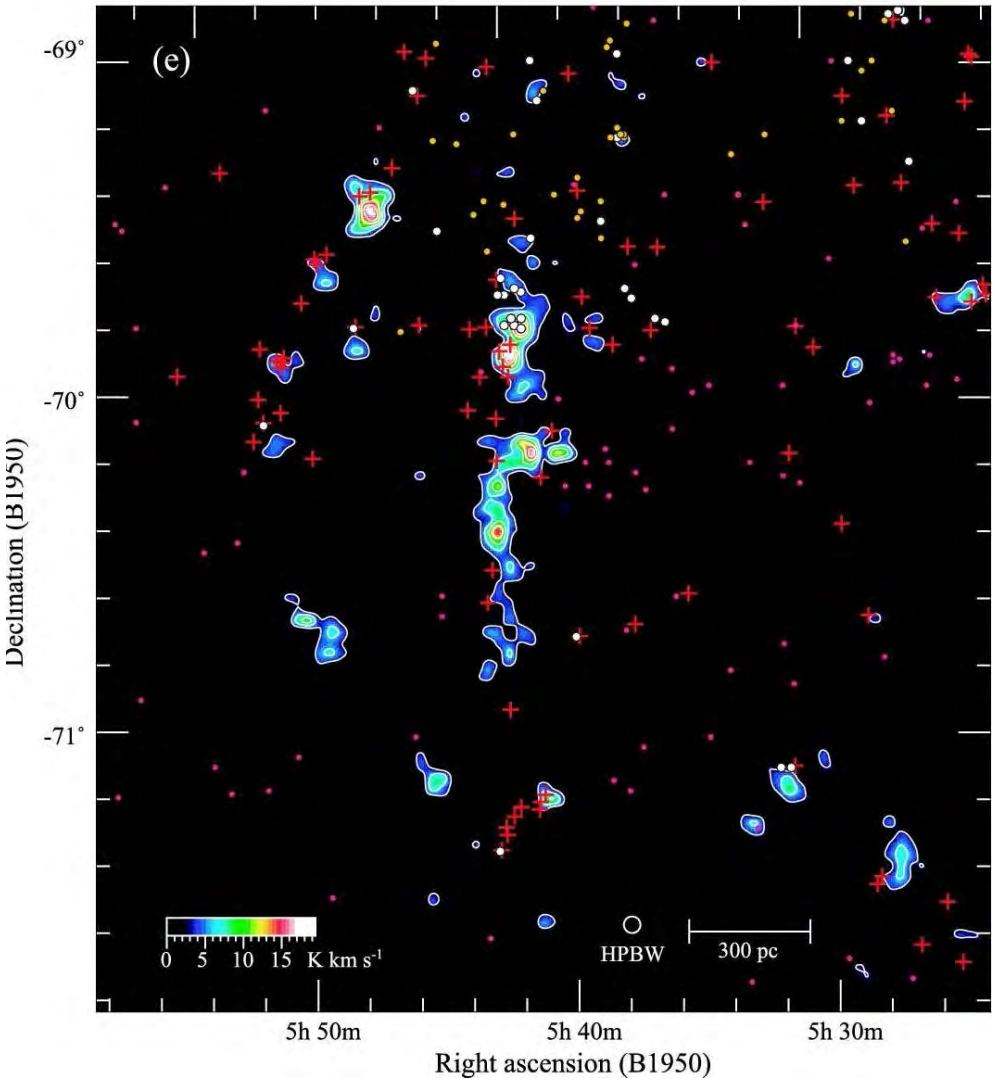

Fig. 4.29: *South-eastern section of the LMC mapped with the NANTEN telescope (Fukui et al., 1999). The most salient features are the molecular ridge south of 30 Doradus and the chain of clouds arranged in a "molecular-arc".*

During the gridding procedure, the data were conlvolved with a Gaussian smoothing kernel with a FWHM half of the beam-size (33″ at 115 GHz), producing an effective resolution of 40″ for the data cube. The spectra were smoothed to an angular resolution of 45″ (corresponding to a linear scale of 11 pc) and to a velocity resolution of 0.48 km s^{-1}, in order to increase the signal-to-noise ratio. They were scaled to main-beam brightness temperature (T_{mb}) using a main-beam efficiency η_{mb} = 0.42 (Ladd et al., 2005).

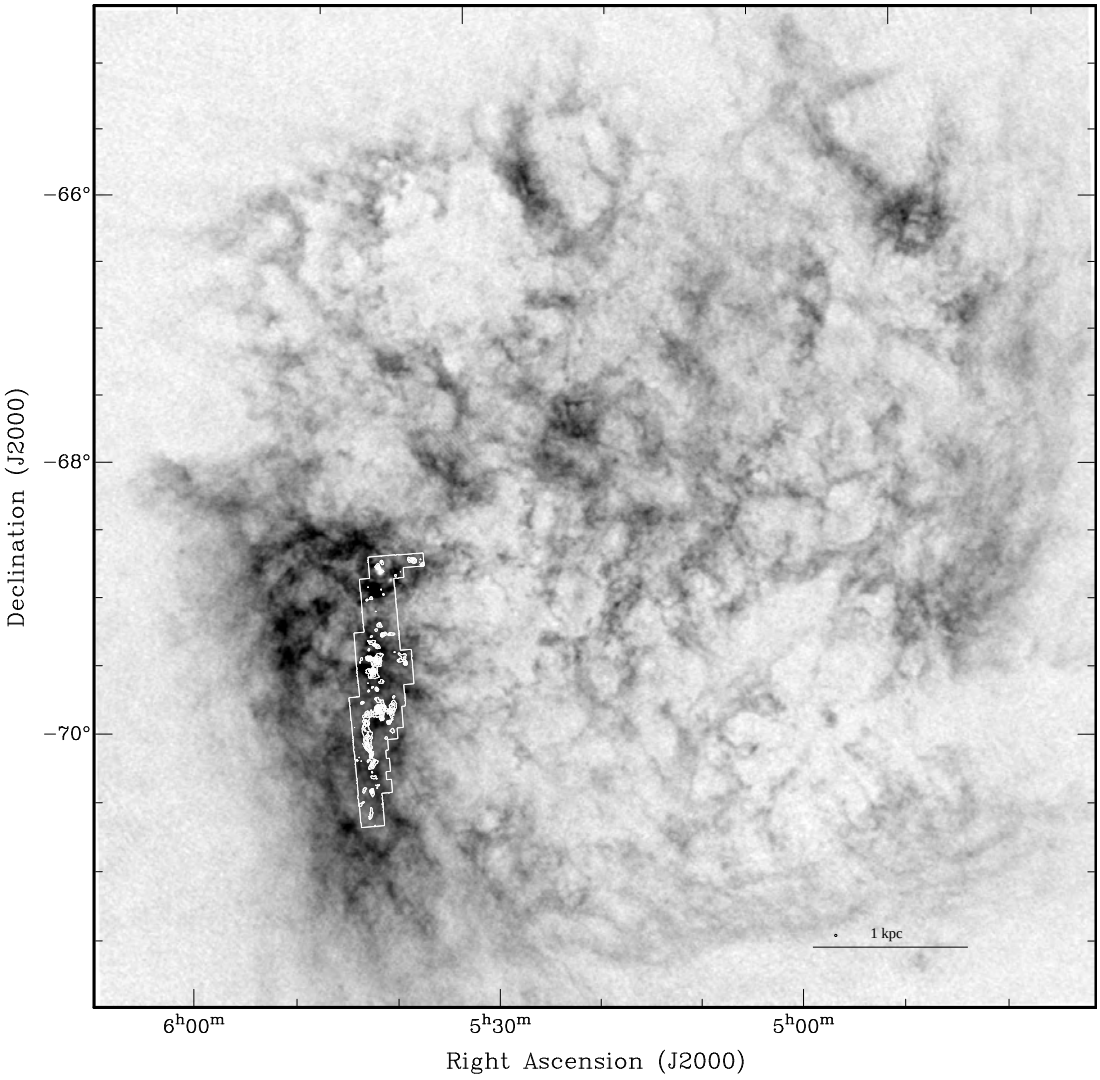

Fig. 4.30: *The entire LMC observed in the H*I *21 cm line (Kim et al., 1998), overlaid with the* ^{12}*CO(1–0) integrated intensity Mopra map.*

4.4 Analysis and Results

4.4.1 Variations in the Far-ultraviolet Radiation Field

Fig. 4.32 shows the 30 Dor molecular ridge in the 8.6 GHz radio continuum (Dickel et al., 2005) and in Hα (SHASSA, Gaustad et al., 2001). The ^{12} CO $J = 1 \rightarrow 0$ map is

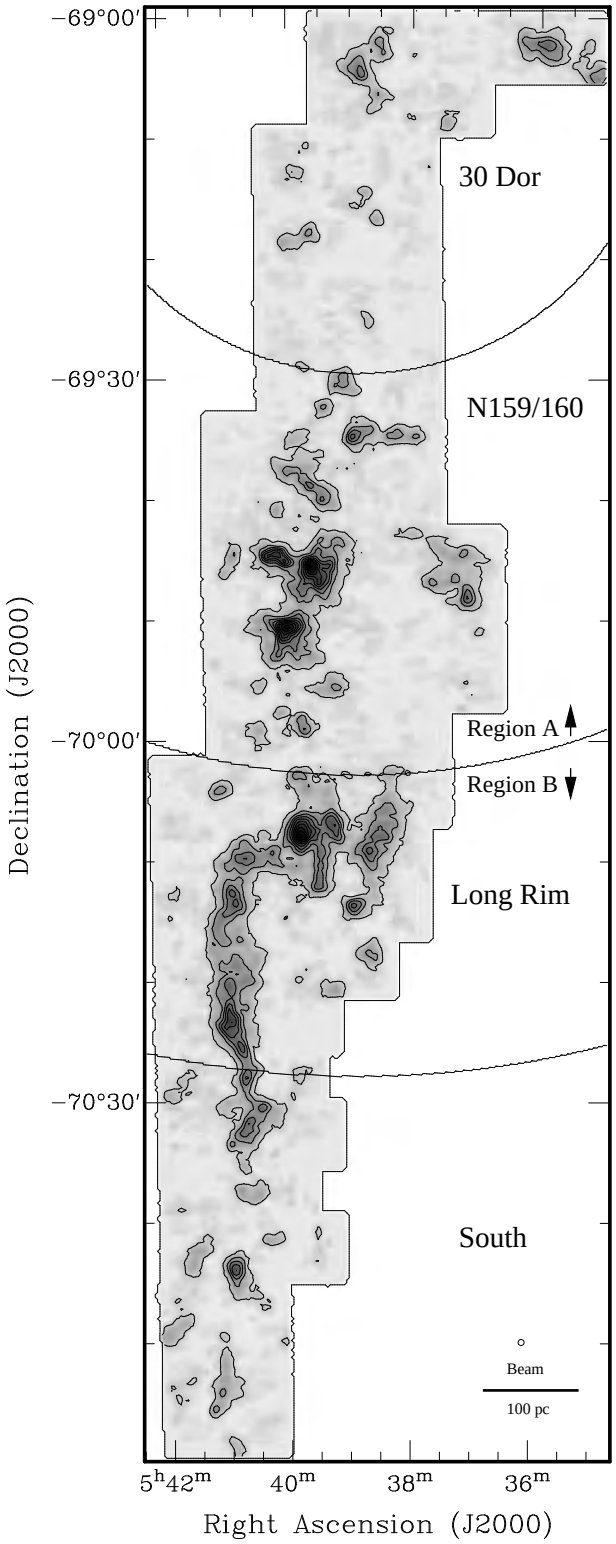

Fig. 4.31: *Map of the integrated intensity of the* ^{12}*CO* $J = 1 \rightarrow 0$ *line of the 30 Dor molecular ridge obtained with the Mopra telescope, overlaid with its own contours. The contour levels correspond to the 5% to 85% of the peak intensity (53 K km* s^{-1}*) in steps of 10%. Thick lines define four different regions: 30 Dor, N159/160, Long rim, and South. The arrows denote the two regions (Region A and B) used in the determination of the clump-mass spectrum (Sec. 4.4.5).*

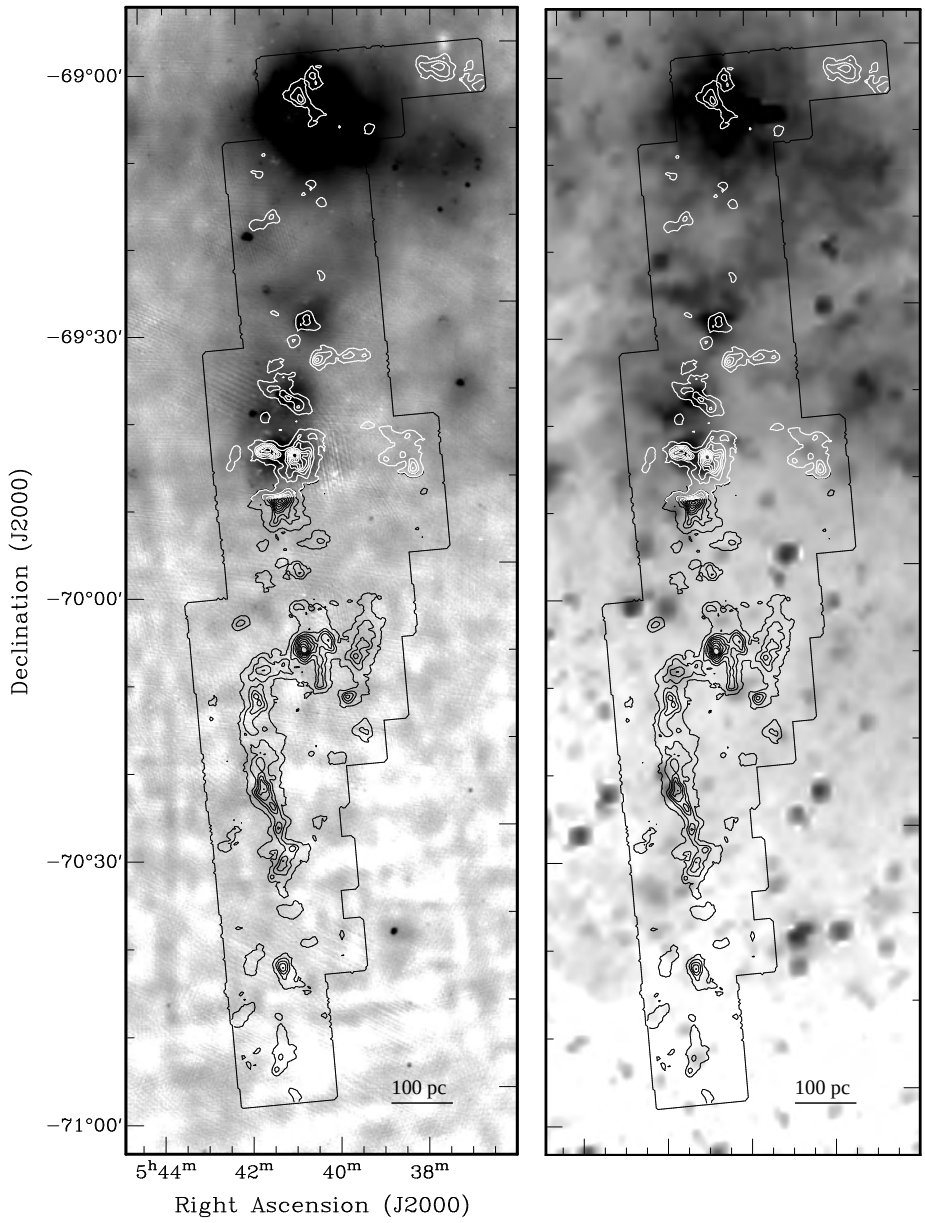

Fig. 4.32: *(left) 8.6 GHz radio continuum and (right) Hα maps overlaid with the line-integrated intensity ^{12}CO $J = 1 \rightarrow 0$ map of the 30 Dor molecular ridge. They are shown in logarithmic scale. In both maps the observed intensity peaks in the 30 Dor region and progressively decreases as the molecular ridge extends southward.*

superimposed as contour lines in each case. Considering the 8.6 GHz radio continuum and the Hα as tracers of the strength of the far-ultraviolet flux we can see that this quantity decreases as a function of distance to 30 Dor. This is illustrated in Fig. 4.33, which shows the average Lyman continuum emissivity a function of distance to 30 Dor. We calculate the emissivities from the 8.6 GHz radio continuum intensity at the positions

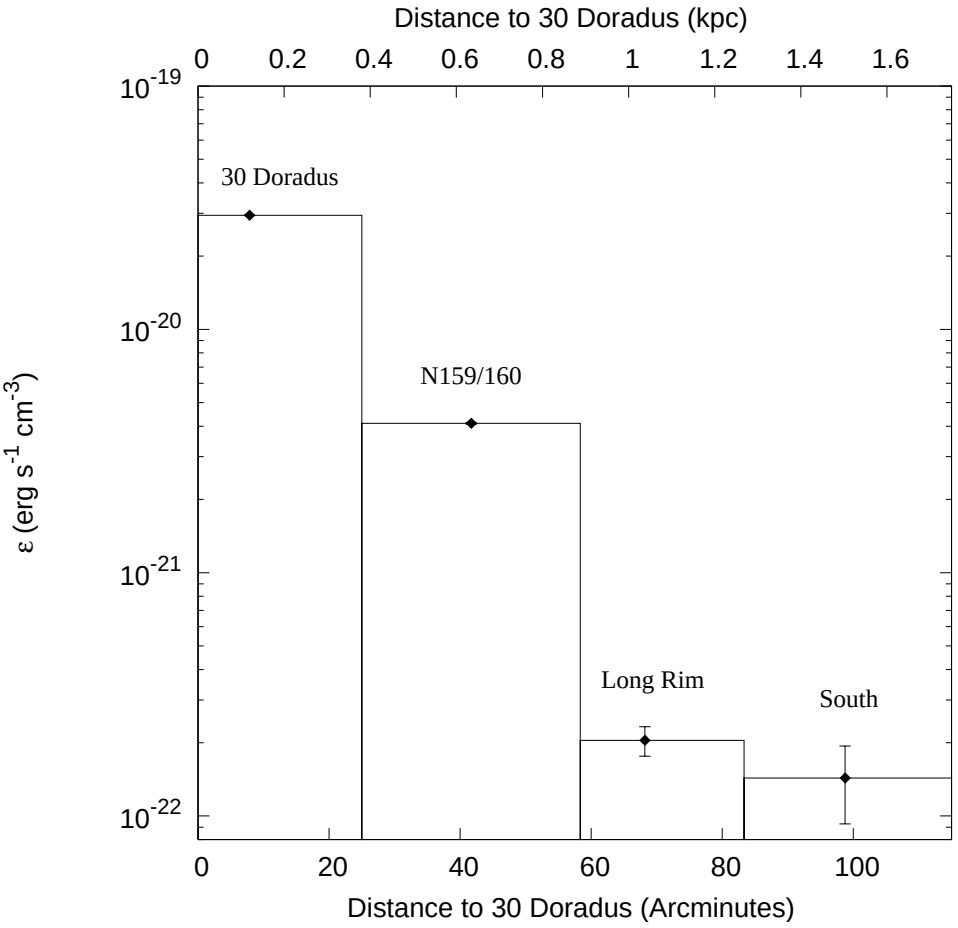

Fig. 4.33: *Averaged Lyman continuum emissivity as a function of distance to 30 Dor. The emissivities are derived from the 8.6 GHz radio continuum intensity and they are averaged in each defined region (Fig. 4.31).*

where we identify clumps and we average them in the regions defined in Fig. 4.31. We first calculate the number of Lyman continuum photons in the beam of the observations using (Appenzeller et al., 1980, Chap. 2)

$$\left(\frac{N_{\rm L}}{\rm phot\,s^{-1}}\right) = 7.54\times10^{46}\left(\frac{\nu}{\rm GHz}\right)^{0.1}\left(\frac{T_{\rm e}}{10^4 K}\right)^{-0.45}\left(\frac{S_\nu}{\rm Jy\,beam^{-1}}\right)\left(\frac{D}{\rm kpc}\right)^2,$$

where ν is the frequency of the observation, $T_{\rm e}$ the electron temperature, S_ν is the flux density per beam, and D the distance. Assuming an electron temperature of $T_{\rm e} = 10^4$ K and that the energy of the Lyman continuum photons is 13.6 eV, we obtain the Lyman continuum emissivity, ϵ, by dividing the Lyman continuum energy rate by the volume of a sphere of the size of the beam. As we can see, the Lyman continuum emissivity increases by about two orders of magnitude from the southern region to 30 Dor. Thus,

clouds close to this region are exposed to stronger FUV radiation fields – and therefore different physical conditions – than those in the N159/160 region; conditions there are still extreme compared to more quiescent regions far south of 30 Dor. This allows the study of the properties of the molecular gas as a continuous function of the ambient radiation field in a low-metallicity environment.

4.4.2 Clump Decomposition

In order to study the properties of the molecular gas in the 30 Dor molecular ridge, we identified individual clumps using the software package `GAUSSCLUMPS` (Stutzki & Güsten, 1990; Kramer et al., 1998). `GAUSSCLUMPS` decomposes the observed three-dimensional intensity distribution into emission of individual, Gaussian shaped clumps by iteratively subtracting fitted clumps. The iterative decomposition process is terminated when a new generation of clumps has peak intensities below 3 times the r.m.s. noise. The decomposition process provides clump parameters such as their position, Local Standard of Rest (LSR) velocity, clump orientation, spatial FWHMs along the spatial axes (Δx, Δy), brightness temperature ($T_{\rm mb}$), and FWHM velocity dispersion (Δv). The scale of the identified clumps is typically between 10–30 pc.

As `GAUSSCLUMPS` approximates irregularly shaped clumps by Gaussian clumps, artificially small, low-mass clumps can be accidentally identified by the algorithm. In order to reduce the importance of this effect, we only consider Gaussian clumps with fitted sizes larger than 110% of the spatial resolution (i.e. the deconvolved size is at least 40% of the instrumental resolution in the two spatial dimensions). The velocity dispersion of a clump is limited to be larger than 1.2 km s^{-1} in order to avoid clumps with a single pixel in velocity space. Kramer et al. (1998) described the stability of the results to variations of input parameters used in the decomposition of several molecular clouds in detail. In the decomposition of our observations, we adopt the standard set of parameters used in their analysis.

4.4.3 The CO-to-H_2 conversion factor

Although molecular hydrogen (H_2) is the most abundant molecular species in the Universe, it is difficult to observe directly in the typical physical conditions of molecular clouds, owing to its lack of an electric dipole transition. In practice, the total mass of molecular gas is often determined using a CO-to-H_2 conversion factor ($X_{\rm CO} \equiv N_{\rm H_2}/W_{\rm CO}$), which relates the observed intensity of CO, the second most abundant molecular species, to the column density of molecular hydrogen. This conversion factor is, however, not uniform among galaxies because it depends on the physical parameters of clouds, such as density and temperature, and also on environmental conditions, such as metallicity and the strength of the radiation field (Maloney & Black,

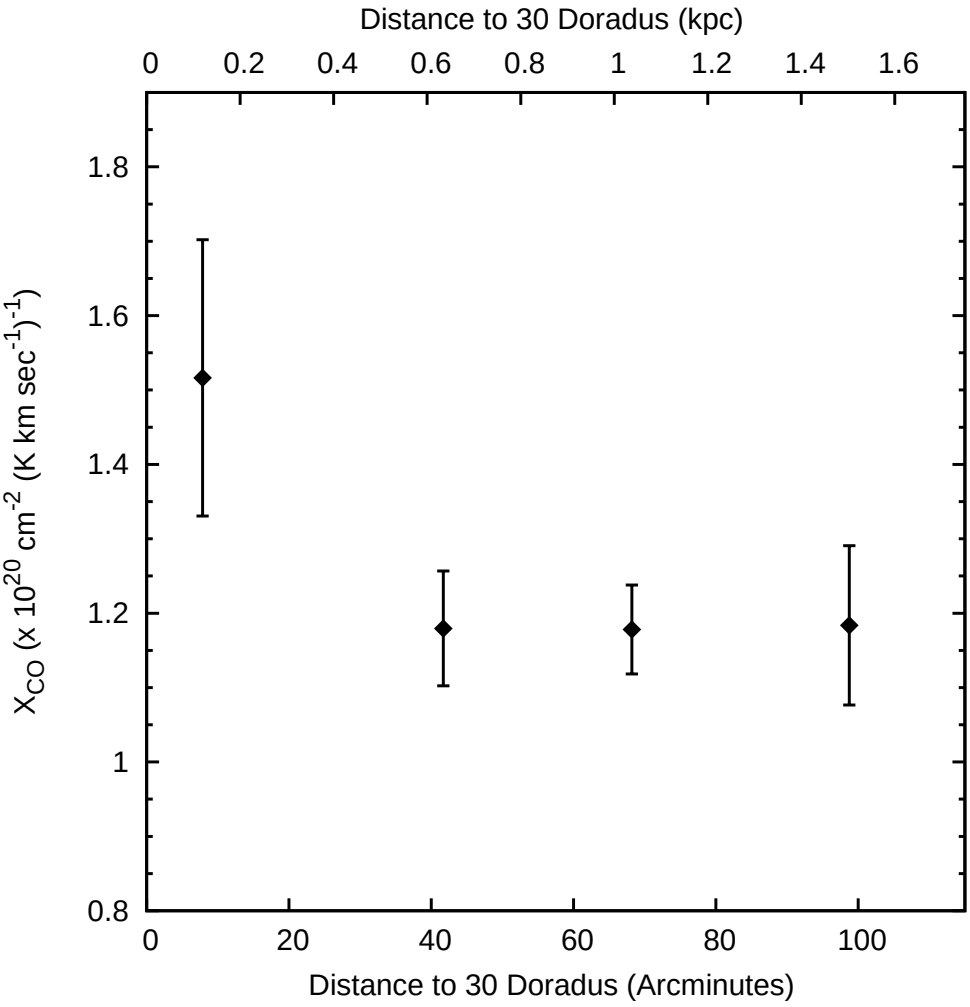

Fig. 4.34: *Average X_{CO} conversion factor as a function of distance to 30 Dor. Error bars are derived assuming a 30% error in the determination of X_{CO} and taking into account the number of clumps identified within each defined region (Fig. 4.31).*

1988). The understanding of the dependence of the conversion factor on these parameters is essential in order to determine the amount of molecular gas in high-redshift galaxies, for which X_{CO} is often the only means to derive the entire molecular content.

In the Milky Way, the X_{CO} conversion factor has been calculated using γ-ray observations (Bloemen et al., 1986), a method which is almost independent of the properties of molecular clouds. Using this method, a value of X_{CO} between 0.9 and 2.0×10^{20} cm^{-2} (K km $s^{-1})^{-1}$ is derived in Galactic molecular clouds (e.g. Strong et al., 1988; Digel et al., 1996, 1999; Hunter et al., 1997). Early studies of the LMC suggested that the X_{CO} conversion factor differs from that estimated in our Galaxy. For example, Cohen et al. (1988) found that for a given cloud velocity dispersion, the LMC clouds are underluminous by a factor of 6 compared with Galactic clouds, implying that the X_{CO}

conversion factor in the LMC is 6 times larger than the Galactic one. Also, Mizuno et al. (2001), assuming virialized clouds, found a value that is three times larger in the LMC than that found in the Galaxy. Note that both studies differ strongly in the spatial resolution of the observations (140 and 40 pc, respectively).

The variation of X_{CO} with metallicity has been studied by several authors (e.g. Dettmar & Heithausen, 1989; Rubio et al., 1991; Wilson, 1995; Arimoto et al., 1996; Sakamoto, 1996; Israel, 1997, 2000). All studies agree in that it scales inversely with metallicity as measured by the oxygen abundance. Israel (1997), studying individual clouds in the LMC, found a linear relation between X_{CO} and the radiation field (in terms of the radiative energy per nucleon, derived from infrared observations).

Assuming that in the 30 Dor molecular ridge metallicity gradients are negligible, the most prominent parameter that varies along this chain of molecular clouds is the strength of the FUV radiation field. This assumes that cloud parameters such as gas densities and temperatures vary as a consequence of the different strengths of the FUV field. Thus, we can study the variations of the X_{CO} conversion factor as a function of this quantity. In order to estimate the value of X_{CO} in our observations, we assume that the observed molecular clouds in the LMC are in virial equilibrium. Then, the conversion factor is calculated by dividing the virial mass by the luminosity of a clump. This allows us to obtain a value of the conversion factor for each identified clump. The virial mass, $M_{\rm vir}$, is defined by

$$\frac{M_{\rm vir}}{\rm M_\odot} = k \left(\frac{R}{\rm pc}\right) \left(\frac{\Delta \rm v}{\rm km\,s^{-1}}\right)^2, \tag{4.12}$$

where R is the deconvolved clump radius and Δv is the deconvolved FWHM of the observed line profile. The factor k depends on the assumed density profile of a clump (MacLaren et al., 1988). In the following, we adopt a value of $k = 210$, corresponding to a spherical cloud with uniform density. The clump radius is defined as

$$R = \left(\frac{D}{\rm pc}\right) \frac{\sqrt{\Delta x \Delta y}}{2}, \tag{4.13}$$

where D is the distance to the clump and Δx and Δy are the projected deconvolved FWHM angular sizes of the clump.

We choose to use deconvolved values in the calculation of the virial mass because it is an intrinsic property of the cloud. Some published studies used undeconvolved cloud parameters (i.e. they worked with the instrumental resolution). This leads to an overestimation of the virial mass, in particular if the cloud size and velocity dispersion are of the same order as the instrumental resolution. The different methods used to calculate the virial mass and other cloud parameters make the quantitative comparison with previous studies difficult, however.

We find an average X_{CO} conversion factor of $(1.2 \pm 0.1) \times 10^{20}$ cm^{-2} (K km s^{-1})$^{-1}$. This is comparable to the X_{CO} factor found in our Galaxy and is consistent with that found by Johansson et al. (1998) for the LMC. We note that our estimated conversion factor is lower compared to previous estimations in the LMC derived on larger linear scales (e.g. Cohen et al., 1988; Garay et al., 1993; Mizuno et al., 2001). Rubio et al. (1993) and Verter & Hodge (1995) have reported that X_{CO} decreases if the observations are performed with better spatial resolution. Our results supports this finding. This suggest that previous estimations of X_{CO} in extragalactic sources suffer from the low resolution of the observations.

Separating the identified clumps into four subregions which are exposed to different strengths of the FUV radiation field (Fig. 4.34), we find that X_{CO} increases for clumps closer to 30 Dor. In order to interpret the observed variations of the X_{CO} conversion factor, we quantify the dependence of X_{CO} on cloud parameters used for its calculation. The X_{CO} conversion factor relates the intensity of CO, given by

$$W_{CO} = \int T_{mb}\, dv \propto T_{mb}\, \Delta v, \tag{4.14}$$

to the column density of H_2. Here, T_{mb} is the main-beam brightness temperature and Δv the velocity dispersion of a clump. The column density of H_2, assuming that clouds are in virial equilibrium, can be written as

$$N(H_2) \propto \frac{M_{vir}}{R^2} \propto \frac{\Delta v^2}{R}, \tag{4.15}$$

where R is the projected radius of the clump. This results in a conversion factor X_{CO} that is related to observed quantities as

$$X_{CO} \propto \Delta v\, T_{mb}^{-1} R^{-1}. \tag{4.16}$$

Fig. 4.35 shows the average main-beam brightness temperature, velocity dispersion, and projected CO clump radius as a function of distance from 30 Dor. With the exception of the CO clump radius, these quantities show clear variations. The main-beam brightness temperature increases from the southernmost regions to N159/160. This increment can be produced by a rise of the gas temperature as the gas heating increases with the FUV radiation field and/or to a larger CO column density and/or an increased beam filling. Gas densities are not considered because they are likely to be higher than the critical density of ^{12}CO $J = 1 \rightarrow 0$ ($\sim 10^3$ cm^{-3}; e.g. Johansson et al., 1998; Poglitsch et al., 1995) and therefore this transition is thermalized. Between these two regions, X_{CO} stays constant (Fig. 4.34), because the increase in T_{mb} is compensated by a larger velocity dispersion. The increment of Δv can be related to an increase of turbulent motions introduced by stellar winds produced, for example, by newly formed

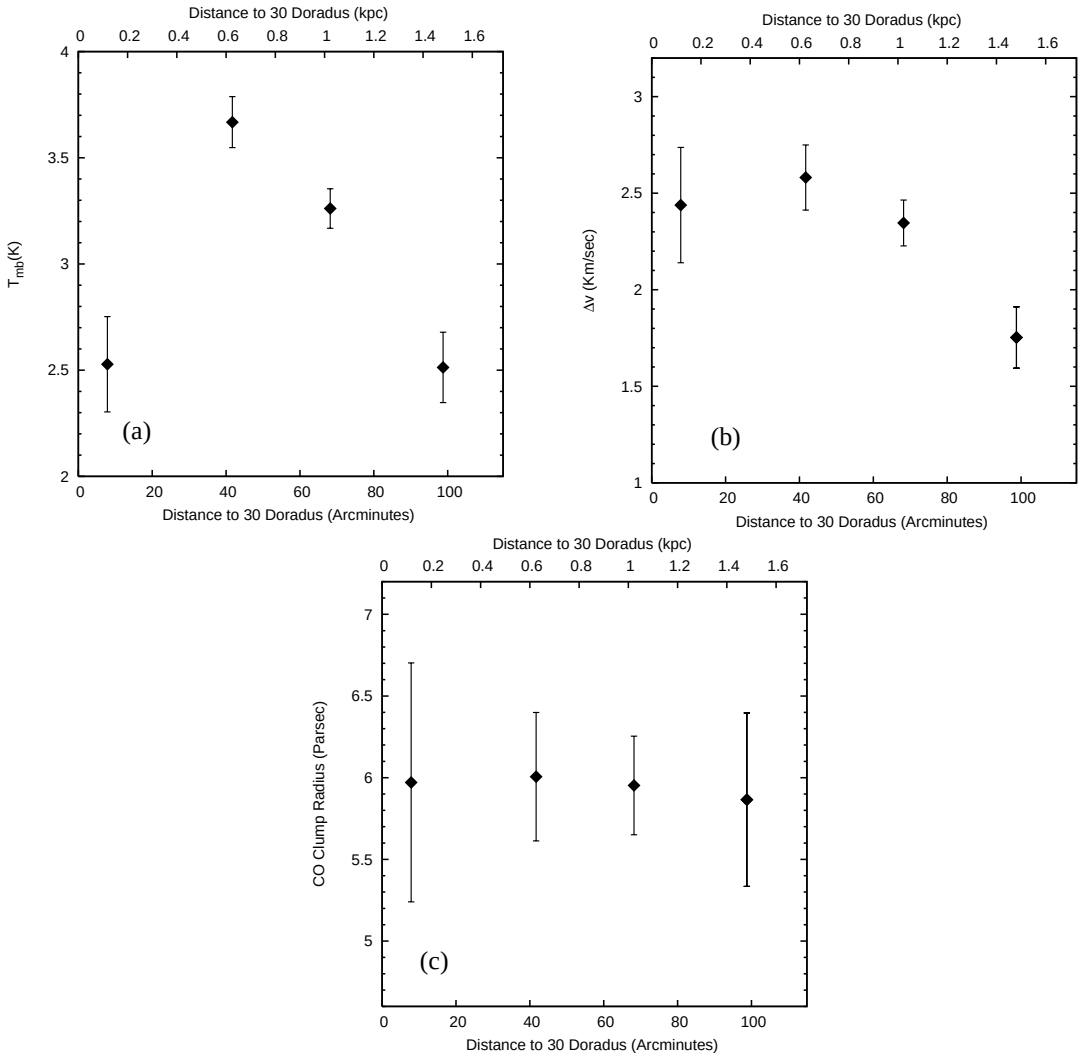

Fig. 4.35: *(a) Brightness temperature, (b) velocity dispersion, and (c) projected CO clump radius as a function of distance to 30 Dor. Error bars in brightness temperature are derived from the r.m.s. of the observations while, for the velocity dispersion and CO clump radius, they are derived assuming a 30% error. In all cases the error bars are weighted by the number of clumps identified in each defined region (Fig. 4.31).*

stars. Between N159/160 and 30 Dor, the gas temperature is further enhanced while the CO column density is constant (Johansson et al., 1998). However, $T_{\rm mb}$ decreases in 30 Dor. This increases the value of X_{CO} because Δv remains constant. The lower main-beam brightness temperature in 30 Dor is likely produced by a reduced beam filling in this region.

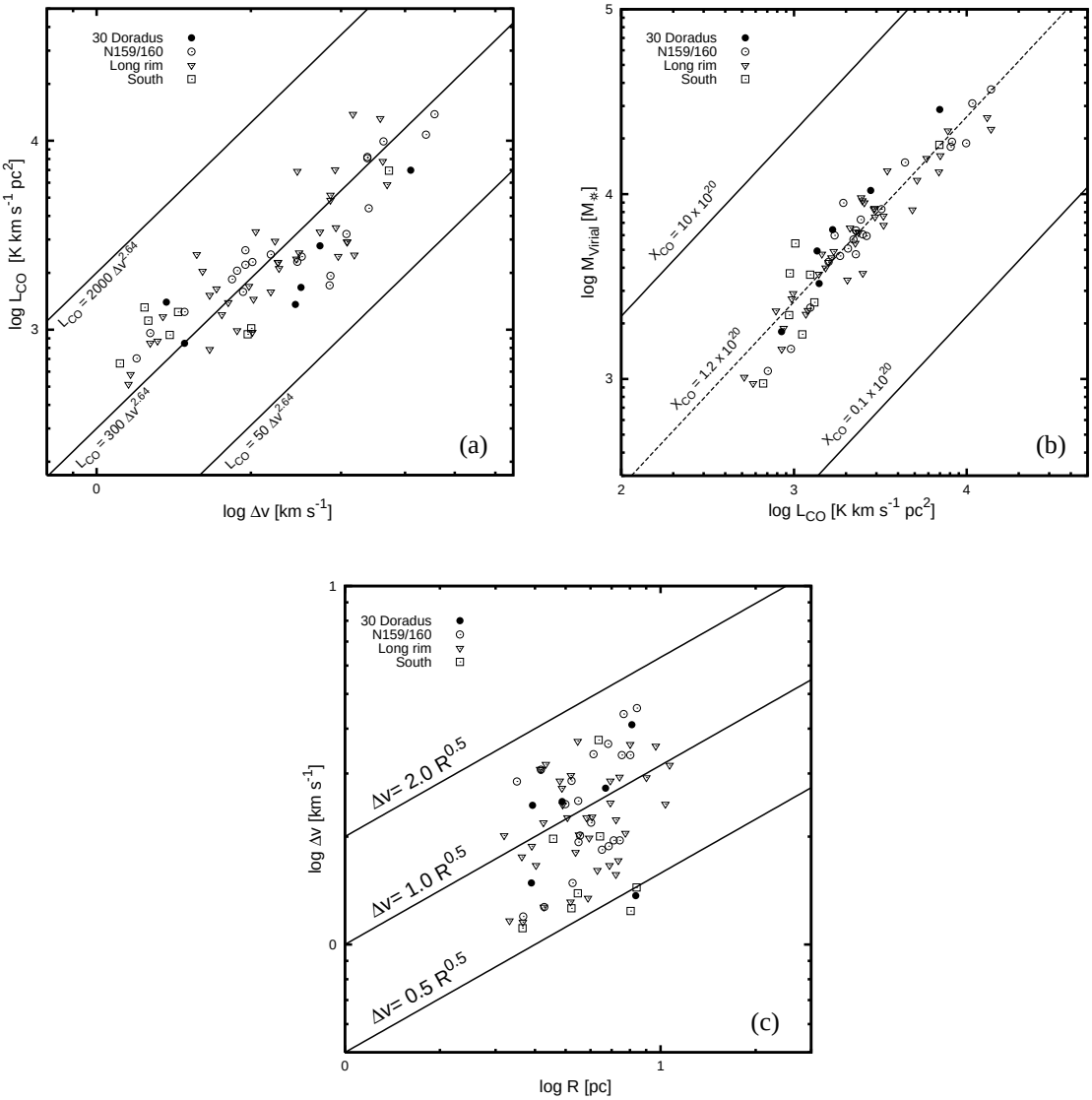

Fig. 4.36: *Relations between molecular cloud parameters of identified clumps in the 30 Dor molecular ridge. (a) The CO luminosity-velocity dispersion. The straight lines represent the Galactic relation. (b) Virial mass-CO luminosity relation. The diagonal lines correspond to constant X_{CO}, including the average value of our survey. (c) Velocity dispersion-size relation. The straight lines represent the Galactic relation. In all relations, different symbols correspond to the different regions defined in Fig. 4.31.*

4.4.4 Molecular Cloud Properties

Several studies of molecular clouds in our Galaxy have established a number of empirical relations between observable parameters (e.g. Larson, 1981; Myers, 1983; Dame

et al., 1986; Solomon et al., 1987). These relations link the CO luminosity and virial mass of a cloud, its size and velocity dispersion, and its CO luminosity and velocity dispersion.

The relations between molecular cloud parameters in our Galaxy are described by power-laws of the form $L_{\rm CO} \propto M_{\rm vir}^{\alpha}$, $\Delta {\rm v} \propto R^{\beta}$, and $L_{\rm CO} \propto \Delta {\rm v}^{\gamma}$. Similar power-laws are also observed in molecular clouds in the LMC, with the difference in the constants of proportionality (e.g. Cohen et al., 1988; Garay et al., 1993; Johansson et al., 1998; Mizuno et al., 2001). This has been suggested to be due to the different environmental conditions to which LMC clouds are exposed.

Fig. 4.36 shows the empirical relations for clumps identified in our survey. Different symbols correspond to the different regions defined in Fig. 4.31.

The relation between the CO luminosity and the velocity dispersion is shown in Fig. 4.36a. The straight lines represent the $L_{\rm CO} \propto \Delta {\rm v}^{2.64}$ relation found for Galactic clouds (e.g. Dame et al., 1986). The slope of the relation is consistent with that found in the Galaxy. We note that clumps located in the 30 Dor region tend to be underluminous compared with clumps further south with similar velocity dispersions. As seen in Sect. 4.4.3, this produces a larger $X_{\rm CO}$ factor in this region.

The virial-mass-to-CO-luminosity relation is shown in Fig. 4.36b. Diagonal lines correspond to constant values of the $X_{\rm CO}$ conversion factor, including the average value obtained in our survey (Sect. 4.4.3). Provided that the CO luminosity is an indicator of the amount of molecular gas traced by CO, the observed relation suggests that the degree of virialization of the clumps does not show any significant variation. In the particular case of the 30 Dor region, clumps tend to have larger virial mass for a given CO luminosity. This is a result of the larger velocity dispersions and lower CO luminosities observed in this region (see Sect. 4.4.3).

Fig. 4.36c shows the velocity-dispersion-size relation. The straight lines represent the $\Delta v \propto R^{0.5}$ relation observed in Galactic clouds. Although there is no clear correlation between the size and velocity dispersion of our clouds, our results are not inconsistent with the $\Delta v \propto R^{0.5}$ relation obtained for Galactic molecular clouds (e.g. Myers, 1983; Dame et al., 1986; Solomon et al., 1987). The limited range of sizes and velocity dispersions of our observations does not allow us to properly test this relation.

4.4.5 Clump-Mass Spectrum

A general property of molecular clouds is that they show self-similar structure over a wide range of scales. This hierarchical, clumpy structure is manifested, for example, in the clump-mass spectrum of molecular clouds. If clumps represent the final substructures that form stars, the clump-mass spectrum should be related to the Initial Mass Function (IMF) of stars as suggested by e.g. Zinnecker (1989). Furthermore,

high-resolution observations of dense cores indicate a mass spectrum that resembles the stellar Salpeter (1955) IMF (e.g. Motte et al., 1998; Testi & Sargent, 1998; Motte & André, 2001; Johnstone et al., 2000, 2001).

The clump-mass distribution in Galactic molecular clouds follows a power-law mass spectrum of the form $dN/dM \propto M^{-\alpha}$, with the power-law index α in the range from 1.4 to 1.9. This value holds over several orders of magnitude of clump mass (e.g. Elmegreen & Falgarone, 1996; Heithausen et al., 1998; Kramer et al., 1998), and is independent of the star-forming nature of the clouds (e.g. Williams et al., 1994). Previous observations of giant molecular clouds (GMC) in the LMC showed a power-law index of the mass spectra of $\alpha = 1.9$ (Fukui et al., 2001).

The effects of metallicity and FUV radiation fields can modify the distribution of clump masses in the ISM of the LMC. The expected reduction of the CO size of clumps under these conditions should be reflected in the slope of the clump-mass spectrum. In order to study the influence of the FUV radiation field on the clump-mass spectrum, we divide the 30 Dor molecular ridge into two sub-regions: Region A, which encloses the 30 Dor and N159/160 regions, and is therefore exposed to strong FUV radiation fields, and Region B, which consists of clouds exposed to weaker radiation fields (long rim and southern regions).

In the literature, the clump-mass spectrum based on ^{12}CO data is often calculated using clump masses derived from the clump luminosity by applying a uniform X_{CO} conversion factor. In the present study we use virial masses for the calculation of the mass spectrum because, as we have seen in Sect. 4.4.3, X_{CO} is not uniform throughout the 30 Dor molecular ridge.

The introduction of a cutoff criterion which discards clouds with low CO emission and noise features in the decomposition implies that some low-mass clumps are missed in the clump-mass spectrum. This effect produces a turnover in the mass spectra. This turnover marks the last mass bin at which the loss of low-mass clumps is expected to occur. A least-squares fit to the clump mass spectrum is therefore applied only to high-mass bins beyond this turnover.

Fig. 4.37 shows the clump-mass spectrum for Region A, Region B and for the entire observed region. A least-squares fit of $dN/dM \propto M^{-\alpha}$ is applied to masses larger than the mass that marks the turnover in the spectrum, resulting in exponents $\alpha_A = 1.61 \pm 0.37$, $\alpha_B = 1.56 \pm 0.32$ and $\alpha_{Total} = 1.91 \pm 0.29$ for Region A, Region B and the complete region, respectively. These were determined by least-squares fits to the mass distributions, taking into account the $(\Delta N)^{1/2}$ statistical error in the distributions, using the routine published by Press et al. (1992). The spectrum is well-fitted by a single power-law, over the mass range of $10^{3.8} < M/M_\odot < 10^{4.5}$.

The derived clump-mass spectra show exponents of the power-law which, for a similar range of masses, are consistent with those obtained in the outer Galaxy ($\alpha = 1.73$, Heyer & Terebey, 1998). They are also similar to that previously found in the LMC

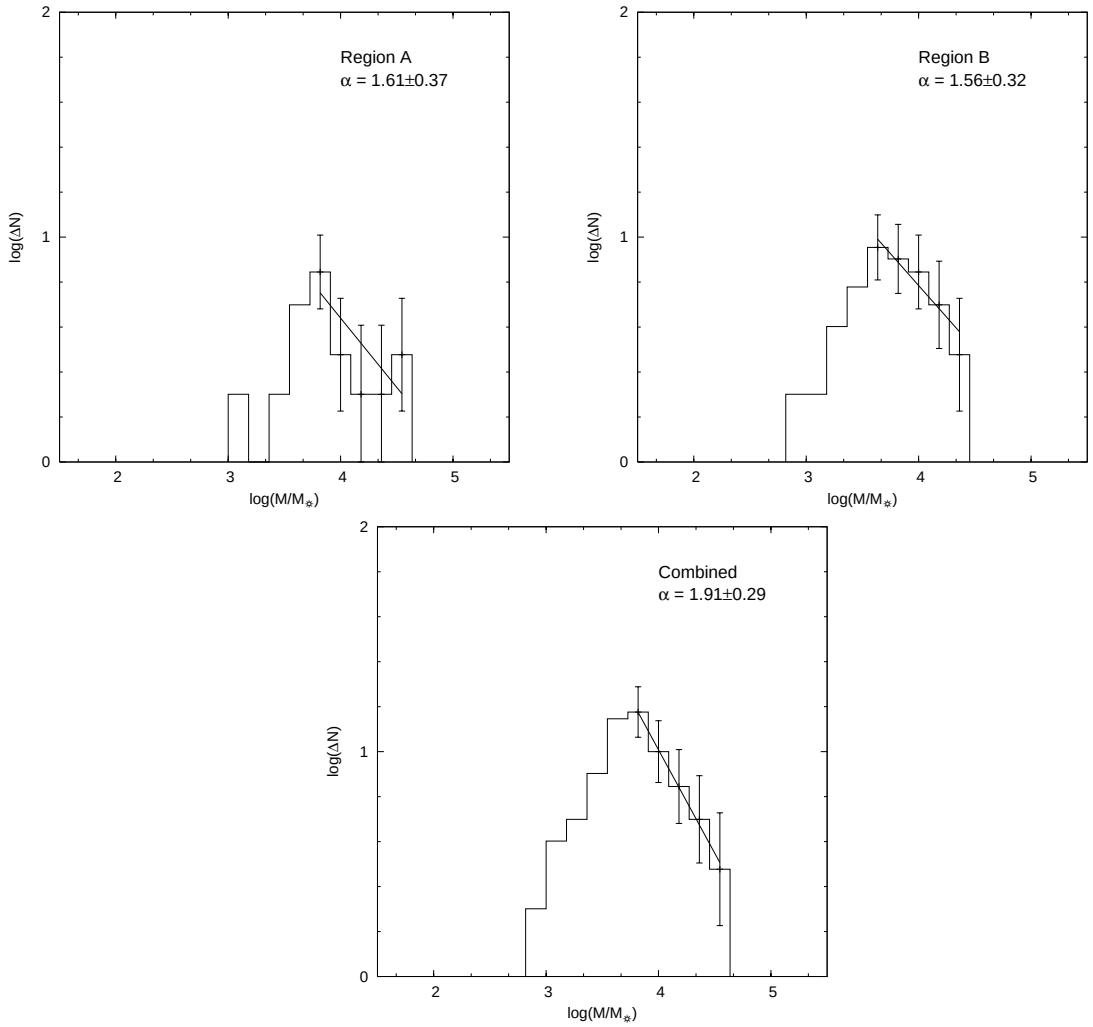

Fig. 4.37: *Clump-mass spectra for Region A, Region B and for the entire data set (see Fig. 4.31). The straight lines over the clump spectra represents the best power-law fit over a range of masses beyond the turnover (completeness limit).*

(α = 1.9, Fukui et al., 2001). Although the observed increase of the velocity dispersion and the rather constant clump size (Fig. 4.35) suggest larger virial masses in Region A, the large error bars in the clump-mass spectrum do not allow to see any significant difference in the power-law index between Region A and B.

4.5 Discussion

As outlined in the previous sections, the global properties of molecular clouds in the LMC are similar to those of Galactic clouds. However, locally we have found evidence for the FUV radiation field to affect the structure ISM in the 30 Dor region where the

X_{CO} conversion factor is larger compared to other regions. We attribute this increase to a reduced beam filling factor in CO due to it being preferentially dissociated relative to H_2 in low-density regions.

The average X_{CO} conversion factor found in our survey is similar to that found in Galactic clouds. As we can see in Fig 4.31, the molecular ridge is composed of few cloud complexes with linear scales between 100 – 300 pc. Those cloud complexes show substructures on scales between 10 – 30 pc, which is characterized by compact clumps connected by low surface brightness gas. Since GAUSSCLUMPS decomposes the clouds fitting local CO intensity peaks, this substructure is the one characterized in the present paper. Therefore, the average X_{CO} estimated in our survey refers to scales between 10 – 30 pc. The large cloud complexes do not necessarily have the same X_{CO} of the individual clumps. Although the clump size increases by about a factor of 10 making the virial mass larger, the CO luminosity does not scale by the same amount due to the presence of the low surface brightness inter-clump gas. This produces an increase of X_{CO} at larger scales as shown e.g. by Bolatto et al. (2003). Observations at lower angular resolutions trace these large-scale complexes rather than small clumps. This can explain the larger values of X_{CO} found in previous surveys in the LMC. The scale of the observed structures has to be considered when the total molecular mass of more distant or high-redshift galaxies is calculated.

The internal structure of the clumps identified in our survey can be represented by an ensemble of spatially unresolved subclumps embedded in a lower-density inter-subclump medium (Fig. 4.38). These subclumps have projected sizes that are smaller than the telescope beam so that many subclumps contribute to the total observed emission. In this medium, the far-ultraviolet photons can penetrate deep into the clumps and isotropically irradiate the subclumps due to scattering (Boisse, 1990; Meixner & Tielens, 1993). This picture has been previously used to describe the properties of the ISM in the LMC and other irregular galaxies (e.g. Rubio et al., 1993; Elmegreen, 1989; Garay et al., 1993). Evidence for substructure smaller than 10 pc has been found in the LMC by Wong et al. (2006). In a low-metallicity gas, the photodissociation of CO is enhanced while H_2 remains unaffected (van Dishoeck & Black, 1988). This reduces the size of the subclumps when they are traced by CO. The CO sizes of subclumps is further reduced when an extreme far-ultraviolet radiation field interacts with the molecular material. This is the case in the 30 Dor region. The smaller CO subclumps fill the beam of the observations less efficiently, thus reducing the observed brightness temperature and, as seen in Section 4.4.3, reducing X_{CO}.

The increased importance of beam filling has been used to explain the weak CO intensity (e.g. Israel et al., 1986; Johansson et al., 1998) as well as the increased [C II]/^{12}CO $J = 1 \rightarrow 0$ (Mochizuki et al., 1994; Poglitsch et al., 1995; Israel et al., 1996) line intensity ratio observed toward the LMC relative to the Milky Way. Johansson et al. (1998) have noticed an enhanced [C II]/^{12}CO $J = 1 \rightarrow 0$ line intensity ratio in the 30 Dor region compared with that in the N159 region. This suggests that the amount of mass in

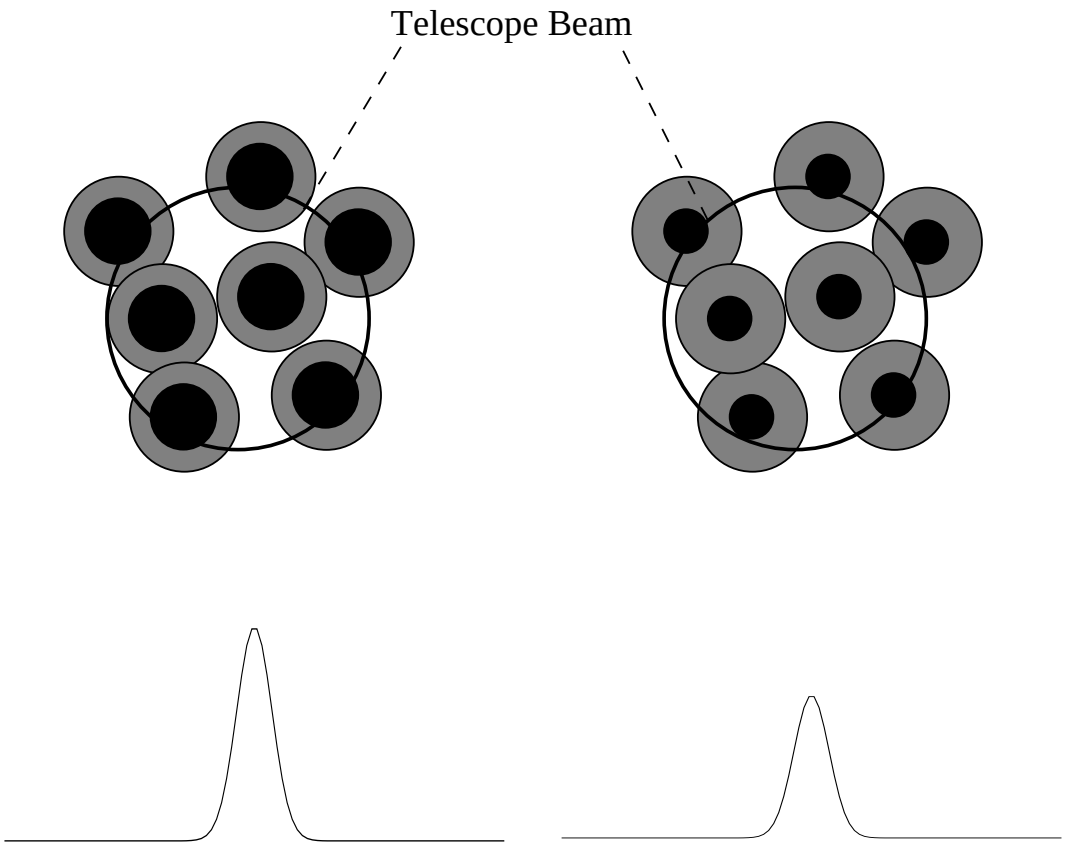

Fig. 4.38: *Sketch of clouds in quiescent regions (left) and clouds exposed to strong FUV radiation fields (right). The grey color represents the H_2 size of the clumps while the black color represent the CO size. The strong FUV radiation field reduces the CO size of the clumps and therefore they are less able to fill the beam. As a consequence, the emerging line emission is weaker.*

a photon-dominated region (traced by [C II]) relative to the molecular mass unaffected by the far-ultraviolet radiation (traced by CO) is enhanced in the 30 Dor region.

A reduced beam filling is not evident in clumps in the N159/160 regions, probably due to the high densities suggested by CO excitation analyses ($10^4 - 10^5$ cm^{-3}; Johansson et al., 1998; Bolatto et al., 2005; Minamidani et al., 2007). At high densities, the penetration of FUV photons into the molecular material is reduced, thus decreasing the extent of the CO photo-dissociation. In this case the amount of molecular mass traced by CO is larger compared to that in lower density clouds. Consequently, high-density regions have lower X_{CO}. In regions more distant from 30 Dor the penetration of FUV photons into the molecular gas is decreased because of the weaker FUV radiation field

and therefore CO is photo-dissociated less efficiently. This may explain the lower X_{CO} found in the southernmost regions. The arguments made above have been suggested by several photon-dominated region (PDR) models (e.g. Kaufman et al., 1999; Bell et al., 2006).

4.6 Summary and Conclusions

We have presented a large-scale ^{12}CO $J = 1 \rightarrow 0$ survey of the 30 Dor molecular ridge in the Large Magellanic Cloud. From the analysis of these observations we conclude the following:

1. The average CO-to-H_2 conversion factor obtained in our survey is $X_{CO} = (1.2 \pm 0.1) \times 10^{20}$ cm^{-2} (K km s^{-1})$^{-1}$, which is consistent with the Galactic conversion factor. We find that X_{CO} is larger for molecular clouds in the immediate surroundings of the 30 Dor region where they are exposed to extreme FUV radiation fields. The higher value of X_{CO} is related to an increase of the velocity dispersion in the 30 Dor and N159 regions compared with regions further south, and to a decrease of the brightness temperature of clumps in the 30 Dor region. Effects of beam filling decrease the observed clump brightness temperature, while turbulence associated with newly formed stars increases the velocity dispersion.

2. Studying the empirical relations in the observed clumps, we find that the molecular clouds in the LMC ridge exhibit properties similar to those in the Galaxy. The degree of virialization of the clumps shows only small variations along the molecular ridge. In case of the 30 Dor region, we find that clumps have lower CO luminosities compared to clouds further south with similar velocity dispersions; they have larger virial masses compared to clumps with similar luminosities.

3. The analysis of the clump-mass spectrum of molecular clouds in the 30 Dor molecular ridge results in a power-law index of $\alpha = 1.61 \pm 0.37$ in a region exposed to a strong FUV field, and $\alpha = 1.56 \pm 0.32$ in a more quiescent one. The power-law index in the entire molecular ridge is $\alpha = 1.91 \pm 0.29$. The obtained power-law indices are consistent with those found in Galactic clouds and in the entire LMC. Due to the large error bars, we do not find any significant difference of the slopes in the clump mass spectra of ridge regions immersed in low and high radiation fields.

5 Photon Dominated Region Modeling of the N159W Region in the LMC.

5.1 Introduction

The processes of star formation in the Large Magellanic Cloud (LMC) differ from those of the Milky Way. This is due to the intense far-ultraviolet (FUV) radiation field, which interacts with the low-metallicity, low-dust-to-gas ratio molecular gas in the LMC.

In low-metallicity environments the FUV field can penetrate deeper into the dense molecular gas (Israel, 1988; Maloney, 1990; Lequeux et al., 1994). This has an important impact on the outer layers of molecular clouds where FUV photons dominate the chemistry and thermal balance of the gas, i.e. in photon-dominated regions (PDRs). In the low-metallicity molecular gas carbon chemistry is especially affected. The abundances of C^+ and C relative to CO are increased due to the enhanced photodissociation of CO, which is less efficiently shielded against FUV photons compared to H_2 (van Dishoeck & Black, 1988). Therefore, the study of low-metallicity PDRs can give important insights into the properties of the molecular gas in the LMC.

One ideal example of massive star formation in a low-metallicity environment is the N159W region. This region is associated with the Henize (1956) H II region N159 and might be ionized by the equivalent of five O5V stars (Bolatto et al., 2000). N159W is the region which shows the strongest CO intensity in the entire LMC (Cohen et al., 1988; Fukui et al., 2001; Johansson et al., 1998), and it has been regarded as a hot core. The region has been observed in ^{12}CO $J = 4 \rightarrow 3$ and [C I] $^3P_1 \rightarrow ^3P_0$ (Stark et al., 1997; Bolatto et al., 2000, 2005) and in [C II] (Mochizuki et al., 1994; Israel et al., 1996).

In the following we study the properties of the low-metallicity molecular gas in the context of PDRs. For this purpose, we utilize observations of the ^{12}CO $J = 1 \rightarrow 0$, $J = 4 \rightarrow 3$, $J = 7 \rightarrow 6$, and ^{13}CO $J = 4 \rightarrow 3$ rotational transitions as well as the [C I] $^3P_2 \rightarrow ^3P_1$ and $^3P_1 \rightarrow ^3P_0$ fine-structure transitions observed toward N159W. With this dataset we provide a self-consistent solution of the chemistry and thermal balance of an isotropically irradiated spherical cloud using the PDR model developed by Störzer et al. (1996) (KOSMA$-\tau$). The observations are summarized in Sect. 5.2. The PDR model is described in Sect. 5.3 and the results are presented in Sect. 5.4. In Sect. 5.5 we discuss the results, and a summary is given in Sect. 5.6.

5.2 Observations

The ^{12}CO $J = 4 \rightarrow 3$, $J = 7 \rightarrow 6$, and ^{13}CO $J = 4 \rightarrow 3$ rotational transitions and the [C I] $^3P_2 \rightarrow ^3P_1$ and $^3P_1 \rightarrow ^3P_0$ fine-structure transitions were observed at unprecedented

Tab. 5.15: *Spectral Line Observations Toward N159W*

Telescope	Transition	$\theta_{\rm mb}$ [arcsec]	$\eta_{\rm mb}$	Δv [km sec^{-1}]	r.m.s. noise [K/Channel]
NANTEN2	[C I] $^3P_2 \rightarrow ^3P_1$	25	0.3	0.21	0.37
NANTEN2	[C I] $^3P_1 \rightarrow ^3P_0$	40	0.45	0.35	0.25
Mopra	^{12}CO $J = 1 \rightarrow 0$	45	0.42	0.48	0.47
NANTEN2	^{12}CO $J = 4 \rightarrow 3$	45	0.45	0.37	0.14
NANTEN2	^{12}CO $J = 7 \rightarrow 6$	25	0.3	0.21	0.63
NANTEN2	^{13}CO $J = 4 \rightarrow 3$	45	0.45	0.38	0.7

high-angular resolution with the NANTEN2 telescope located in Chile. The ^{12}CO $J = 7 \rightarrow 6$, ^{13}CO $J = 4 \rightarrow 3$, and [C I] $^3P_2 \rightarrow ^3P_1$ transitions were detected for the first time in the LMC. The ^{12}CO $J = 1 \rightarrow 0$ were made with the Mopra 22-m telescope (Chapter 4). A summary of the parameters of observations is listed in Table 5.15 and the observed spectra are shown in Figure 5.39.

The NANTEN2 observations were made using a two-channel, single-pixel receiver for simultaneous observations at 490 and 810 GHz. The observations correspond to a single pointing toward the peak position of the N159W region located at $\alpha = 5^{\rm h}39^{\rm m}36.''8$ and $\delta = -69°45'31.''91$ (J2000). Typically, a 3rd-order polynomial was fitted and subtracted from the spectra. A more detailed description of the observations is presented in Fukui et al. (2007).

5.3 PDR model

In order to investigate whether the emission from N159W can be explained by current photo-chemical models, we analyze the [C I] and CO emission using the PDR model developed by Störzer et al. (1996) (KOSMA$-\tau$). This model assumes a spherical clump isotropically irradiated by an external FUV radiation field. We adopt a density distribution of the cloud with a truncated power-law profile of the form

$$n(r) = n_{\rm s}(r/r_{\rm cl})^{-1.5},$$

for $0.2 \leq r/r_{\rm cl} \leq 1$, and

$$n(r) = 11.2\, n_{\rm s}.$$

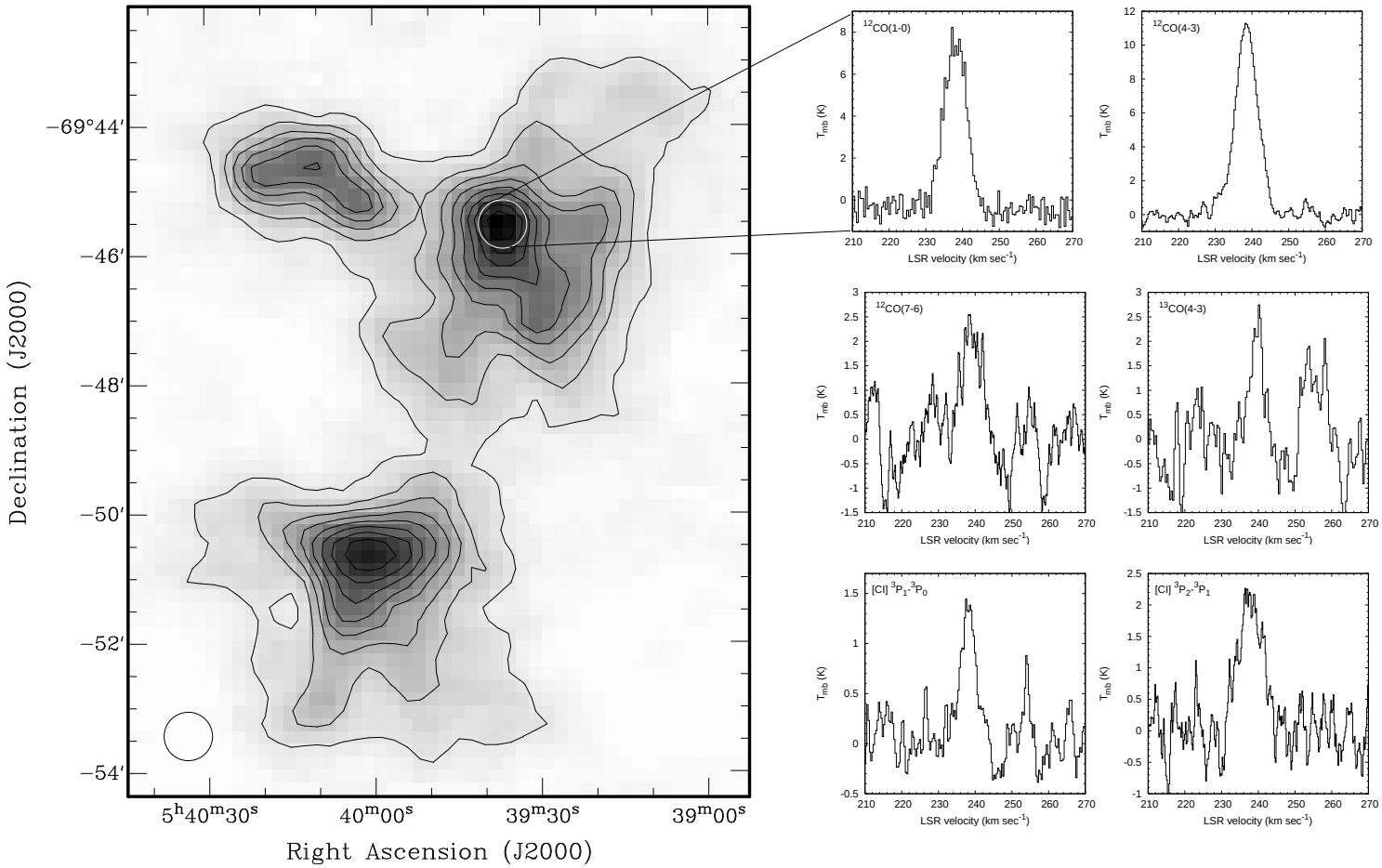

Fig. 5.39: *Left: Map of the* $^{12}CO\ J = 1 \rightarrow 0$ *emission of the N159 region. The contours run from 10% to 90% of the peak intensity (52.3 K km* s^{-1}*) in steps of 10%. The white circle indicates the position where the observations toward N159W were made. Right: Observed spectra toward N159W.*

Tab. 5.16: *Model parameters of the spherical PDR code.*

Model Parameters		
$M_{\rm cl}$	$10^{-6}\ldots100$ M$_\odot$	Clump mass
$\langle n\rangle_{\rm cl}$	$3\times10^{4}\ldots3\times10^{8}$ cm^{-3}	average clump density
$n_{\rm s}$	$n_{\rm s}\approx0.5\times\langle n\rangle_{\rm cl}$	clump surface density[a]
$\zeta_{\rm CR}$	5×10^{-17}s^{-1}	CR ionization rate
$A_{\rm v}$	$6.3\times10^{-22}\times N_{\rm H_{tot}}$	visual extinction
$\tau_{\rm UV}$	$3.68A_{\rm v}$	FUV dust attenuation
b	1 km s^{-1}	Doppler width
He	0.1	abundances[b]
C	1.4×10^{-4}	
O	3.0×10^{-4}	
N	7.9×10^{-5}	
^{13}C	2.15×10^{-6}	
S	2.8×10^{-5}	
Mg	1.1×10^{-6}	
Fe	1.7×10^{-7}	
Si	1.7×10^{-6}	
PAH	4.0×10^{-7}	

[a] For a truncated power-law density profile $n\propto r^{-1.5}$.
[b] Initial abundance, relative to H nuclei.

for $r/r_{\rm cl}\leq0.2$, where $r_{\rm cl}$ is the clump radius and $n_{\rm s}$ the clump surface density . This density profile corresponds to that of a marginally bound polytropic gas sphere (Chieze, 1987). The model provides a self-consistent solution of the thermal balance (heating and cooling) and chemistry (abundance of species). This results in abundances and temperature profiles which are then used by the `ONION` radiative transfer code (Gierens et al., 1992) in order to calculate the peak and line-integrated intensity of the ^{12}CO and ^{13}CO rotational transitions as well as the [C I] and [C II] fine structure transitions. A summary of the initial model parameters and adopted abundances is listed in Table 5.16. A detailed description of the treatment of metallicity in the PDR model is given by Röllig et al. (2006).

5.4 Results

In the following we use the PDR model in order to identify the typical mass and density of the clumps that better reproduce the observed line ratios. Following Bensch (2006), we assume that the modelled clumps are much smaller than the beam of the observations and that we can describe the observed line ratios considering an

Tab. 5.17: *Line-integrated intensity ratios observed toward N159W.*

Line Ratio[a]	
[C I] $^3P_2 \rightarrow ^3P_1/^{12}CO$ $J = 7 \rightarrow 6$	0.75± 0.3
[C I] $^3P_1 \rightarrow ^3P_0/^{12}CO$ $J = 1 \rightarrow 0$	25.5±10.2
[C I] $^3P_1 \rightarrow ^3P_0/^{12}CO$ $J = 4 \rightarrow 3$	0.12±0.05
[C I] $^3P_1 \rightarrow ^3P_0/^{13}CO$ $J = 4 \rightarrow 3$	0.97±0.38

[a] Based in line-integrated intensities in units of erg cm^{-2} s^{-1} sr^{-1}.

ensemble of clumps with the same mass and density. These clumps are not radiatively coupled and effects of shadowing are negligible. This does not rule out the presence of clumps with different mass and densities, but assumes that they do not dominate the observed line emission. We run a grid of 9×9 PDR models where each model is characterized by a mass and a clump-averaged density. The clump mass in the grid ranges from 10^{-6} M$_\odot \leq M_{\rm cl} \leq 100$ M$_\odot$, while the clump density runs from $3 \times 10^4 \leq \langle n \rangle_{\rm cl} \leq 3 \times 10^8$ cm^{-3}. For N159W, we adopt a metallicity of $0.5\,Z_\odot$ (Westerlund, 1997) and a strength of the FUV radiation field of $176\,\chi_0$ (Israel et al., 1996), where χ_0 is the mean FUV radiation field (Draine, 1978).

In order to compare with the PDR model, we use the [C I]/CO line-integrated intensity ratios listed in Table 5.17. We choose these ratios because the transitions of each pair are observed with similar angular resolutions. Fig. 5.40 shows the line-integrated intensity ratios obtained by the model grid as a function of clump mass and density. The line ratios are based in observations at a scale of 11 pc (45″ at a distance of 50 Kpc), with the exception of [C I] $^3P_2 \rightarrow ^3P_1/^{12}CO$ $J = 7 \rightarrow 6$ which is based in observations at 6 pc (25″). In order to compare all observed line ratios with the PDR model, they have to trace the same material. For that, we assume that the clumps we model are much smaller than 6 pc.

We compare the observations with the model results by calculating the quantity Q^2 using the same procedure described in Sect. 3.4.3. The quantity Q^2 is plotted as a function of the average clump mass and clump density. Fig. 5.41 shows the Q^2 for the studied model grid.

The models with line ratios that are closer to the observed values suggest clumps with a density of $\langle n \rangle_{\rm cl} = 10^{7.2}$ cm^{-3} and masses between $10^{-3} - 10^{-4}$ M$_\odot$. As we can see in Fig. 5.40, the [C I] $^3P_2 \rightarrow ^3P_1/^{12}CO$ $J = 7 \rightarrow 6$ and [C I] $^3P_1 \rightarrow ^3P_0/^{12}CO$ $J = 4 \rightarrow 3$ line-integrated intensity ratios suggest high densities but do not constrain the clump mass. The latter quantity is constrained by the [C I] $^3P_1 \rightarrow ^3P_0/^{12}CO$ $J = 1 \rightarrow 0$ and ^{13}CO $J = 4 \rightarrow 3$ line ratios. We note that high densities are the result of the low observed [C I] $^3P_1 \rightarrow ^3P_0/^{12}CO$ $J = 4 \rightarrow 3$ line ratio. Other line integrated-intensity ratios suggest somewhat lower densities ($\sim 10^6$ cm^{-3}) and higher masses (~ 1 M$_\odot$).

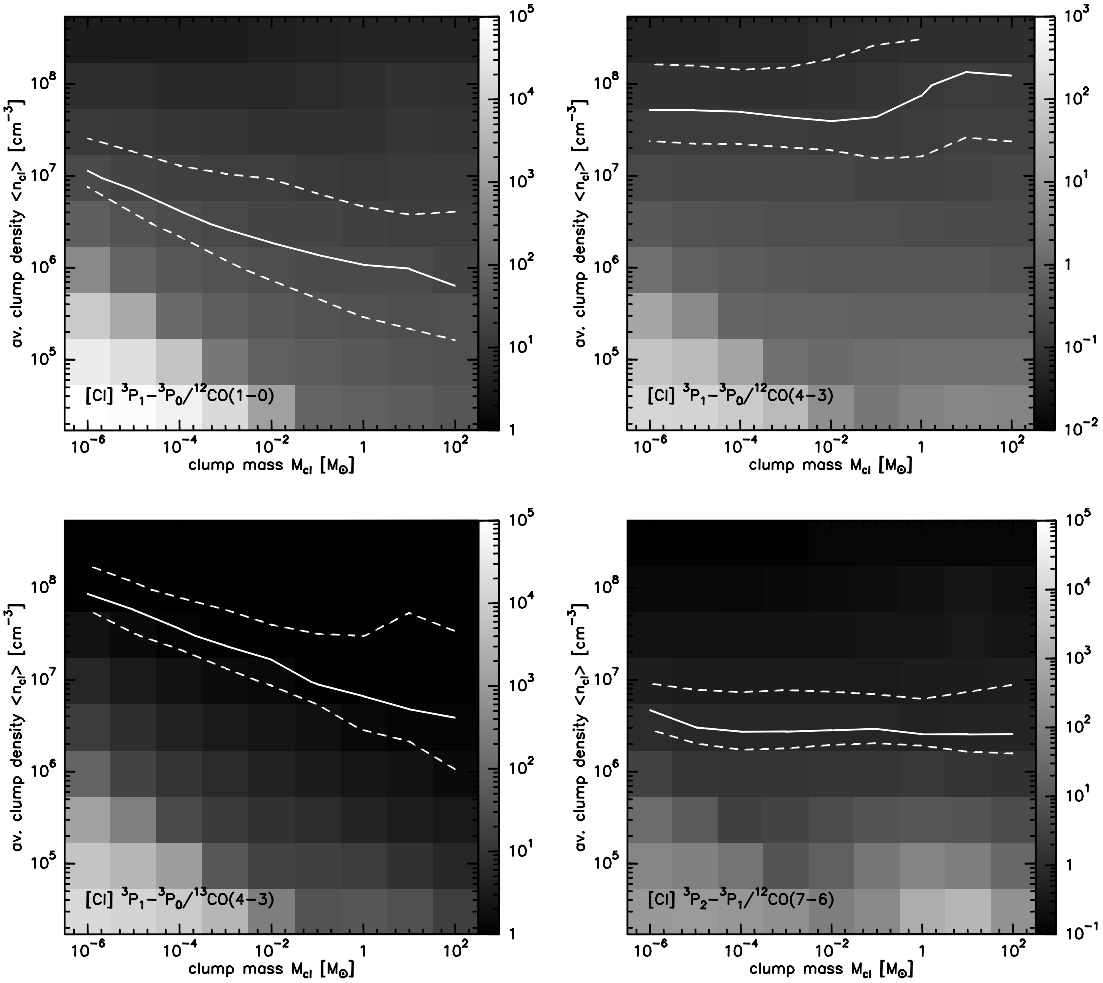

Fig. 5.40: *Model [C I] $^3P_1 \rightarrow {}^3P_0$/$^{12}CO$ $J = 4 \rightarrow 3$, $J = 1 \rightarrow 0$, [C I] $^3P_1 \rightarrow {}^3P_0$/$^{13}CO$ $J = 4 \rightarrow 3$, and [C I] $^3P_2 \rightarrow {}^3P_1$/$^{12}CO$ $J = 7 \rightarrow 6$ line-integrated intensity ratios. Solid contours represent the observed line ratios, while the dashed ones delimit a 40% error range.*

5.5 Discussion

5.5.1 High-density Gas in N159W

An CO excitation analysis made by Johansson et al. (1998) toward N159W suggest $T_{\rm kin} \simeq 20$ K, $N_{\rm CO} \simeq 10^{17}$ cm^{-2}, $n \simeq 10^{4.5}$ cm^{-3} with a filling factor between 0.7 and 1.0 at a scale of 11 pc. Using these parameters in the escape-probability code described in [See note **2** at the end of the draft], we obtain a value for the ^{12}CO $J = 4 \rightarrow 3$ peak temperature that is consistent with the observations ($T_{\rm mb} \simeq 11$ K). This peak temperature is also expected assuming LTE, optically thick emission, and $T_{\rm kin} \simeq 20$ K. These results set a lower limit to the gas density of $n \gtrsim 10^{4.5}$ cm^{-3}. If the density of $10^{4.5}$ cm^{-3} applies, this suggest that the ^{12}CO $J = 4 \rightarrow 3$ line is excited by line trapping, as its critical

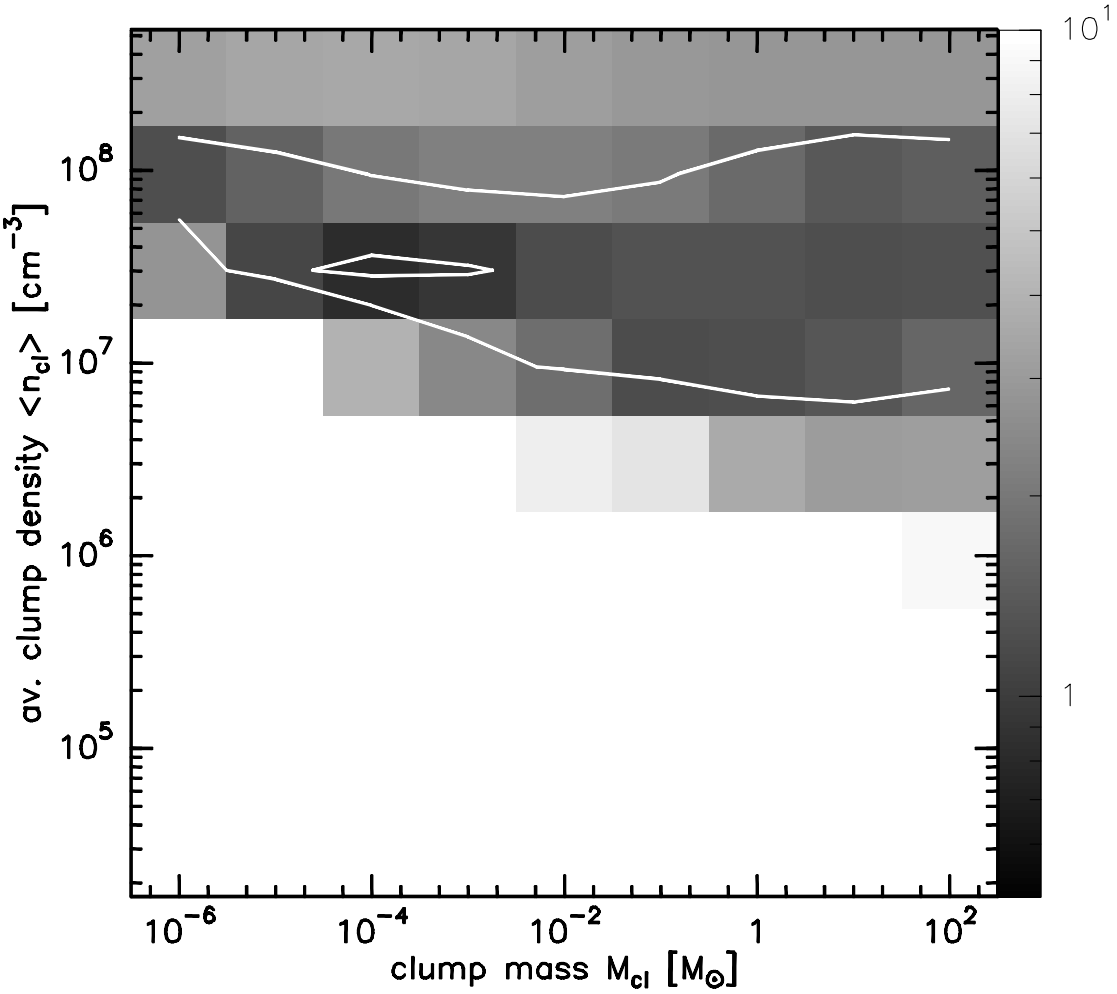

Fig. 5.41: *Reduced Q^2 resulting from the comparison between the observed [C I]/^{12}CO , [C I]/^{13}CO, and ^{12}CO $J = 4 \rightarrow 3$/ $J = 1 \rightarrow 0$ line-integrated intensity ratios toward N159W . The contours represent Q^2 =1 and 2.*

density is $n_{\rm crit} \simeq 10^5$ cm^{-3}. Other excitation analyses also suggest a low-temperature and high-density molecular gas in N159W (Bolatto et al., 2005; Minamidani et al., 2007) and in other regions of the LMC (N44; Kim et al., 2004). We note that a two-component model proposed by Bolatto et al. (2005) is not required to reproduce the observed low and mid-J CO emission.

High densities are also suggested by observations of molecular species like CS, SO, and H_2CO ($n = 10^5 - 10^6$ cm^{-3}; Heikkilä et al., 1999). Temperatures of about 20 K are suggested by observations of NH_3 (J. Ott; private communication).

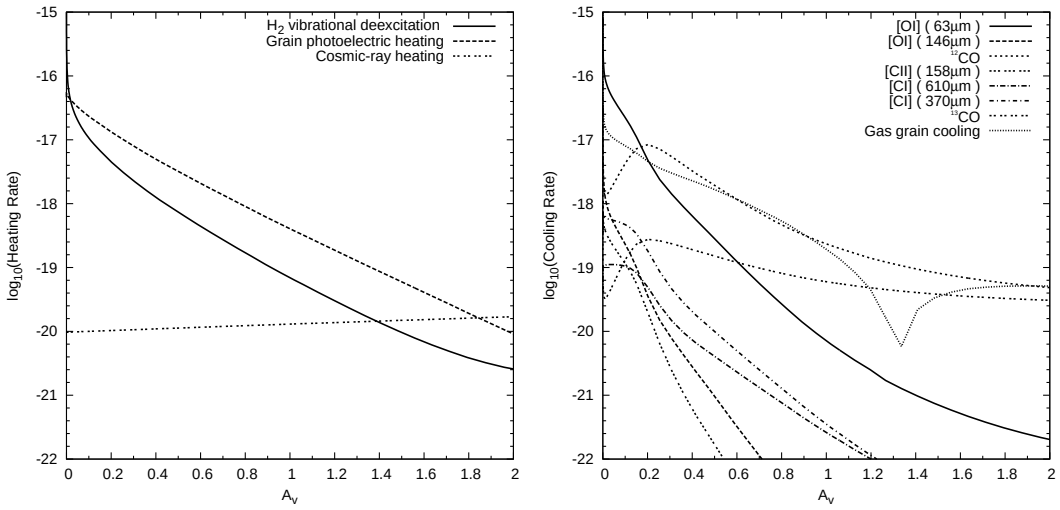

Fig. 5.42: *Dominant heating and cooling processes.The heating and cooling rates are in units of erg* s^{-1} cm^{-3}.

5.5.2 Heating and Cooling

Fig. 5.42 shows heating and cooling rates for different processes as a function of visual extinction A_v for a PDR model with $Q^2 \simeq 0.8$ ($M_{cl} = 10^{-4}\,M_\odot$ and $\langle n \rangle_{cl} = 10^{7.2}$ cm^{-3}; Sect. 4.4). The photoelectric effect on dust grains dominates the gas heating at the cloud surface followed by cosmic-ray heating, which becomes more important at larger depths. It is only at the edge of the cloud ($A_v < 0.1$) that H_2 vibrational deexcitation heating dominates over photoelectric heating. The gas cooling is mainly governed by the ^{12}CO rotational transitions and by gas-grain collisions, except at the cloud edge ($A_v < 0.2$) where the [O I] $^3P_1 \rightarrow ^3P_0$ fine structure transition dominates. Similar results have been obtained in models with high density by Röllig et al. (2006). Note that the [C II] transition does not dominate the cooling, even very close to the cloud surface. This can attributed to the presence of PAHs in the chemical network of our models, which enhance the charge transfer between PAH^- and C^+, hence reducing the abundance of C^+ (see Chapter 2).

5.6 Conclusions

In this chapter we have presented observations of the ^{12}CO $J = 4 \rightarrow 3$, $J = 7 \rightarrow 6$, and ^{13}CO $J = 4 \rightarrow 3$ rotational transitions as well as the [C I] $^3P_2 \rightarrow ^3P_1$ and $^3P_1 \rightarrow ^3P_0$ fine-structure transitions toward the N159W region in the LMC. The ^{12}CO $J = 7 \rightarrow 6$, ^{13}CO $J = 4 \rightarrow 3$, and [C I] $^3P_2 \rightarrow ^3P_1$ transitions were detected for the first time in the LMC (more details in Fukui et al., 2007). Combining this data with observations of the ^{12}CO $J = 1 \rightarrow 0$ line presented in Chapter 4, we study the properties of the

low-metallicity molecular gas in N159W using a PDR model. From this analysis we conclude:

- The models that best reproduce the observations suggest clump densities of $n \simeq 10^7$ cm^{-3} and masses M = $10^{-3} - 10^{-4}$ M$_\odot$.
- High densities are suggested by the strong ^{12}CO $J = 4 \rightarrow 3$ line. This line is consistent with LTE, optically thick emission and $T_{\rm kin} \simeq 20$ K. This sets a lower limit to the gas density of $n \gtrsim 10^5$ cm^{-3}, which is the critical density of the ^{12}CO $J = 4 \rightarrow 3$ transition.
- We find that the gas heating at the cloud surface is dominated by H_2 vibrational deexcitation and photoelectric heating. The cooling is dominated by the [O I] $^3P_1 \rightarrow ^3P_0$ fine structure transition at the cloud edge, followed by ^{12}CO and gas-grain collision which dominate at larger depths.

6 The influence of the FUV radiation field on the low-metallicity molecular gas.

In the following we study the impact of the FUV field on the line ratios between different transitions using a PDR model. The effects of metallicity in PDRs have been previously studied by Röllig et al. (2006).

Considering that the 30 Dor molecular ridge is an excellent laboratory to study the properties of the molecular gas in a low-metallicity environment (Chapter 3), we focus our study on this region. We assume that the clump density and mass are constant properties of the molecular gas along the molecular ridge. Thus, we assume a fixed clump mass and density, $M_{\rm cl} = 10^{-4}\,{\rm M}_{\odot}$ and $\langle n \rangle_{\rm cl} = 10^{7.2}$ cm^{-3}, respectively, as this is the model with the smallest Q^2 obtained in Sect. 5.4. We also consider a constant metallicity of $Z = 0.5\,{\rm Z}_{\rm solar}$ in this region (Westerlund, 1997).

We run models considering different strengths of the FUV radiation field. In Model #1 the model clump is exposed to the mean interstellar radiation field (χ_0; Draine, 1978). This might be the condition for clumps located far form the 30 Dor region. In case of Model #2 we consider a FUV radiation field of $176\,\chi_0$ as estimated by Israel et al. (1996) in the N159W region. We finally consider a model with $3500\,\chi_0$ (Model #3). This strength of the FUV field has been estimated toward 30 Dor (Werner et al., 1978; Poglitsch et al., 1995). A summary of the presented models is shown in Table 6.18.

Tables 6.19 and 6.20 show the line ratios between the fine structure transitions of [C I] and [C II] and the ^{12}CO and ^{13}CO rotational transitions. Larger differences are noticed between ratios in Model #1 and in Model #2. In case of the ratios involving [C I] the larger differences occur in those including [C I] $^3{\rm P}_2 \rightarrow ^3{\rm P}_1$ because this transition is more sensitive to the FUV radiation field compared to $^3{\rm P}_1 \rightarrow ^3{\rm P}_0$. In general ratios involving low$-J$ ^{12}CO and ^{13}CO transitions show larger changes as these transitions are less sensitive to χ. In case of the mid$-J$ ^{12}CO and ^{13}CO transitions, ratios in Model #2 tend to be more similar to, or smaller than, those in Model #1. For higher FUV radiation fields (Model #2 and #3) line ratios involving [C I] are rather insensitive to χ with only differences of a factor of about 2 for the two lowest ^{12}CO and ^{13}CO transitions.

In case of the [C II]/^{12}CO and [C II]/^{13}CO line ratios we can see differences of several orders of magnitude between Model #1 and #2. This is because [C II] is very sensitive to the FUV radiation field and can be very weak in the regime of low-FUV radiation fields (see Chapter 2). Larger changes are also noticed between Model #2 and #3, especially for line ratios involving low$-J$ ^{12}CO and ^{13}CO transitions, with differences by a factor between 10 to 60. In case of the [C II]/ [C I] line ratios, that involving the $^3{\rm P}_1 \rightarrow ^3{\rm P}_0$ is the most sensitive (differences by a factor of $\sim$10 and $\sim$60 for the [C I] $^3{\rm P}_1 \rightarrow ^3{\rm P}_0$ and $^3{\rm P}_1 \rightarrow ^3{\rm P}_0$, respectively).

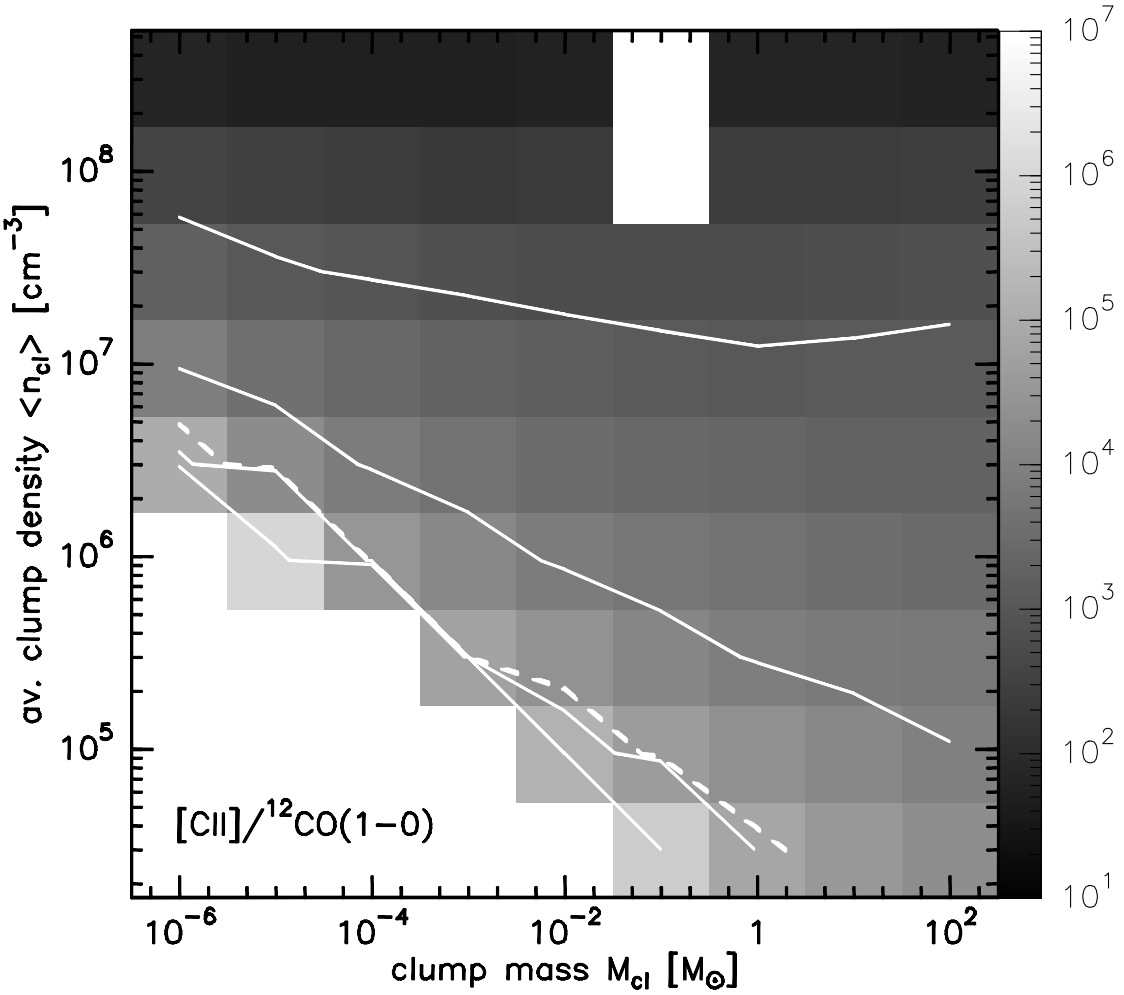

Fig. 6.43: *[C II]/^{12}CO $J = 1 \rightarrow 0$ line ratio calculated for a grid of models with χ =3500χ_0. Solid contour lines correspond to $10^3, 10^4, 10^5$, and 10^6. The dashed contour denotes the value obtained by Poglitsch et al. (1995) toward 30 Dor (6×10^4).*

Comparing the [C II]/^{12}CO $J = 1 \rightarrow 0$ line ratios obtained in Model #3 with that observed toward 30 Dor (6.9×10^4; Poglitsch et al., 1995), we notice that its value is lower by a factor of ~80. This can be due to the assumption of constant clump density and mass throughout the 30 Dor molecular ridge. In the following we study the

Tab. 6.18: *PDR models*

Model #	FUV field χ_0	Metallicity Z_{solar}	Density $\log(\langle n \rangle_{cl})$	Mass M_{cl}
1	1.0	0.5	7.2	10^{-4}
2	176	0.5	7.2	10^{-4}
3	3500	0.5	7.2	10^{-4}

Tab. 6.19: *[C I]/^{12}CO and [C I]/^{13}CO line-integrated intensity ratios.*

Line Ratio	Model #1	Model #2	Model #3
[C I] $^3P_2 \rightarrow ^3P_1$ / $^3P_1 \rightarrow ^3P_0$	0.54	4.33	6.32
[C I] $^3P_2 \rightarrow ^3P_1$/ ^{12}CO			
$J = 1 \rightarrow 0$	0.35	45.4	84.8
$J = 2 \rightarrow 1$	0.05	4.61	7.85
$J = 3 \rightarrow 2$	0.02	1.35	2.11
$J = 4 \rightarrow 3$	0.01	0.62	0.87
$J = 5 \rightarrow 4$	0.02	0.37	0.46
$J = 6 \rightarrow 5$	0.09	0.27	0.29
$J = 7 \rightarrow 6$	0.79	0.24	0.21
[C I] $^3P_2 \rightarrow ^3P_1$/ ^{13}CO			
$J = 1 \rightarrow 0$	1.37	267	708
$J = 2 \rightarrow 1$	0.21	26.2	53.0
$J = 3 \rightarrow 2$	0.13	8.13	13.2
$J = 4 \rightarrow 3$	0.22	4.58	5.86
[C I] $^3P_1 \rightarrow ^3P_0$/ ^{12}CO			
$J = 1 \rightarrow 0$	0.65	10.4	13.4
$J = 2 \rightarrow 1$	0.09	1.06	1.24
$J = 3 \rightarrow 2$	0.03	0.31	0.33
$J = 4 \rightarrow 3$	0.02	0.14	0.13
$J = 5 \rightarrow 4$	0.04	0.08	0.07
$J = 6 \rightarrow 5$	0.17	0.06	0.04
$J = 7 \rightarrow 6$	1.46	0.05	0.03
[C I] $^3P_1 \rightarrow ^3P_0$/ ^{13}CO			
$J = 1 \rightarrow 0$	2.52	61.7	112
$J = 2 \rightarrow 1$	0.39	6.05	8.38
$J = 3 \rightarrow 2$	0.23	1.87	2.09
$J = 4 \rightarrow 3$	0.41	1.05	0.92

effect of these parameters on the [C II]/^{12}CO $J = 1 \rightarrow 0$ line ratio. Fig. 6.43 shows the [C II]/^{12}CO $J = 1 \rightarrow 0$ line ratio of a grid of models with different clump density and mass but with the same FUV radiation field of 3500 χ_0. As we can see this line ratio strongly depends on the clump density and to a minor degree on the clump mass. The lower the clump density the larger the penetration of FUV photons into the molecular gas. This produces a larger C^+/C/CO transition layer and therefore increases the abundance of C^+ on the clump surface which, together with the larger gas temperatures at the cloud surface, increases the intensity of the [C II] line. This produces a larger [C II]/^{12}CO $J = 1 \rightarrow 0$ line ratio. The latter argument suggest that the clump density

toward 30 Dor is lower compared to that in N159W. Lower densities in 30 Dor have been suggested by multi-line study carried out by Poglitsch et al. (1995) ($n = 10^4 - 10^5$ cm^{-3}).

Tab. 6.20: *[C II]/^{12}CO and [C II]/^{13}CO line-integrated intensity ratios.*

Line Ratio	Model #1	Model #2	Model #3
[C II] $^2P_{3/2} \rightarrow ^2P_{1/2}$/ [C I]			
$^3P_2 \rightarrow ^3P_1$	5.7×10^{-4}	0.33	10
$^3P_1 \rightarrow ^3P_0$	3.1×10^{-4}	1.45	63.3
[C II] $^2P_{3/2} \rightarrow ^2P_{1/2}$/ ^{12}CO			
$J = 1 \rightarrow 0$	2.0×10^{-4}	15.2	850
$J = 2 \rightarrow 1$	2.8×10^{-5}	1.54	78.7
$J = 3 \rightarrow 2$	1.2×10^{-5}	0.45	21.1
$J = 4 \rightarrow 3$	9.0×10^{-6}	0.20	8.8
$J = 5 \rightarrow 4$	1.2×10^{-5}	0.12	4.68
$J = 6 \rightarrow 5$	5.4×10^{-5}	0.09	2.95
$J = 7 \rightarrow 6$	4.5×10^{-4}	0.08	2.12
[C II] $^2P_{3/2} \rightarrow ^2P_{1/2}$/ ^{13}CO			
$J = 1 \rightarrow 0$	7.8×10^{-4}	89.6	7104
$J = 2 \rightarrow 1$	1.2×10^{-4}	8.79	531
$J = 3 \rightarrow 2$	7.4×10^{-5}	2.72	132
$J = 4 \rightarrow 3$	1.2×10^{-4}	1.53	58.8

7 Summary and Future Prospects

In the present thesis we have studied the properties of the low-metallicity molecular gas in different regimes of the far-ultraviolet radiation field. We approach this problem by studying the molecular gas in the context of photon-dominated regions (PDRs). For that we use the PDR model developed by Störzer et al. (1996) (KOSMA$-\tau$) to provide a self-consistent solution of the thermal balance and chemistry of the molecular gas. This model assumes an isotropically irradiated spherical cloud.

In order to model the emission emerging from PDRs, models need to assume abundances of elements, cloud morphology, a density structure, and they also also need to approximate physical processes related with the cloud heating and cooling. Any variation of these assumptions and approximations can lead to very different results (Röllig et al., 2007). Barnard 68 (Chapter 2) with its roughly spherical geometry and well constrained density profile (Alves et al., 2001) is an ideal test case for spherically symmetric PDR models. We have compared observations of the three lowest rotational transitions of ^{12}CO, ^{13}CO $J = 3 \rightarrow 2$, $J = 2 \rightarrow 1$, and the [C I] $^3P_1 \rightarrow ^3P_0$ transition with the PDR model in unprecedented detail. We tested the impact of including PAHs in the chemical network of the model, reducing the FUV radiation field, and considering the effects of depletion in the emerging model line intensity. We find difficulties to simultaneously explain the observed ^{12}CO and ^{13}CO emission. We find that the low FUV field proposed by Bergin et al. (2006) trying to explain the weak ^{13}CO emission is incompatible with observations of ^{12}CO and [C I]. Including PAHs in the chemical network of the model has the effect of increasing the C^0 layer while the C^+ layer is very thin, making the [C II] emission very faint and difficult to distinguish from the emission from the ambient Warm Ionized Medium (WIM). Depletion is not likely to play an important role for the observed transitions.

With a better understanding of the chemistry in the weak FUV regime, we study the low-metallicity gas present in two intermediate velocity clouds (IVCs; Chapter 3). IVCs are thought to be located in the interface between the galactic halo and the galactic diskin which they seem to be falling. Analyzing global properties obtained from CO observations we find that the observed IVCs have low molecular masses ($M \simeq 10^{-3} M_\odot$). An excitation analysis of the ^{12}CO and ^{13}CO emission suggests excitation temperatures of $T_{ex} \simeq 12$ K, total CO column densities of $N_{CO} \simeq 10^{16} - 10^{17}$ cm^{-2} and gas densities between $10^3 - 10^4$ cm^{-3}. We also find that the ^{12}CO $J = 2 \rightarrow 1$ and ^{12}CO $J = 1 \rightarrow 0$ transitions are consistent with LTE, while the ^{12}CO $J = 3 \rightarrow 2$ is probably affected by sub-thermal excitation or optical depth effects. We analyze the ^{12}CO and ^{13}CO observations together with the [C I] emission observed toward IVC210 using a PDR model. We find that in order to match the observed line ratios, a spherical clump surrounded by a layer of small column density H_2 is required (pre-shielding). We also find that the C I/CO line-integrated intensity ratios are not significantly affected by the metallicity when the molecular gas is exposed to weak far-ultraviolet radiation fields.

The results of this study suggest that IVCs are similar to translucent clouds in the low CO column density regime.

In Chapter 4 we study whether the global properties of the molecular gas is affected by the low metallicity and by the strongly varying far-ultraviolet radiation field in the LMC. To this end we have performed a large-scale ^{12}CO J= 1 → 0 survey of the 30 Dor molecular ridge in this galaxy. The observations were analyzed using a clump-decomposition algorithm (GAUSSCLUMPS). We find that the average CO-to-H_2 conversion factor of our survey, $X_{CO} = (1.2 \pm 0.04) \times 10^{20}$ cm^{-2} (K km s^{-1})$^{-1}$), is consistent with that found in our Galaxy. We also find that X_{CO} is larger for molecular clouds in the immediate surrounding of the 30 Dor region where they are exposed to extreme FUV radiation fields. The higher value of X_{CO} is related to an increase of the velocity dispersion in the 30 Dor and N159 regions compared with regions further south, and to a decrease of the brightness temperature of clumps in the 30 Dor region. Effects of beam filling decrease the observed clump brightness temperature, while turbulence associated with newly formed stars increases the velocity dispersion. Comparing with previous determinations of X_{CO}, we notice that it decreases with decreasing linear scale of the observations, suggesting that the scale of the observations is important in the determination of molecular masses of distant galaxies. The empirical relations between observed clump parameters are similar to those found in Galactic clouds. The degree of virialization of the clumps shows only small variations along the molecular ridge. Clumps in the 30 Dor region show lower CO luminosities compared to clouds further south with similar velocity dispersions and larger virial masses compared to clumps with similar luminosities. The clump-mass spectrum of molecular clouds is similar to that found in the Galaxy. We do not find any significant difference in the clump-mass spectrum between regions in the molecular ridge. From these results we conclude that the global properties of the low-metallicity molecular gas are similar to those found in our Galaxy and that changes in local properties of the gas can only be noticed in the case of an extreme FUV radiation field as present in the 30 Dor region.

In Chapter 5 we have presented observations of the ^{12}CO $J = 1 \rightarrow 0$, $J = 4 \rightarrow 3$, $J = 7 \rightarrow 6$, and ^{13}CO $J = 4 \rightarrow 3$ rotational transitions as well as the [C I] $^3P_2 \rightarrow ^3P_1$ and $^3P_1 \rightarrow ^3P_0$ fine-structure transitions toward the N159W region in the LMC. The observations of the ^{12}CO $J = 7 \rightarrow 6$, ^{13}CO $J = 4 \rightarrow 3$, and [C I] $^3P_2 \rightarrow ^3P_1$ transitions are first detections in the LMC and are presented by Fukui et al. (2007). We compare a PDR model with the observed line ratios in order to study the properties of the low-metallicity molecular gas in N159W. We find that clumps with masses between $M = 10^{-3} - 10^{-4}$ M$_\odot$ and high densities, $n \simeq 10^7$ cm^{-3}, are required to explain the line emission. The ^{12}CO $J = 4 \rightarrow 3$ line is consistent with LTE, optically thick emission and $T_{kin} \simeq 20$ K. The gas heating at the cloud surface is dominated by H_2 vibrational de-excitation and photoelectric heating. The cooling is dominated by the [O I] $^3P_1 \rightarrow ^3P_0$ fine structure transition at the cloud edge followed by ^{12}CO and gas-grain collisions which dominate at larger depths.

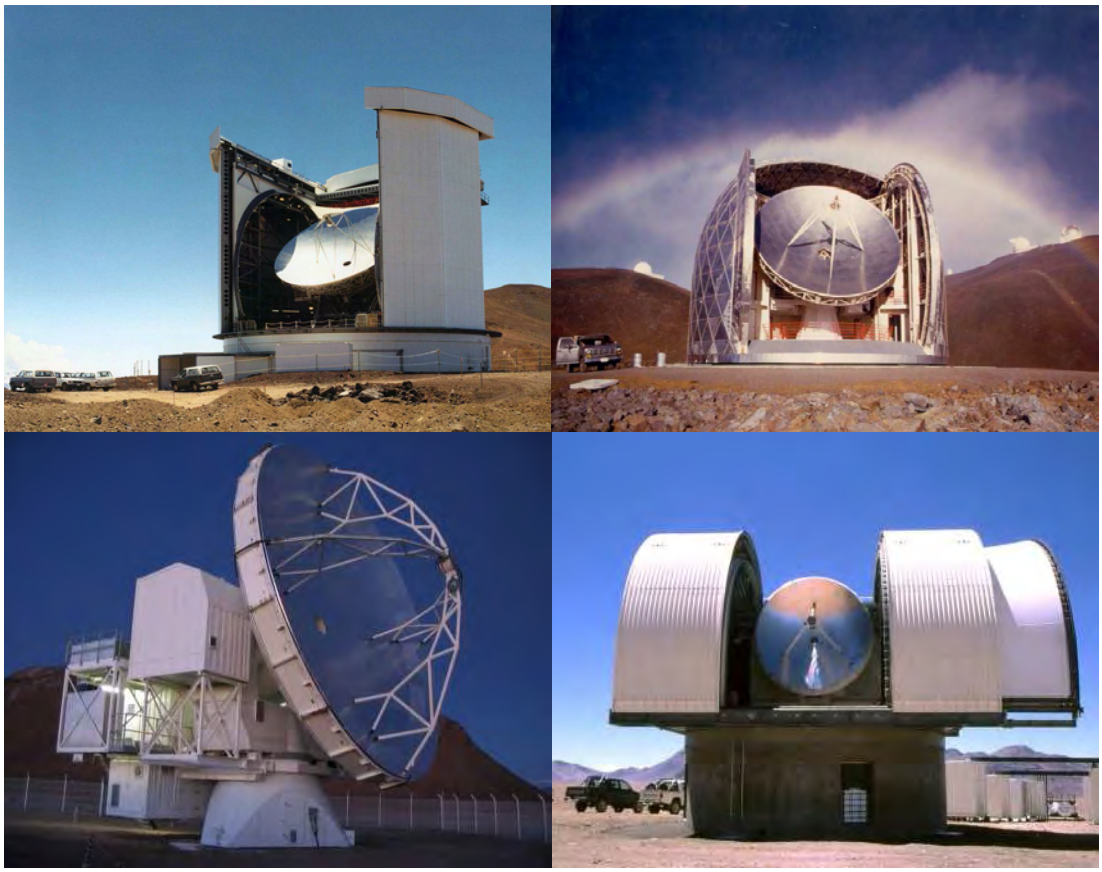

Fig. 7.44: *Upper left: The James Clerk Maxwell Telescope (JCMT), upper right Caltech Sub-millimeter Observatory (CSO), Lower left: Atacama Pathfinder Experiment (APEX), and Lower right: NANTEN2.*

We finally study the variations with the FUV radiation field of the line ratios involving [C II], [C I], ^{12}CO, and ^{13}CO (Chapter 6). For this end we consider the conditions found in the 30 Dor molecular ridge in the LMC. The most sensitive line ratios are those relating [C II] and [C I] to low–J ^{12}CO and ^{13}CO transitions. We also find that in order to explain the observed [C II]/^{12}CO $J = 1 \rightarrow 0$ ratio observed toward 30 Dor we need a lower gas density compared with that estimated in N159W.

Future observations will be useful to test our results and assess the importance of different parameters used in our PDR models. This will take advantage of the current (e.g. JCMT, CSO), new (e.g. APEX, NANTEN2; Fig. 7.44) and future (SOFIA, Herschel; Fig. 7.45) telescopes. Due to their high critical densities, observations of the ^{12}CO $J = 4 \rightarrow 3$ and $J = 5 \rightarrow 4$ rotational transitions can be used to distinguish between models with or without pre-shielding. Models with pre-shielding predict lower densities and, as a consequence, weaker ^{12}CO $J = 4 \rightarrow 3$ and $J = 5 \rightarrow 4$ emission compared to models without pre-shielding.

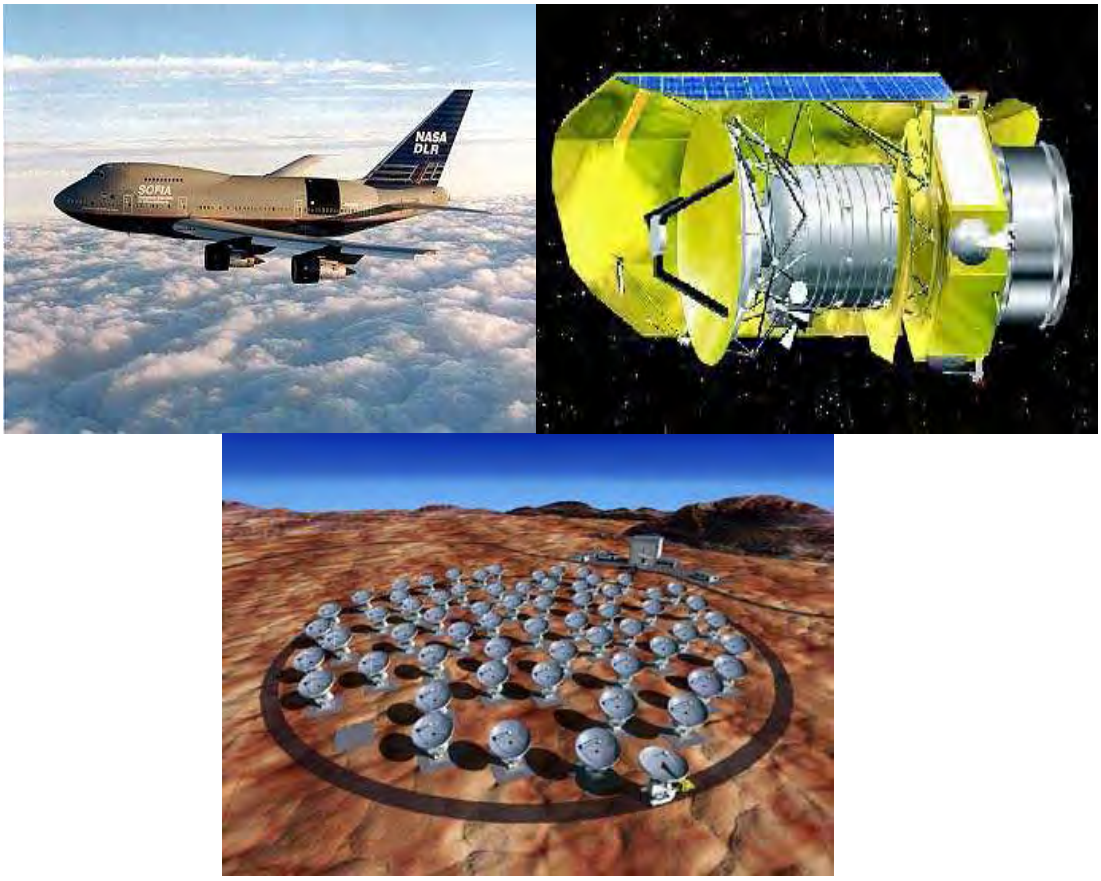

Fig. 7.45: *Upper left: The Stratospheric Observatory for Infrared Astronomy (SOFIA), Upper right: the Herschel satellite. Lower panel: Atacama Large Millimetric Array (ALMA).*

SOFIA and Herschel will facilitate observations of lines located in the Terahertz regime of the electromagnetic spectrum such as the [C II] and [O I] fine structure transitions. The [C II] emission is important in order to assess the importance of metallicity in the PDR models. This is because in low-metallicity PDRs the CO layer is reduced due to the enhanced CO photodissociation while the C^+ layer is increased. This should be reflected in the [C II]/^{12}CO line ratios. The emission from this line is expected to be very faint in PDRs exposed to weak FUV radiation fields as a result of the inclusion of PAHs in the chemical network. Velocity-resolved observations of this transition are required to distinguish its emission from that emerging from the ambient WIM. Observations of [O I] $^3P_1 \rightarrow ^3P_0$ will be used to test the results suggesting that this transition dominates the gas cooling at the cloud surface in the low-metallicity, strong FUV field case.

The study of the properties of the low-metallicity gas exposed to different regimes of the FUV radiation field is crucial in order to understand the processes of star formation in the early universe. A better knowledge of these conditions in the local universe will

serve as a template for future studies of the ISM in high-redshift galaxies using ALMA (Fig. 7.45). These studies will also benefit from a better understanding of the nature of the sub-millimeter and terahertz emission since these transitions are redshifted to more favorable atmospheric windows and therefore they will be easier to observe even from the ground. Having a comprehensive picture of the physics and chemistry of the local or high-redshifted molecular gas will give us insights into the way galaxies evolve and into the nature of our universe.

A Heating and Cooling processes

In the following, we describe the main heating and cooling processes used in our models. The model also includes H_2 heating (dissociation, collisional de-excitation of vibrational levels, photo-dissociation and formation of H_2), cooling due to recombination of electrons in dust grains as well as radiative cooling.

A.1 Photo-electric Heating

Heating by the photo-electric effect in dust grains is one of the principal contributors to the gas heating in dense PDRs. Bakes & Tielens (1994) made theoretical calculations of the photo-electric heating efficiency, ϵ, for a given grain size distribution of PAHs and small grains, including the effects of grain charging. These calculations are fitted by

$$\epsilon = \frac{4.87\times10^{-2}}{[1+4\times10^{-3}(G_0T^{1/2}/n_e)^{0.73}]} + \frac{3.65\times10^{-2}(T/10^4)^{0.7}}{[1+2\times10^{-4}(G_0T^{1/2}/n_e)]} \tag{A.17}$$

for gas temperatures up to $T = 10^4$ K. Here G_0 is the mean interstellar radiation field (1.3×10^{-4}ergs^{-1}cm^{-2}sr^{-1}; Habing, 1968) and n_e is the electron density in cm^{-3}.

The total photo-electric heating rate, in terms of the efficiency ϵ is given by

$$\Gamma_{\rm pe} = 10^{-24}\epsilon G_0 n_{\rm H} \quad {\rm ergs\,s^{-1}cm^{-3}}, \tag{A.18}$$

where $n_{\rm H}$ is the density of H atoms in units of cm^{-3}. About half of the gas heating by the photo-electric process is due to grains with sizes less than 15Å ($N_{\rm C} \simeq 1500$ C atoms), while the other half is due to grains of sizes between 15 and 100Å ($1500 < N_{\rm C} < 5\times10^5$ C atoms). The contribution of larger grains is negligible.

A.2 Gas-Grain Collisions

Gas and dust can exchange energy through the difference in their temperatures. The heating rate due to gas-grain collisions is given by (Tielens & Hollenbach (1985), Eq. A19)

$$\Gamma_{\rm gg} = 3.5\times10^{-34} n_{\rm H}\delta_{\rm dust}T_{\rm gas}^{0.5}(T_{\rm dust}-T_{\rm gas}) \quad {\rm ergs\,s^{-1}cm^{-3}}, \tag{A.19}$$

where $\delta_{\rm dust}$ is the ratio of the dust abundance to that in the diffuse interstellar medium, $n_{\rm H}$ the density of H atoms in units of cm^{-3}, $T_{\rm gas}$ the gas temperature in K, and $T_{\rm dust}$ the dust temperature in K. For the physical conditions of our models, $T_{\rm gas} > T_{\rm dust}$; therefore, gas-grain collisions reflect a cooling process.

A.3 Cosmic-Ray Heating

Cosmic rays can efficiently ionize and heat the gas. This heating mechanism dominates in regions with higher visual extinction. In a cloud, a high-energy cosmic-ray can ionize an atom producing an energetic electron. This primary electron can later transfer energy to free electrons (inelastic collisions) or to other atoms and molecules (ionization and excitation). The cosmic-ray heating rate depends on the cosmic-ray ionization rate (s^{-1}) of molecular hydrogen ,ζ, and is given by (Wolfire et al., 1995)

$$\Gamma_{\rm CR} = n_{\rm H}\zeta E_h(E,\chi_e) \quad {\rm ergs\,s^{-1}cm^{-3}}, \tag{A.20}$$

where $E_h(E, x_e)$ is the average heat deposited by a primary electron with energy E and an electron fraction χ_e and $n_{\rm H}$ the density of H atoms in units of cm^{-3}. For a value of E_h = 7.6 eV, the cosmic-ray heating rate results in

$$\Gamma_{\rm CR} = 1.22\times10^{-11} n_{\rm H}\zeta \quad {\rm ergs\,s^{-1}cm^{-3}}, \tag{A.21}$$

In our models, we assume a cosmic-ray ionization rate of $\zeta = 5{\times}10^{-11}s^{-1}$ (Röllig et al., 2006).

B Acknowledgments

I would like to thank my advisors Uli Klein and Frank Bensch for their constant support and advise. I appreciate very much their patience and willingness to reply to all my questions. I thank them for giving me the inspiration and the ideas that lead me to write this thesis. I also thank their corrections and suggestions concerning this thesis.

Special thanks to Christina Stein-Schmitz for all the help regarding my adaptation to a new country. Without her constant help and advise I would not be able to "survive" in Germany.

I thank to all members of the radioastronomy division of the Argelander Institut für Astronomie giving a very friendly and inspiring working atmosphere. I thank Phillipp Müller for letting me to use the tools from the institute's electronics laboraroty to solve my "technical" problems.

I thank my collaborators Jürgen Ott, Tony Wong, Erik Muller, and Annie Hughes for helping me during the observations in the Mopra 22-m telescope and for the fruitful scientific discussions regarding the work done in Chapter 3. Special thanks to Jürgen Ott for his constant support and willingness to reply to my questions.

I thank to all the friends I made in Bonn for giving me the opportunity to spend a great time during my PhD.

I finally would like to thank the support from my family. Although they are far away, I always feel that they are with me.

I acknowledge the financial support from the International Max Planck Research School (IMPRS) for German courses. I thank all the German members of Argelander Institut für Astronomie that answered all my questions about the German language.

The first half of my PhD was supported through a stipend from the International Max Planck Research School (IMPRS) for Radio and Infrared Astronomy at the University of Bonn and Cologne.

The second half of my PhD was supported by the Deutsche Forschungsgemeinschaft, DFG via Grant SFB 494.

C Curriculum Vitae

Curriculum Vitae

Name:	Jorge Luis Pineda Gálvez
Address:	Kessenicher Strasse 74 53129 Bonn
Nationality:	Chilean
Date of Birth:	15 March 1979
Marital Status:	Single
Education:	
Mar. 1984 – Nov 1996	Colegio Salesiano Manuel Arriarán Barros Santiago, Chile Primary and Secondary School.
Mar. 1998 – Nov. 2002	University of Chile Santiago, Chile B.S. in Physics and Astronomy
Mar. 2002 – Oct. 2003	University of Chile Santiago, Chile M.S. in Astronomy
Jan. 2004 – Mar. 2007	Angelander Institut fuer Astronomie (University of Bonn) and Max Planck Institute fuer Radioastronomie Bonn, Germany Ph.D. in Astronomy
Interests:	Yoga.

References

Allen, C. W. 1973, Astrophysical quantities (London: University of London, Athlone Press, |c1973, 3rd ed.)

Alves, J. F., Lada, C. J., & Lada, E. A. 2001, Nature, 409, 159

Appenzeller, I., Lequeux, J., Silk, J., Maeder, A., & Martinet, L. 1980, Star formation : tenth advanced course of the Swiss Society of Astronomy and Astrophysics (member society of the Swiss National Academy of Science) (Sauverny, Switzerland : Geneva Observatory, 1980.)

Arimoto, N., Sofue, Y., & Tsujimoto, T. 1996, PASJ, 48, 275

Bakes, E. L. O. & Tielens, A. G. G. M. 1994, ApJ, 427, 822

Bakes, E. L. O. & Tielens, A. G. G. M. 1998, ApJ, 499, 258

Bekki, K. & Chiba, M. 2005, MNRAS, 356, 680

Bell, T. A., Roueff, E., Viti, S., & Williams, D. A. 2006, MNRAS, 371, 1865

Bensch, F. 2006, A&A, 448, 1043

Bensch, F., Leuenhagen, U., Stutzki, J., & Schieder, R. 2003, ApJ, 591, 1013

Bergin, E. A., Maret, S., van der Tak, F. F. S., et al. 2006, ApJ, 645, 369

Bergin, E. A. & Snell, R. L. 2002, ApJ, 581, L105

Black, J. H. & van Dishoeck, E. F. 1987, ApJ, 322, 412

Bloemen, J. B. G. M., Strong, A. W., Mayer-Hasselwander, H. A., et al. 1986, A&A, 154, 25

Boisse, P. 1990, A&A, 228, 483

Bolatto, A. D., Israel, F. P., & Martin, C. L. 2005, ApJ, 633, 210

Bolatto, A. D., Jackson, J. M., Israel, F. P., Zhang, X., & Kim, S. 2000, ApJ, 545, 234

Bolatto, A. D., Leroy, A., Israel, F. P., & Jackson, J. M. 2003, ApJ, 595, 167

Booth, R. S. 1993, in LNP Vol. 416: New Aspects of Magellanic Cloud Research, ed. B. Baschek, G. Klare, & J. Lequeux, 26–35

Bourke, T. L., Hyland, A. R., Robinson, G., James, S. D., & Wright, C. M. 1995, MNRAS, 276, 1067

Burns, C. R., Tycner, C., McClure, M., et al. 2003, AJ, 125, 2584

Chieze, J. P. 1987, A&A, 171, 225

Cohen, R. S., Dame, T. M., Garay, G., et al. 1988, ApJ, 331, L95

Corneliussen, U. 1996, Ph.D. Thesis, University of Cologne

Dame, T. M., Elmegreen, B. G., Cohen, R. S., & Thaddeus, P. 1986, ApJ, 305, 892

de Boer, K. S., Braun, J. M., Vallenari, A., & Mebold, U. 1998, A&A, 329, L49

de Geus, E. J., de Zeeuw, P. T., & Lub, J. 1989, A&A, 216, 44

Desert, F.-X., Bazell, D., & Blitz, L. 1990, ApJ, 355, L51

Desert, F. X., Bazell, D., & Boulanger, F. 1988, ApJ, 334, 815

Dettmar, R.-J. & Heithausen, A. 1989, ApJ, 344, L61

Di Francesco, J., Hogerheijde, M. R., Welch, W. J., & Bergin, E. A. 2002, AJ, 124, 2749

Dickel, J. R., McIntyre, V. J., Gruendl, R. A., & Milne, D. K. 2005, AJ, 129, 790

Dickman, R. L. 1978, ApJS, 37, 407

Digel, S. W., Aprile, E., Hunter, S. D., Mukherjee, R., & Xu, F. 1999, ApJ, 520, 196

Digel, S. W., Grenier, I. A., Heithausen, A., Hunter, S. D., & Thaddeus, P. 1996, ApJ, 463, 609

Draine, B. T. 1978, ApJS, 36, 595

Draine, B. T. & Sutin, B. 1987, ApJ, 320, 803

Elmegreen, B. G. 1989, ApJ, 338, 178

Elmegreen, B. G. & Falgarone, E. 1996, ApJ, 471, 816

Evans, II, N. J. 1999, ARA&A, 37, 311

Evans, II, N. J., Davis, J. H., Mundy, L. G., & Van den Bout, P. 1987, ApJ, 312, 344

Feast, M. 1999, PASP, 111, 775

Fukui, Y., Mizuno, N., Yamaguchi, R., Mizuno, A., & Onishi, T. 2001, PASJ, 53, L41

Fukui, Y., Mizuno, N., Yamaguchi, R., et al. 1999, PASJ, 51, 745

Fukui, Y., Pineda, J. L., & Stutzki, J. 2007, PASP, 480, L59

Garay, G., Rubio, M., Ramirez, S., Johansson, L. E. B., & Thaddeus, P. 1993, A&A, 274, 743

Gaustad, J. E., McCullough, P. R., Rosing, W., & Van Buren, D. 2001, PASP, 113, 1326

Gierens, K. M., Stutzki, J., & Winnewisser, G. 1992, A&A, 259, 271

Gladders, M. D., Clarke, T. E., Burns, C. R., et al. 1999, in ASP Conf. Ser. 166: Stromlo Workshop on High-Velocity Clouds, ed. B. K. Gibson & M. E. Putman, 45

Graf, U. U., Heyminck, S., Michael, E. A., et al. 2003, in Millimeter and Submillimeter Detectors for Astronomy. Edited by Phillips, Thomas G.; Zmuidzinas, Jonas. Proceedings of the SPIE, Volume 4855, pp. 322-329 (2003)., ed. T. G. Phillips & J. Zmuidzinas, 322–329

Habing, H. J. 1968, Bull. Astron. Inst. Netherlands, 19, 421

Heikkilä, A., Johansson, L. E. B., & Olofsson, H. 1999, A&A, 344, 817

Heiles, C. & Habing, H. J. 1974, A&AS, 14, 1

Heiles, C., Reach, W. T., & Koo, B.-C. 1988, ApJ, 332, 313

Heithausen, A., Bensch, F., Stutzki, J., Falgarone, E., & Panis, J. F. 1998, A&A, 331, L65

Heithausen, A., Weiß, A., Kerp, J., & Fritz, T. 2001, ApJ, 561, 238

Henize, K. G. 1956, ApJS, 2, 315

Heyer, M. H. & Terebey, S. 1998, ApJ, 502, 265

Ho, P. T. P. & Townes, C. H. 1983, ARA&A, 21, 239

Hollenbach, D. J. & Tielens, A. G. G. M. 1999, Reviews of Modern Physics, 71, 173

Hotzel, S., Harju, J., Juvela, M., Mattila, K., & Haikala, L. K. 2002, A&A, 391, 275

Howe, J. E., Jaffe, D. T., Genzel, R., & Stacey, G. J. 1991, ApJ, 373, 158

Hunter, S. D., Bertsch, D. L., Catelli, J. R., et al. 1997, ApJ, 481, 205

Israel, F. 2000, in Molecular hydrogen in space, Cambridge, UK: Cambridge University Press, 2001. xix, 326 p.. Cambridge contemporary astrophysics. Edited by F. Combes, and G. Pineau des Forêts. ISBN 0521782244, p.293, ed. F. Combes & G. Pineau Des Forets, 293

Israel, F. P. 1988, in Millimetre and Submillimetre Astronomy, ed. R. D. Wolstencroft & W. B. Burton, 281–305

Israel, F. P. 1997, A&A, 328, 471

Israel, F. P., de Graauw, T., van de Stadt, H., & de Vries, C. P. 1986, ApJ, 303, 186

Israel, F. P., Johansson, L. E. B., Lequeux, J., et al. 1993, A&A, 276, 25

Israel, F. P., Maloney, P. R., Geis, N., et al. 1996, ApJ, 465, 738

Johansson, L. E. B. 1991, in IAU Symp. 146: Dynamics of Galaxies and Their Molecular Cloud Distributions, ed. F. Combes & F. Casoli, 1

Johansson, L. E. B., Greve, A., Booth, R. S., et al. 1998, A&A, 331, 857

Johansson, L. E. B., Olofsson, H., Hjalmarson, A., Gredel, R., & Black, J. H. 1994, A&A, 291, 89

Johnstone, D., Fich, M., Mitchell, G. F., & Moriarty-Schieven, G. 2001, ApJ, 559, 307

Johnstone, D., Wilson, C. D., Moriarty-Schieven, G., et al. 2000, ApJ, 545, 327

Kaufman, M. J., Wolfire, M. G., Hollenbach, D. J., & Luhman, M. L. 1999, ApJ, 527, 795

Kennicutt, Jr., R. C. 1998, ARA&A, 36, 189

Kim, S., Staveley-Smith, L., Dopita, M. A., et al. 1998, ApJ, 503, 674

Kim, S., Walsh, W., & Xiao, K. 2004, ApJ, 616, 865

Kramer, C., Stutzki, J., Rohrig, R., & Corneliussen, U. 1998, A&A, 329, 249

Kuntz, K. D. & Danly, L. 1996, ApJ, 457, 703

Kutner, M. L., Rubio, M., Booth, R. S., et al. 1997, A&AS, 122, 255

Ladd, N., Purcell, C., Wong, T., & Robertson, S. 2005, Publications of the Astronomical Society of Australia, 22, 62

Larson, R. B. 1981, MNRAS, 194, 809

Le Bourlot, J., Pineau Des Forets, G., Roueff, E., & Flower, D. R. 1993, A&A, 267, 233

Lepp, S. & Dalgarno, A. 1988, ApJ, 324, 553

Lequeux, J., Le Bourlot, J., Des Forets, G. P., et al. 1994, A&A, 292, 371

Lisenfeld, U. & Ferrara, A. 1998, ApJ, 496, 145

MacLaren, I., Richardson, K. M., & Wolfendale, A. W. 1988, ApJ, 333, 821

Maloney, P. 1990, in ASSL Vol. 161: The Interstellar Medium in Galaxies, ed. H. A. Thronson, Jr. & J. M. Shull, 493–523

Maloney, P. & Black, J. H. 1988, ApJ, 325, 389

Mastropietro, C., Moore, B., Mayer, L., Wadsley, J., & Stadel, J. 2005, MNRAS, 363, 509

Mathis, J. S., Rumpl, W., & Nordsieck, K. H. 1977, ApJ, 217, 425

Mebold, U., Cernicharo, J., Velden, L., et al. 1985, A&A, 151, 427

Meixner, M. & Tielens, A. G. G. M. 1993, ApJ, 405, 216

Melnick, G. J., Stauffer, J. R., Ashby, M. L. N., et al. 2000, ApJ, 539, L77

Meng, S. Y. & Kraus, J. D. 1970, AJ, 75, 535

Minamidani, T., Mizuno, N., Mizuno, Y., et al. 2007, ApJS submitted

Mizuno, N., Yamaguchi, R., Mizuno, A., et al. 2001, PASJ, 53, 971

Mochizuki, K., Nakagawa, T., Doi, Y., et al. 1994, ApJ, 430, L37

Motte, F. & André, P. 2001, in ASP Conf. Ser. 243: From Darkness to Light: Origin and Evolution of Young Stellar Clusters, ed. T. Montmerle & P. André, 301

Motte, F., Andre, P., & Neri, R. 1998, A&A, 336, 150

Myers, P. C. 1983, ApJ, 270, 105

Poglitsch, A., Krabbe, A., Madden, S. C., et al. 1995, ApJ, 454, 293

Press, W. H., Teukolsky, S. A., Vetterling, W. T., & Flannery, B. P. 1992, Numerical recipes in C. The art of scientific computing (Cambridge: University Press, |c1992, 2nd ed.)

Richter, P., Wakker, B. P., Savage, B. D., & Sembach, K. R. 2003, ApJ, 586, 230

Rohlfs, K. & Wilson, T. L. 2004, Tools of radio astronomy (Tools of radio astronomy, 4th rev. and enl. ed., by K. Rohlfs and T.L. Wilson. Berlin: Springer, 2004)

Röllig, M., Abel, N. P., Bell, T., et al. 2007, ArXiv Astrophysics e-prints

Röllig, M., Ossenkopf, V., Jeyakumar, S., Stutzki, J., & Sternberg, A. 2006, A&A, 451, 917

Rubio, M., Garay, G., Montani, J., & Thaddeus, P. 1991, ApJ, 368, 173

Rubio, M., Lequeux, J., & Boulanger, F. 1993, A&A, 271, 9

Sakamoto, S. 1996, ApJ, 462, 215

Salpeter, E. E. 1955, ApJ, 121, 161

Schlegel, D. J., Finkbeiner, D. P., & Davis, M. 1998, ApJ, 500, 525

Snell, R. L., Goldsmith, P. F., Erickson, N. R., Mundy, L. G., & Evans, II, N. J. 1984, ApJ, 276, 625

Solomon, P. M., Rivolo, A. R., Barrett, J., & Yahil, A. 1987, ApJ, 319, 730

Stacey, G. J., Jaffe, D. T., Geis, N., et al. 1993, ApJ, 404, 219

Stark, A. A., Bolatto, A. D., Chamberlin, R. A., et al. 1997, ApJ, 480, L59

Sternberg, A. & Dalgarno, A. 1989, ApJ, 338, 197

Sternberg, A. & Dalgarno, A. 1995, ApJS, 99, 565

Störzer, H., Stutzki, J., & Sternberg, A. 1996, A&A, 310, 592

Strong, A. W., Bloemen, J. B. G. M., Dame, T. M., et al. 1988, A&A, 207, 1

Stutzki, J. & Güsten, R. 1990, ApJ, 356, 513

Stutzki, J., Stacey, G. J., Genzel, R., et al. 1988, ApJ, 332, 379

Stutzki, J. & Winnewisser, G. 1985, A&A, 144, 13

Testi, L. & Sargent, A. I. 1998, ApJ, 508, L91

Tielens, A. G. G. M. & Hollenbach, D. 1985, ApJ, 291, 722

van der Werf, P. P., Stutzki, J., Sternberg, A., & Krabbe, A. 1996, A&A, 313, 633

van Dishoeck, E. F. & Black, J. H. 1988, ApJ, 334, 771

Verschuur, G. L. 1971, AJ, 76, 317

Verter, F. & Hodge, P. 1995, ApJ, 446, 616

Wakker, B. P. 2001, ApJS, 136, 463

Wakker, B. P. 2006, ApJS, 163, 282

Weiß, A., Heithausen, A., Herbstmeier, U., & Mebold, U. 1999, A&A, 344, 955

Werner, M. W., Becklin, E. E., Gatley, I., et al. 1978, MNRAS, 184, 365

Wesselius, P. R. & Fejes, I. 1973, A&A, 24, 15

Westerlund, B. E. 1997, The Magellanic Clouds (New York: Cambridge Univ. Press)

Williams, J. P., de Geus, E. J., & Blitz, L. 1994, ApJ, 428, 693

Wilson, C. D. 1995, ApJ, 448, L97+

Wolfire, M. G., Hollenbach, D., McKee, C. F., Tielens, A. G. G. M., & Bakes, E. L. O. 1995, ApJ, 443, 152

Wong, T., Whiteoak, J. B., Ott, J., Chin, Y.-n., & Cunningham, M. R. 2006, ApJ, 649, 224

Zinnecker, H. 1989, in Evolutionary Phenomena in Galaxies, ed. J. E. Beckman & B. E. J. Pagel, 113

List of Figures

List of Tables

Ich versichere, daß ich diese Arbeit selbständig verfaßt und keine anderen als die angegebenen Quellen und Hilfsmittel benutzt sowie Zitate kenntlich gemacht habe.